Taylor flow hydrodynamics in gas-liquid-solid micro reactors

PROEFSCHRIFT

ter verkrijging van de graad van doctor aan de Technische Universiteit Eindhoven, op gezag van de rector magnificus, prof.dr.ir. C.J. van Duijn, voor een commissie aangewezen door het College voor Promoties in het openbaar te verdedigen op donderdag 17 december 2009 om 16.00 uur

door

Maurice Jozef Fernande Warnier

geboren te Maastricht

Dit proefschrift is goedgekeurd door de promotor:

prof.dr.ir. J.C. Schouten

Copromotor:
dr. M.H.J.M. de Croon

A catalogue record is available from the Eindhoven University of Technology Library

ISBN: 978-90-386-2089-3

Taylor flow hydrodynamics in gas-liquid-solid micro reactors

Summary

Chemical reactions in which a gas phase component reacts with a liquid phase component at the surface of a solid catalyst are often encountered in chemical industry. The rate of such a gas-liquid-solid reaction is often limited by the mass transfer rate of the gas phase component, which depends on the hydrodynamics of the gas-liquid flow. The efficiency of a gas-liquid-solid reactor further depends on, amongst others, the pressure drop, which is also determined by the hydrodynamics.

Therefore, the trend in chemical industry towards more sustainable production methods has led to developments aimed at improving the performance of gas-liquid-solid reactors by tailoring the hydrodynamics. Two examples of these efforts are monolith reactors and microreactors, in which the gas and liquid are forced to flow through channels with diameters in the order of 10^{-4} to 10^{-3} m.

At these length scales, the hydrodynamics differ from those in conventional reactors and the Taylor flow regime is the main flow regime of interest. It consists of an alternating sequence of gas bubbles and liquid slugs. The length of the gas bubbles is larger than the channel diameter and a thin liquid film separates the gas bubbles from the channel walls, where the catalyst is located. The liquid at the interface of the gas bubble and this film is saturated with the gas component and, for a fast reaction, the concentration at the catalyst surface is very small. The large concentration gradient in the liquid film results in a high diffusion rate. Furthermore, due to the small dimensions of the channel, the specific interfacial surface area between the gas bubbles and the liquid film is large, which further increases gas component mass transfer rates compared to conventional reactors.

It is, therefore, important to understand the relation between gas-liquid Taylor flow hydrodynamics and gas component mass transfer. Additionally, it is required to understand

how the pressure drop depends on the various hydrodynamic parameters, since the pressure drop partly determines the efficiency of a reactor. Furthermore, to be able to fully optimize the reactor design, it has to be understood how to manipulate the Taylor flow hydrodynamics by varying parameters that can be controlled directly, *e.g.* the gas and liquid feed velocities, the geometry of the gas-liquid contactor and the geometry of the channel.

The thickness of the liquid film is a key parameter for gas component mass transfer in small channels, but it also determines the excess velocity of the gas bubbles with respect to the average velocity in the channel, which, in turn, determines the gas and liquid hold-up in the channel. The behaviour of the liquid film thickness is well understood for channels with a circular cross-sectional area and for negligible inertial and gravitational forces. In microreactors and monoliths, these conditions are not necessarily met and channels with a square or rectangular cross-sectional area are often used. Therefore, an experimental study was performed regarding the fraction of channel cross-sectional area occupied by the liquid film and the gas hold-up. Experiments were done for nitrogen-water Taylor flow in rectangular micro channels under conditions where inertial forces were significant. The results are presented in **chapter 2** and show that the gas hold-up as a function of the superficial gas and liquid velocities follows the well known Armand correlation, which states that the ratio of the gas hold-up and the volumetric fraction of gas in the feed flow is constant. A mass balance based Taylor flow model shows that the validity of the Armand correlation implies that the fraction of cross-sectional channel area occupied by the liquid film does not depend on the gas bubble velocity. From comparison of these results with literature data it was also shown that, when inertial effects are significant, the liquid film thickness is not only independent of the bubble velocity, but also occupies a fixed fraction of the channel cross-section independent of the channel diameter.

Pressure drop models for gas-liquid Taylor flow in capillaries are hardly available in literature, with the notable exception of one semi-empirical model for channels with a circular cross-section. In this work, a new pressure drop model was developed for gas-liquid Taylor flow with a non-negligible liquid film thickness in small channels (diameter typically < 1 mm) with a circular cross-section. The model takes two sources of pressure drop into account: (i) frictional pressure drop caused by laminar flow in the liquid slugs, and (ii) an additional pressure drop over a single gas bubble due to the gas bubble disturbing the otherwise parabolic velocity profile in the liquid slugs. The model includes the effects of the liquid slug length on the pressure drop, similar to the semi-empirical model available in literature.

Additionally, the model developed in this work includes the effect of the gas bubble velocity on the pressure drop over a single gas bubble. Data were obtained from experiments with nitrogen-water Taylor flow in a round glass channel with an inner diameter of 250 µm. The model described the experimental results with an accuracy of ± 4% of the measured values. This work is described in **chapter 3**.

Although the understanding of the pressure drop of gas-liquid Taylor flow in channels with a circular cross-sectional area is growing, no models are available for non-circular channels and detailed data sets are lacking. One complicating factor is that accurately measuring the pressure drop in microfluidic chips and in channels with a non-circular cross-sectional area is not straightforward. In **chapter 4**, a method is presented for estimating the pressure of a gas-liquid Taylor flow in a microchannel by combining results obtained from image analysis with a mass balance based Taylor flow model. The method was applied to nitrogen-water Taylor flow in channels with a square or rectangular cross-sectional area, as well as to nitrogen-isopropanol Taylor flow in a channel with a rectangular cross-sectional area. It was shown that the method developed in this chapter yields realistic values for the pressure drop of gas-liquid Taylor flow in microchannels with a non-circular cross-section. It, therefore, appears to be a viable method for determining the pressure drop of gas-liquid Taylor flow in microchannels. However, a more firm validation of the method by comparison with data obtained by another measurement technique still needs to be done.

For proper design of a gas-liquid-solid reactor in the Taylor flow regime, it is important to know for what combinations of gas and liquid velocities this regime occurs and how this range of combinations varies with various parameters. Flow maps were, therefore, determined while varying the liquid phase, the mixer design and the dimensions of the microfluidic channel. The mixer design was found to be of influence mainly on the regime transitions occurring at higher superficial velocities of one or both phases, where inertial effects are significant. On the other hand, varying the liquid phase between isopropanol and water affected all regime transitions, except those at high superficial gas and liquid velocities. When decreasing the dimensions of both the channel and the mixer, annular flow was no longer observed and Taylor flow could be obtained at higher gas velocities. This work is described in **chapter 5**

The mass transfer rate of the gas component depends on the lengths of the gas bubbles and liquid slugs. Furthermore, the liquid slug length partly determines the pressure

drop of gas-liquid Taylor flow. Therefore, the length of a gas bubble was studied as a function of the gas and liquid flow rates, the liquid phase, and the dimensions of the mixer. Experiments were performed for nitrogen-water and nitrogen-isopropanol Taylor in cross-mixers with either square or rectangular channels. This work is described in **chapter 5.** All the results could be described by a simple correlation, and they showed showed that, for a given mixer and channel, the gas bubble and liquid slug lengths can not be varied independently from each other. However, if the geometry of the mixer can be varied separately from the dimensions of the downstream channel, then the gas bubble length, liquid slug length and total flow rate, can each be controlled.

The rate of a gas-liquid-solid reaction per unit of reactor volume depends on the rate of external mass transfer, on the diffusion rate in the catalyst layer, and on the amount of catalyst per unit of reactor volume. The latter is determined by the ratio of the thickness of the catalyst layer and the channel diameter. The channel diameter also affects the external mass transfer rate, while the thickness of the catalyst layer determines, amongst others, the rate of diffusion in the catalyst layer. It is, therefore, important to choose the right combination of catalyst layer thickness and channel diameter in order to optimize the performance of the microreactor for a given gas-liquid-solid reaction. Other researchers recently developed a new method for applying a thin film of mesoporous titania to the wall of a capillary, and the film served as a catalyst support for Pd nanoparticles. This type of capillaries was further tested in this work, and the resulting data set was used as input for an optimization study of the channel diameter and the thickness of the catalyst layer. This work is described in **chapter 6**.

The hydrogenation of phenylacetylene in isopropanol was performed over Pd supported on mesoporous titania films with a thickness of $120 \cdot 10^{-9}$ m coated on the walls of a glass capillary with an inner diameter of 250 µm. Two such capillaries were used, containing, based on the weight of the coating, 1 wt% and 2 wt% Pd, respectively. The reaction was performed in the Taylor flow and Taylor-ring-annular regimes at temperatures varying from 313 to 343 K. The phenylacetylene conversions were smaller than 0.2 and styrene selectivities were higher than 0.92.

An optimization study based on these data showed that, for this catalyst:

- External mass transfer limitations can be avoided for channel diameters less than approximately 650 µm, regardless of the thickness of the catalyst layer.

- Internal mass transfer limitation can be avoided, if the thickness of the catalyst layer is less than 4 µm.

- Both internal and external mass transfer limitations are avoided, if the thickness of the catalyst layer is less than 4 µm and the channel diameter is smaller than $1.47 \cdot 10^{-3}$ m. At these limiting values the overall reaction rate coefficient per unit of capillary volume has a value of 0.10 s^{-1}. The amount of catalyst per unit of capillary volume is then 16.9 kg/m^3.

- For a fixed bubble velocity, fixed catalyst coating thickness and a relatively thin liquid film and catalyst coating, the ratio of the volumetric reaction rate coefficient of the catalyst and the volumetric mass transfer coefficient scales linearly with the channel diameter.

Furthermore, it was shown that, for channel diameters small enough to avoid external mass transfer limitations, further reducing the channel diameter at a constant catalyst layer thickness results in a nearly linear increase of the overall volumetric reaction rate, solely due to increasing the amount of catalyst per unit reactor volume. However, the pressure drop, and thus the frictional energy dissipation per unit of reactor volume, then increases quadratically. All other things being equal, the net result of decreasing the channel diameter, when external mass transfer limitations are no longer significant, is that the reactor efficiency decreases with decreasing channel diameter.

At the channel diameters currently used in monolith reactors, external mass transfer limitations in gas-liquid-solid reactions can already be overcome. While microreactor technology enables the use of channels with a diameter an order of magnitude smaller than currently used in monolith reactors, such a further reduction of channel diameter, solely motivated by increasing the amount of catalyst per unit of reactor volume, is not efficient. However, if heat transfer is limiting or if the intrinsic rates of these types of reactions can be increased, *e.g.* through catalyst development or by using microchannels to open new process windows, then a reduction of the channel diameter beyond those used in monolith reactors can be beneficial.

Table of contents

Chapter 1

Introduction

1.1 Gas-liquid-solid reactions in small channels

Chemical reactions between gas and liquid phase components catalyzed by a solid are often encountered in chemical industry. These gas-liquid-solid reactions are typically performed in stirred slurry reactors, slurry bubble columns or packed bed reactors [1]. In the first two types, the catalyst particles are suspended in the liquid phase while the gas is allowed to bubble through the suspension. For the latter type, the catalyst is fixed in the reactor and can either be dumped randomly in the reactor volume or be fixed as structured elements.

In a reactor, the overall rate of such a gas-liquid-solid reaction depends on many parameters, *e.g.* mass transfer rates by diffusion and convection, and the intrinsic reaction rate at the catalyst surface. The overall performance of the reactor, in terms of energy efficiency and production per unit volume of reactor, also depends on the pressure drop or the power input of the stirrer, if any, and the heat transfer rates that can be achieved. In turn, the mass and heat transfer rates as well as the pressure drop depend on the hydrodynamics of the gas and liquid flows.

The trend in chemical industry towards more sustainable production methods has led to a number of developments aimed at improving the performance of gas-liquid-solid reactors by tailoring the hydrodynamics [2,3]. One such development is the application of monolith reactors for this type of reactions [4,5]. The monolith reactor is a structured reactor consisting of a large number of identical and straight channels through which the gas and liquid are allowed to flow and the catalyst is located on the channel walls in the form of a washcoat. The channel diameters are typically in the order of a few hundred micrometers to

a millimeter and, at this length scale, the hydrodynamics of the laminar gas-liquid flows differ from those in more traditional types of reactors. The reduced characteristic length scale results in higher interfacial areas and larger concentration gradients, leading to higher volumetric mass transfer rates, which often limit the reaction rate in packed beds, slurry bubble columns and stirred tank reactors. Furthermore, monolith reactors generally have a lower pressure drop compared to packed bed reactors.

The relatively small characteristic channel dimensions in monolith reactors are, arguably, the result of evolution of classical reactor engineering. On the other hand, developments in the relatively new fields of micro-electro-mechanical systems (MEMS) and micro total analysis systems (μTAS) have led to the application of these systems for performing a plethora of chemical reactions [6]. The heart of these systems are chips containing microfluidic structures of which the characteristic length scale is in the order of 10^{-5} to 10^{-4} m. Compared to conventional reactors, the reduced characteristic length scales in these systems can have various advantages: faster mixing times, better mass transfer, better heat transfer due to the larger surface to volume ratio, and better inherent safety due to the small volumes per chip [7]. These properties can allow for combinations of reaction conditions outside the reach of more conventional reactors, which opens novel process windows [8,9,10]. Despite their use in many applications, chip based microreactors and microstructured reactors have, so far, been applied to only a limited amount of gas-liquid-solid reactions, while the possible gains in mass transfer rates are clear [11,12,13]. The reason may be that a porous catalyst layer is required in order to obtain enough surface area to obtain reaction rates large enough for practical purposes. Applying such a layer in microfluidic channels in a chip is far more difficult [7] than applying it to, for instance, a monolith or capillary where washcoating can be used.

1.2 Gas-liquid Taylor flow and gas-liquid-solid reactions

Monoliths and microreactors for gas-liquid and gas-liquid-solid reactions are generally operated in the gas-liquid Taylor flow regime [14,15,16], which is also commonly used in various other gas-liquid microfluidic applications. A typical image of gas-liquid Taylor flow is given in Figure 1.1. It consists of sequences of a gas bubble and a liquid slug. The length of the gas bubbles is larger than the channel diameter and a thin liquid film separates the gas

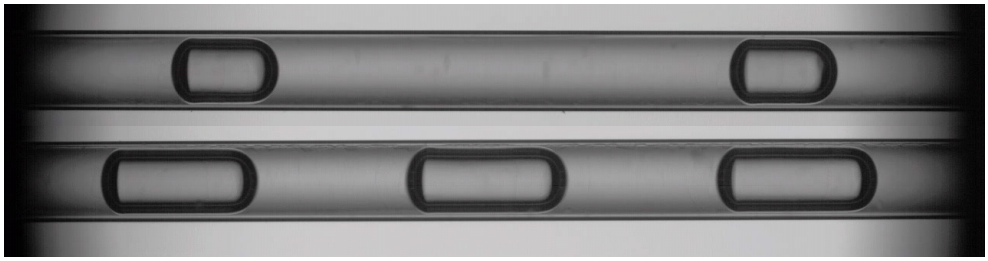

Figure 1.1: Typical images of two different nitrogen-water Taylor flow recorded in a glass capillary with an internal diameter of 250 µm.

bubbles from the channel walls. For horizontal and vertical channels, in which gravitational forces are negligible, the liquid film is stagnant. Furthermore, for liquids and bubble velocities typically applied in gas-liquid-solid reactions, most of the liquid in the slugs forms recirculation cells. The recirculation cells move at the same velocity as the gas bubbles and there is no convective flow in or out of them. Thus, there is hardly any interaction between two liquid slugs. This feature is commonly used in *µ*TAS systems, where Taylor gas bubbles are used for keeping various liquid samples separated from each other while moving through a microfluidic system.

The key hydrodynamic parameters in gas-liquid Taylor flow are: the gas bubble length, the liquid slug length, the gas bubble velocity and the liquid film thickness. For proper design of reactors and microfluidic devices operating under Taylor flow conditions, it is required to understand how these parameters influence mass transfer rates, heat transfer rates and pressure drop. Furthermore, it is also required to understand how to manipulate the Taylor flow hydrodynamics by parameters that can be controlled directly, *e.g.* the gas and liquid feed velocities, the geometry of the gas-liquid contactor and the geometry of the channel.

1.2.1 Thickness of the liquid film

The thickness of the liquid film is a key parameter in the operation of gas-liquid-solid reactions under Taylor flow conditions. Firstly, the thin liquid film surrounding the gas bubble ensures a short diffusion path length for the gas phase component diffusing from the gas-liquid interface through the film to the channel wall, where the catalyst is located. Thus, it determines the maximum mass transfer coefficient that can be achieved for a given gas-liquid system. Secondly, the thickness of the liquid film also determines the excess velocity

of the gas bubbles with respect to the average velocity in the channel, which determines the gas and liquid hold-up in the channel.

The behaviour of the liquid film as function of the gas bubble velocity and the properties of the liquid phase are well understood for channels with a circular cross-sectional area and negligible inertial forces compared to surface tension and viscous forces [17,18]. However, in practice, inertial forces can not always be neglected and the channels in monoliths and chip based microfluidic devices generally have square or rectangular cross-sectional areas. The effects of these parameters on the thickness of the liquid film have been studied in several computational studies [19,20,21,22,23], but experimental data are limited [24,25] and analytical equations or correlations are lacking.

1.2.2 Gas-liquid-solid mass transfer

Since gas to liquid mass transfer is usually the rate determining step in gas-liquid-solid reactions, its relation to Taylor flow hydrodynamics has been the subject of study for many years. Assuming gas side mass transfer resistances are negligible, three steps for gas component mass transfer are identified [26,27,28] for a gas-liquid-solid reaction occurring at the channel wall under Taylor flow conditions, as illustrated in Figure 1.2. These steps are:

1) mass transfer from the gas bubbles to the liquid slug,

2) mass transfer from the liquid slug to the catalyst and,

3) mass transfer from the gas bubble through the liquid film to the catalyst,

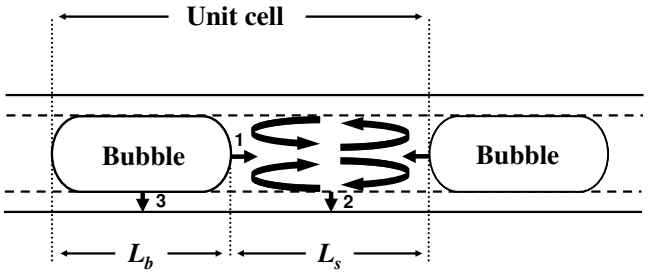

Figure 1.2: Three mass transfer steps for gas component mass transfer to the catalyst at the channel wall: 1) from the bubble caps to the liquid slug, 2) from the liquid slug through the liquid film to the catalyst, and 3) from the gas bubble through the liquid film to the catalyst. The definitions of a unit cell, the bubble length L_b and the liquid slug length L_s are also indicated.

where steps 1 and 2 occur in series, parallel to step 3.

Mass transfer through the liquid film occurs by diffusion only, and thus the liquid film thickness is a crucial parameter. Mass transfer from the gas bubble caps to the liquid slug is a combination of diffusion and convection due to the recirculation cells.

The volumetric mass transfer coefficient for the gas bubble cap to the liquid slug is smaller than for the liquid slug to the channel wall. Furthermore, mass transfer from the gas bubble directly through the liquid film, step 3, provides the shortest possible diffusion path for the gas component. This step, combined with the large interfacial area due to the small channel size, is where the gain in the volumetric mass transfer coefficient is made compared to conventional reactors, and is hence the subject of interest.

The overall volumetric mass transfer coefficient depends on the liquid film thickness, the gas bubble velocity and the lengths of the liquid slugs and gas bubbles. While gas-liquid-solid mass transfer in channels with a circular cross-sectional area is reasonably well understood, a complicating factor occurs when considering channels with a non-circular cross-sectional area. The liquid film thickness is not uniform and is thicker in the corners of a square or rectangular channel. Knowledge of the shape of the liquid film is then required in order to be able to calculate mass transfer coefficients, and, as mentioned previously, this understanding is not yet complete.

1.2.3 Pressure drop

It is well documented in literature that conventional two-phase pressure drop correlations fail to consistently describe the pressure drop of gas-liquid Taylor flow in small channels. The reason is that these correlations were obtained for channels with larger diameters, where surface tension forces are less dominant compared to gas-liquid flows in smaller channels. Furthermore, these models do not take the hydrodynamic details, such as the gas bubble and liquid slug lengths, into account.

Recently, a semi-empirical model was developed that describes the pressure drop of gas-liquid Taylor flows as the sum of the frictional pressure drop caused by laminar flow in the liquid slugs and an additional term accounting for the effect of the gas bubbles disturbing the otherwise parabolic velocity profile in the liquid slugs [23]. The correlation captures the

effect of the liquid slug length on the pressure drop: the relative contribution of the additional pressure drop caused by the gas bubbles decreases with increasing liquid slug length.

However, an understanding of the nature of the fitted parameters is still lacking and the correlation has not yet been extensively tested for various channel geometries, ranges of channel diameters, and low gas bubble velocities.

1.2.4 Heat transfer

Heat transfer in single phase flows in small channels has been studied by various authors, but little research has been performed on heat transfer in gas-liquid flows in small channels [29]. A better understanding of heat transfer in multiphase flows in small channels is required, both for modeling purposes and for comparison of various reactor designs [2].

1.2.5 Creating Taylor flow

As the understanding of pressure drop and gas-liquid-solid mass transfer as a function of the various hydrodynamic properties of gas-liquid Taylor flow is growing [14,15], it is also important to be able to control those hydrodynamics.

Many flow maps have been published for a variety of channel geometries and hydraulic channel diameters ranging from 10^{-5} to 10^{-3} m. Most of the data gave been obtained for nitrogen-water, or for air-water systems. Although the details of the flow maps vary, all maps show that Taylor flow in channels with a diameter typically in the order of 10^{-3} m or less occurs for superficial gas and liquid velocities in the order of 1 m/s or less [30].

In microfluidic applications, gas-liquid Taylor flow is generally created by either introducing the gas into the liquid flow at an angle of 90^0 with respect to the direction of the liquid flow, the so-called “T-mixer”, or by introducing two liquid streams into the gas stream at an angle of 90^0 with respect to the direction of the gas flow, the “cross-mixer”. The gas bubble length is found to depend on the ratio of the superficial gas and liquid velocities and the dimensions of the mixer, regardless of whether a T- or cross-mixer is used [31,32,33]. Once the gas bubble length is known, the number of gas bubbles formed per unit time and the liquid slug length can easily be calculated from the known superficial gas and liquid velocities.

For monolith reactors, nozzle or shower head distributors are used instead of these type of T- and cross-mixers [34]. For these systems, experimental work is available in which the liquid slug length was measured as a function of the ratio of the superficial liquid velocity and the sum of the superficial gas and liquid velocities for various distributors. The results showed that, for a given combination of superficial gas and liquid velocities, the liquid slug length is a function of the type of distributor.

The results for both the monolith reactors and microfluidic devices show that, for a given combination of gas and liquid velocities, the number of gas bubbles, and thus the gas bubble and liquid slug lengths, can be chosen by selecting the right distributor or mixer. This decoupling of hydrodynamics and flow rates is another advantage of gas-liquid Taylor flow in small channels compared to conventional reactors.

1.3 Scope and outline of this thesis

The research described in this thesis was carried out within the “Microstructured Reaction Architectures for Advanced Chemicals Synthesis” project, or in short, the “MiRAACS” project. The project was funded by the Dutch Technology Foundation (STW, project no. EPC.6359), Schering-Plough, DSM Pharmaceutical Products, Shell Global Solutions, Akzo Nobel Chemicals B.V., Bronkhorst High-Tech B.V. and TNO.

The goal of the project was to develop a microreactor system, based on the lab-on-a-chip approach, for the selective hydrogenation of α,β-unsaturated aldehydes to their corresponding alcohols. The research was divided into two sub-projects. One sub-project focussed on the development of bi-metallic catalysts and kinetics of these hydrogenation reactions and the research was carried out by Oki Muraza. The goal of the second sub-project was to gain more insight in the hydrodynamics of gas-liquid flows in small channels and their relation to pressure drop and mass transfer and the results are presented in this thesis.

In chapter 2, the results of an experimental study regarding the liquid film thickness and gas hold-up in nitrogen-water Taylor flow in rectangular micro channels are presented. These two parameters are obtained from combining results from image analysis with a mass balance based model.

In chapter 3, a model is presented for the pressure drop of gas-liquid Taylor flow in channels with a circular cross-sectional area. The model is compared to experimental results obtained for nitrogen-water Taylor flow in a capillary with a diameter of 250 μm. The performance of the model is compared to that of a semi-empirical model developed for Taylor flow, and a well-known model developed for larger channels, which is commonly applied to microchannels.

In chapter 4, a method is presented to estimate the pressure of a gas-liquid Taylor flow in a microchannel by combining results obtained from image analysis with a mass balance based Taylor flow model. The method was applied to nitrogen-water Taylor flow in channels with a square and rectangular cross-sectional area, as well as to nitrogen-isopropanol Taylor flow in a channel with a rectangular cross-sectional area. The results obtained in this manner, where then compared to existing pressure drop models, including the model developed in chapter 3.

In chapter 5, results obtained with respect to creating Taylor flow in microchannels are presented. The data were obtained with the same gas-liquid systems and microfluidic chips used in chapters 2 and 4. Flow maps were made for all of these systems. Furthermore, the gas bubble length as a function of the superficial gas and liquid velocities and mixer design was studied. The results are compared to models available in literature.

In chapter 6, an optimization study of the catalyst layer thickness and the channel diameter is discussed, based on experimental data. The hydrogenation of phenylacetylene in isopropanol was performed in round microcapillaries with a diameter of 250 μm, in which a Pd/TiO_2 mesoporous catalyst was deposited. The reaction was carried out in both Taylor flow conditions and at higher superficial gas velocities. These data were then used in order to determine which values of the volumetric reaction rate coefficient can be obtained by varying the thickness of the catalyst layer and the channel diameter. The following cases are considered:

- not allowing internal or external mass transfer limitations,
- allowing only internal mass transfer limitations,
- allowing both internal and external mass transfer limitations.

In chapter 7, the main conclusions of this thesis are summarized and suggestions for further research are given. Furthermore, some comments are made regarding gas-liquid-solid reactions in small channels.

References

[1] Dudoković, M. P., Larachi, F., Mills, P. L., Multiphase catalytic reactors: a perspective on current knowledge and future trends. *Catalysis reviews*, 44(1), 123-246, 2002

[2] Pangarkar, K., Schildhauer, T. J., Van Ommen, J. R., Nijenhuis, J., Kapteijn, F., Moulijn, J. A., Structured packings for multiphase catalytic reactors. *Ind. Eng. Chem. Res.*, 47(10), 3720-3751, 2008

[3] Stitt, E. H., Alternative multiphase reactors for fine chemicals: A world beyond stirred tanks? *Chem. Eng. J.*, 90(1-2), 47-60, 2002

[4] Kapteijn, F., Nijhuis, T. A., Heiszwolf, J. J., Moulijn, J. A., New non-traditional multiphase catalytic reactors based on monolithic structures. *Catal Today*, 66(2-4), 133-144, 2001

[5] Nijhuis, T. A., Kreutzer, M. T., Romijn, A. C. J., Kapteijn, F., Moulijn, J. A., Monolithic catalysts as efficient three-phase reactors. *Chem. Eng. Sci.*, 56(3), 823-829, 2001

[6] Günther, A., Jensen, K. F., Multiphase microfluidics: From flow characteristics to chemical and materials synthesis. *Lab Chip Miniaturisation Chem. Biol.*, 6(12), 1487-1503, 2006

[7] Gavriilidis, A., Angeli, P., Cao, E., Yeong, K. K., Wan, Y. S. S., Technology and applications of microengineered reactors. *Chem. Eng. Res. Des.*, 80(1), 3-30, 2002

[8] Hessel, V., Löwe, H., Organic synthesis with microstructured reactors. *Chem. Eng. Technol.*, 28(3), 267-284, 2005

[9] Jensen, K. F., Microreaction engineering-is small better? *Chem. Eng. Sci.*, 56(2), 293-303, 2001

[10] Hessel, V., Novel Process Windows - Gate to Maximizing Process Intensification via Flow Chemistry. *Chem. Eng. Technol.*, 32(11), in press, 2009

[11] Besser, R. S., Ouyang, X., Surangalikar, H., Hydrocarbon hydrogenation and dehydrogenation reactions in microfabricated catalytic reactors. *Chem. Eng. Sci.*, 58(1), 19-26, 2003

[12] Losey, M. W., Schmidt, M. A., Jensen, K. F., Microfabricated multiphase packed-bed reactors: Characterization of mass transfer and reactions. *Ind. Eng. Chem. Res.*, 40(12), 2555-2562, 2001

[13] Kobayashi, J., Mori, Y., Okamoto, K., Akiyama, R., Ueno, M., Kitamori, T., Kobayashi, S., A microfluidic device for conducting gas-liquid-solid hydrogenation reactions. *Science*, 304(5675), 1305-1308, 2004

[14] Angeli, P., Gavriilidis, A., Hydrodynamics of Taylor flow in small channels: A review. *Proc. Inst. Mech. Eng. Part C J. Mech. Eng. Sci.*, 222(5), 737-751, 2008

[15] Kreutzer, M. T., Kapteijn, F., Moulijn, J. A., Heiszwolf, J. J., Multiphase monolith reactors: Chemical reaction engineering of segmented flow in microchannels. *Chem. Eng. Sci.*, 60(22), 5895-5916, 2005

[16] Günther, A., Khan, S. A., Thalmann, M., Trachsel, F., Jensen, K. F., Transport and reaction in microscale segmented gas-liquid flow. *Lab Chip Miniaturisation Chem. Biol.*, 4(4), 278-286, 2004

[17] Bretherton, F. P., The motion of long bubbles in tubes. *J. Fluid. Mech.*, 10, 166-188, 1961

[18] Aussillous, P., Quéré, D., Quick deposition of a fluid on the wall of a tube. *Phys. Fluids*, 12(10), 2367-2371, 2000

[19] Hazel, A. L., Heil, M., The steady propagation of a semi-infinite bubble into a tube of elliptical or rectangular cross-section. *J. Fluid. Mech.*, 470, 91-114, 2002

[20] Giavedoni, M. D., Saita, F. A., The axisymmetric and plane cases of a gas phase steadily displacing a Newtonian liquid - A simultaneous solution of the governing equations. *Phys. Fluids*, 9(8), 2420-2428, 1997

[21] Westborg, H., Hassager, O., Creeping motion of long bubbles and drops in capillary tubes. *J. Colloid Interface Sci.*, 133(1), 135-147, 1989

[22] Fujioka, H., Grotberg, J. B., The steady propagation of a surfactant-laden liquid plug in a two-dimensional channel. *Phys. Fluids*, 17(8), 1-17, 2005

[23] Kreutzer, M. T., Kapteijn, F., Moulijn, J. A., Kleijn, C. R., Heiszwolf, J. J., Inertial and interfacial effects on pressure drop of Taylor flow in capillaries. *AIChE Journal*, 51(9), 2428-2440, 2005

[24] Thulasidas, T. C., Abraham, M. A., Cerro, R. L., Bubble-train flow in capillaries of circular and square cross section. *Chem. Eng. Sci.*, 50(2), 183-199, 1995

[25] Kolb, W. B., Cerro, R. L., The motion of long bubbles in tubes of square cross section. *Phys. Fluids*, 5(7), 1549-1557, 1993

[26] Kreutzer, M. T., Du, P., Heiszwolf, J. J., Kapteijn, F., Moulijn, J. A., Mass transfer characteristics of three-phase monolith reactors. *Chem. Eng. Sci.*, 56(21-22), 6015-6023, 2001

[27] Van Baten, J. M., Krishna, R., CFD simulations of mass transfer from Taylor bubbles rising in circular capillaries. *Chem. Eng. Sci.*, 59(12), 2535-2545, 2004

[28] Van Baten, J. M., Krishna, R., CFD simulations of wall mass transfer for Taylor flow in circular capillaries. *Chem. Eng. Sci.*, 60(4), 1117-1126, 2005

[29] Hetsroni, G., Mosyak, A., Pogrebnyak, E., Segal, Z., Heat transfer of gas-liquid mixture in micro-channel heat sink. *Int. J. Heat Mass Transf.*, 52(17-18), 3963-3971, 2009

[30] Shao, N., Gavriilidis, A., Angeli, P., Flow regimes for adiabatic gas-liquid flow in microchannels. *Chem. Eng. Sci.*, 64(11), 2749-2761, 2009

[31] Van Steijn, V., Kreutzer, M. T., Kleijn, C. R., μ-PIV study of the formation of segmented flow in microfluidic T-junctions. *Chem. Eng. Sci.*, 62(24), 7505-7514, 2007

[32] Cubaud, T., Tatineni, M., Zhong, X., Ho, C. M., Bubble dispenser in microfluidic devices. *Physical Review E - Statistical, Nonlinear, and Soft Matter Physics*, 72(3), 1-4, 2005

[33] Garstecki, P., Fuerstman, M. J., Whitesides, G. M., Stone, H. A., Formation of droplets and bubbles in a microfluidic T-junction - Scaling and mechanism of break-up. *Lab Chip Miniaturisation Chem. Biol.*, 6(3), 437-446, 2006

[34] Kreutzer, M. T., Eijnden, M. G. V. D., Kapteijn, F., Moulijn, J. A., Heiszwolf, J. J., The pressure drop experiment to determine slug lengths in multiphase monoliths. *Catal Today*, 105(3-4), 667-672, 2005

Chapter 2

Gas hold-up and liquid film thickness in Taylor flow in rectangular micro channels

This chapter has been adapted from:

Warnier, M.J.F., Rebrov, E.V., De Croon, M.H.J.M., Hessel, V., Schouten, J.C., Gas hold-up and liquid film thickness in Taylor flow in rectangular microchannels. *Chem. Eng. J.*, 135S, S153-S158, 2007

Abstract

The gas hold-up in nitrogen-water Taylor flows in a glass micro channel of rectangular cross-section (100x50 μm^2) was shown to follow the Armand correlation when inertial effects are significant. The validity of the Armand correlation implies that the fraction of cross-sectional channel area occupied by the liquid film is not a function of the bubble velocity, which was varied between 0.24 and 7.12 m/s. This behaviour differs from the results reported for viscous fluids, where inertial effects were not significant, and the fraction of cross-sectional channel area occupied by the liquid film increases with increasing bubble velocity.

Images of the Taylor flow were captured at a rate of 10,000 frames per second and were used to obtain the bubble and liquid slug lengths, the bubble velocity, and the number of bubbles formed per unit of time. A mass balance based Taylor flow model was used to calculate the superficial gas velocity and gas hold-up at the imaging location from the data obtained from imaging.

2.1 Introduction

Taylor flow is the main flow regime of interest for performing gas/liquid/solid reactions in small channels (diameter < 1 mm). It consists of sequences of a gas bubble and a liquid slug. The length of the gas bubbles is larger than the channel diameter and a thin liquid film separates the gas bubbles from the channel walls. The liquid film ensures a short diffusion path length for the gas phase diffusing through the film to the channel wall, where the catalyst is often located. The liquid in the slugs forms circulation cells when the capillary number ($Ca=\mu_l u_b/\sigma$) is smaller than 0.5 [1,2]. The circulation patterns cause radial mass transfer by convection, where it is otherwise determined solely by diffusion [3]. The thin liquid film and the liquid circulation cells make Taylor flow a suitable flow regime for three-phase reactions where mass transfer to the wall is of influence on the reaction rate.

The thickness of the liquid film and the liquid velocity therein are key parameters, not only for mass transfer, but also for describing the hydrodynamics of Taylor flow. The gas hold-up is an important parameter in reactor design since it determines the mean residence times of the phases in the reactor and is related to the thickness of the liquid film. Due to the presence of the liquid film, the gas bubbles move through a smaller cross-sectional area than the combined gas and liquid flows. Continuity then requires that the velocity of the gas bubbles is larger than the total superficial velocity in the channel. Because of this, the gas hold-up differs from the flow quality, which is defined as the volumetric fraction of gas in the feed stream. The relation between liquid film thickness and gas hold-up also depends on the flow rate of the liquid in the film.

Bretherton [4] showed that the liquid film thickness is a function of the capillary number for capillaries with a circular cross-section. His model is valid for vanishing liquid film thickness and for negligible inertial and gravitational forces, i.e. $Ca_b < 0.05$, $We_b=\rho_l u_b^2 D_h/\sigma << 1$ and $Bo=(\rho_l-\rho_g)gD_h^2/\sigma << 3$. Aussillous and Quéré [5] expanded Bretherton's theory by taking a non negligible liquid film thickness into account and fitting their equation to the data of Taylor [6]. The conditions in small reactor channels operated in Taylor flow conditions are often such that inertia has to be accounted for when estimating the liquid film thickness. When taking inertia into account, the liquid film thickness is also a function of the Reynolds number ($Re_b=\rho_l u_b D_h/\mu_l$), as shown by a number of numerical studies [5,7,8,9,10]. Aussillous and Quéré found, from their experimental data, that inertial effects give rise to a thicker liquid film than predicted by Bretheron's theory and provide a qualitative explanation for this

effect. They also stated that the thickening effect is superimposed by a geometric effect which makes the liquid film thickness converge to a finite fraction of the tube radius. However, they provide no quantitative analysis for predicting this limit in the liquid film thickness.

For channels with a square or rectangular cross-section, as often encountered in monolithic reactors and microfluidic devices, the liquid film thickness is not uniform along the channel perimeter [2,11,12,13,14]. Kreutzer *et al.* [15] correlated the bubble diameter to the capillary number based on the experimental data of Kolb *et al.* and Thulasidas *et al.* [2,13] and the numerical data set of Hazel and Heil [12]. The calculations of Hazel and Heil were done in absence of inertial effects. The experiments of Kolb *et al.* were done with viscous fluids in a 2x2 mm^2 square channel at low gas bubble velocities, where inertial effects can also be neglected. The work of Thulasidas *et al.* was performed in the same channels at lower liquid viscosities for up-flow, down-flow and horizontal flow. However, no data sets are available for low viscous fluids in square or rectangular channels with diagonal channel diameters in the order of 10^{-4} m, as used in this work and often encountered in microfluidic and monolithic reactors.

Experimentally determining the liquid film thickness or gas hold-up from images of the flows is difficult, especially for channels with a rectangular cross-section and the relatively large bubble velocities used in this work. The shapes of the cross-sectional area and of the nose and tail sections of a gas bubble are not axisymmetrical and can not be obtained directly from images of the flow. Therefore, in this work, a mass balance based model for Taylor flow is used to obtain the cross-sectional bubble area of a gas bubble from experimental data acquired by imaging techniques. This method is also used to determine the amount of liquid having a non-zero velocity surrounding the nose and tail sections. This allows for calculation of the gas hold-up, which can then be compared to several data sets from literature. These contain the gas hold-up of gas-liquid Taylor flow for various conditions, but do not include data concerning the liquid film thickness. The mass balance model used in this work is similar to that of Thulasidas *et al.* [13], although its derivation is different.

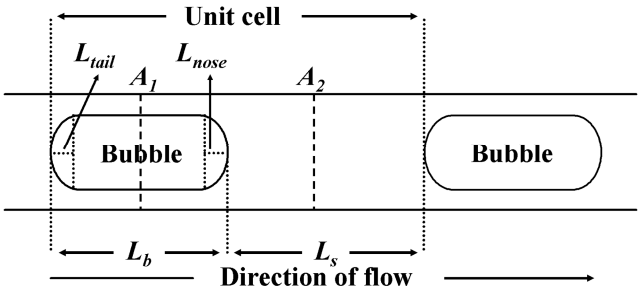

Figure 2.1: Schematic of Taylor flow showing the definitions of the unit cell, gas bubble length L_b and the liquid slug length L_s. The lengths of the nose L_{nose} and tail L_{tail} sections of the gas bubble are also indicated.

2.2 Taylor flow model

Consider a gas-liquid Taylor flow moving through a channel with a cross-sectional area A. The gas bubbles have a velocity u_b, a length L_b and occupy a fraction of the cross-sectional area of the channel A_b/A. The liquid slugs have a length L_s. The flow is divided into unit cells consisting of one gas bubble, its surrounding liquid film, and one liquid slug and the unit cell length is L_b+L_s. These definitions are illustrated in Figure 2.1.

Continuity requires that the overall average velocity through any cross-section of the channel perpendicular to the direction of flow is equal to the sum of the superficial gas U_g and liquid U_l velocities, which are based on the channel cross-section A. The flow through plane A_1 consists of the gas bubble moving with velocity u_b through a cross-section A_b, and the liquid film moving at an average velocity u_f through a cross-section A-A_b, giving:

$$\frac{A_b}{A}u_b + \left(1 - \frac{A_b}{A}\right)u_f = U_g + U_l \tag{2.1}$$

The flow through plane A_2 consists solely of liquid which occupies the whole cross-section of the channel A and the average velocity of the liquid in the slug is therefore equal to U_g+U_l.

The superficial gas velocity U_g is equal to the bubble volume times the bubble formation frequency F_b, divided by the channel cross-sectional area A. If the bubble volume is taken to be the bubble length L_b times its cross-sectional area A_b, then it is overestimated

because part of the volume $A_b(L_{nose}+L_{tail})$ consists of liquid. This liquid volume depends on the bubble geometry, but can arbitrarily be written as the bubble cross-sectional area A_b times a length δ. This length δ is then a correction on the bubble length to account for the overestimation of the gas bubble volume if it were taken to be equal to A_bL_b. Note that, in case of a bubble with a circular cross-section and hemispherical bubble caps, it can be shown that δ is 1/3 of the bubble diameter D_b. The superficial gas velocity U_g is then given by:

$$U_g = \frac{A_b}{A} F_b \left(L_b - \delta \right) \tag{2.2}$$

The bubble formation frequency F_b is equal to the number of unit cells passing a certain location in the channel per unit of time, which is the reciprocal of the time it takes for a unit cell to travel a distance equal to its own length: $(L_b+L_s)/u_b$. The bubble formation frequency is therefore given by:

$$F_b = \frac{u_b}{L_b + L_s} \tag{2.3}$$

If equations (2.2) and (2.3) are substituted into equation (2.1), the following expression is obtained for the superficial liquid velocity U_l:

$$U_l = \frac{A_b}{A} F_b \left(L_s + \delta \right) - \left(1 - \frac{A_b}{A} \right) u_f \tag{2.4}$$

The gas hold-up ε_g is defined as the fraction of channel volume occupied by the gas and is equal to U_g/u_b, which can be rewritten with the previous equations as shown in equation (2.5).

$$\varepsilon_g = \frac{U_g}{u_b} = \frac{A_b}{A} \left(\frac{L_b - \delta}{L_b + L_s} \right) = \frac{A_b}{A} \frac{U_g}{U_g + U_l - \left(1 - \frac{A_b}{A} \right) u_f} \tag{2.5}$$

Equations (2.1) to (2.5) are valid regardless of the channel geometry, whether or not liquid recirculation cells are present, or whether or not the liquid film surrounding the gas bubbles is stagnant. For vertically oriented systems with respect to the gravity vector, gravity can cause flow in the film region, especially for channels with a rectangular cross-section. However, in this work horizontally oriented channels are used and the Bond number is in the order of 10^{-3}. Gravity is therefore not a source for flow in the liquid film. Furthermore, in absence of impurities, it is reported that there is no pressure gradient in the liquid film in the uniform bubble region, eliminating another potential source for liquid flow in the film [7,11]. Thus, the liquid film surrounding the gas bubbles is stagnant and u_f is equal to 0 in equations (2.1), (2.4) and (2.5).

2.3 Experimental

The micro fluidic chips used in this work were designed for investigating the influence of mixer design on the gas/liquid hydrodynamics in the subsequent channel as described in [16]. The chips consist of two anodically bonded Pyrex glass wafers. The micro fluidic structures were etched by Deep Reactive Ion Etching and the in- and outlet holes were made by powder blasting. The chips were constructed by LioniX BV. Figure 2.2 shows the designs of the mixers. For both designs, the gas inlet is encompassed by two liquid inlets. The two mixers differ in angle at which the gas and liquid streams are contacted. For the cross mixer, the angle between the gas and liquid inlets is 90^0. In the smooth mixer the inlets are nearly parallel to each other. Both mixers then focus the flow into a 2 cm long channel with a 50 x 100 μm^2 rectangular cross-section.

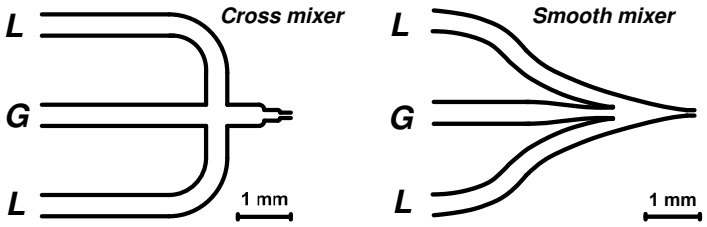

Figure 2.2: Geometries of the two mixers used for realizing two-phase flow in a downstream channel with a rectangular cross-section of 100 x 50 μm^2 and a length of 2 cm. The depth of these structures is 50 μm. The bar represents 1 mm.

Table 2.1: Superficial liquid U_l and gas velocities U_g^0 for which a stable, regular Taylor flow was observed with bubble and slugs lengths suitable for image analysis. The superficial gas velocity is given at a temperature of 20 ^{0}C and a pressure of 1 bar. The range of flow qualities used in the experiments is also given.

	U_l [m/s]	U_g^0 [m/s]	$U_g^0/(U_g^0+U_l)$ [-]
Cross mixer	0.07-1.90	0.50-10	0.43-0.91
Smooth mixer	0.07-0.47	0.50-50	0.45-0.91

All experiments were carried out with nitrogen gas and demineralised water at a temperature of 20 ^{0}C. The gas flow was regulated by a set of mass flow controllers (Bronkhorst F-200C and Bronkhorst F-201C). An LKB 2150 high-performance liquid chromatography pump was used to create the liquid flow. The range of superficial velocities used in the experiments, is given in Table 2.1.

Images of the flows were recorded by a Redlake MotionPro CCD camera connected to a Zeiss Axiovert 200 MAT inverted microscope. The images were recorded at a resolution of 1280 x 48 pixels at a rate of 10,000 frames per second. An exposure time of 12 μs was sufficient to eliminate significant motion blur. The width of one pixel represented 3.6 μm of channel length. All images captured 2.86 mm of channel length and their centerpoint was located 17.8 mm from the channel entrance. For every combination of gas and liquid velocities, three movies of 5000 frames each were recorded (0.5 s measurement time per movie).

For each movie, every individual bubble was tracked and its length was averaged over all frames it occurred in. These values were then averaged to obtain the average bubble length L_b for that movie. The same was done for the liquid slugs, giving the average slug length L_s. The bubble frequency F_b is the number of tracked bubbles divided by the measurement time. The average velocity of a single bubble was obtained by dividing the distance travelled by its centre of mass in the movie by the time that the bubble was present in that movie. Like the average bubble and slug lengths, the velocity was first determined for every single bubble and then averaged over all bubbles to give the average bubble velocity u_b.

2.4 Results and discussion

The results from image analysis are given in Table 2.2. The capillary, Reynolds and Weber *($We_b=\rho D_h u_b^2/\sigma$)* numbers based on the liquid properties and the gas bubble velocities observed in the experiments are given in Table 2.3.

$$L_s = \frac{U_l A}{F_b A_b} - \delta \tag{2.6}$$

When equation (2.4) is rewritten to equation (2.6) and, for both mixers, the liquid slug length is plotted against the ratio of the superficial liquid velocity U_l and the gas bubble formation frequency F_b, Figure 2.3 is obtained. From this figure, it appears that there is a linear relationship between these parameters, implying that the dimensionless cross-sectional bubble area A_b/A is constant for a wide range of bubble velocities. The correction on the liquid slug length to compensate for the volume of liquid present around the nose and tail of a gas bubble δ is also obtained from the fit. The differences between the slopes of the curves and between the values of δ are most likely due to experimental error. The larger

Table 2.2: The minimum and maximum values of the parameters obtained from image analysis are given. The gas bubble and liquid slug lengths L_b and L_s are given as a fraction of the channel width w, which was 100 µm for both mixers. The bubble velocity u_b and the gas bubble formation frequency are also given.

Mixer	L_b/w [-]	L_s/w [-]	$L_b/(L_b+L_s)$ [-]	u_b [m/s]	F_b [10^3 s^{-1}]
Cross	2.74-20.07	0.75-7.35	0.48-0.94	0.24-7.12	0.14-4.86
Smooth	7.69-25.41	1.33-25.29	0.49-0.93	0.54-4.44	0.22-2.11

Table 2.3: The minimum and maximum values the capillary, Reynolds and Weber numbers based on the liquid properties and the gas bubble velocity.

Mixer	Ca_b [-]	Re_b [-]	We_b [-]
Cross	$3{\cdot}10^{-3}$-$9.9{\cdot}10^{-2}$	16-474	0.05-47
Smooth	$8{\cdot}10^{-3}$-$6.2{\cdot}10^{-2}$	36-296	0.27-18

spread in the data obtained with the cross mixer is the result of a less uniform bubble and slug size distribution for a given set of flow rates. This is caused by the differences in bubble formation mechanisms in the two mixers, as described in Haverkamp *et al.* [16]

The sum of the volumes occupied by the nose and tail sections of the gas bubble and the volume of the part of the liquid slug surrounding them is $A_b(L_{nose}+L_{tail})$. The length of the nose of the gas bubble is L_{nose} and the length of its tail is L_{tail}, as indicated in Figure 2.1. The volume of liquid in this area is $A_b\delta$, so that the fraction of liquid in this volume is $\delta/(L_{nose}+L_{tail})$. For ease of calculation the shapes of the nose and tail sections of a bubble are assumed to be identical half ellipsoids with a cross-sectional area A_b. The total volume of the two halves is then $2A_b(L_{nose}+L_{tail})/3$ and $\delta/(L_{nose}+L_{tail})$ = 0.33. The lengths of the tails and noses of the gas bubbles have been estimated at both the largest and smallest bubble velocity used in this work. For these experiments the sum of the nose and tail lengths is 100 ± 10 µm and the value for $\delta/(L_{nose}+L_{tail})$ is then 0.5 ± 0.2. This is close to the value of 0.33 found if the nose and tail sections were shaped like half ellipsoids. It is concluded that a value for δ of 50 µm is realistic.

Literature data including measured values of A_b/A were all obtained for gas-liquid Taylor flow where inertial effects could be neglected. These show A_b/A to increase with

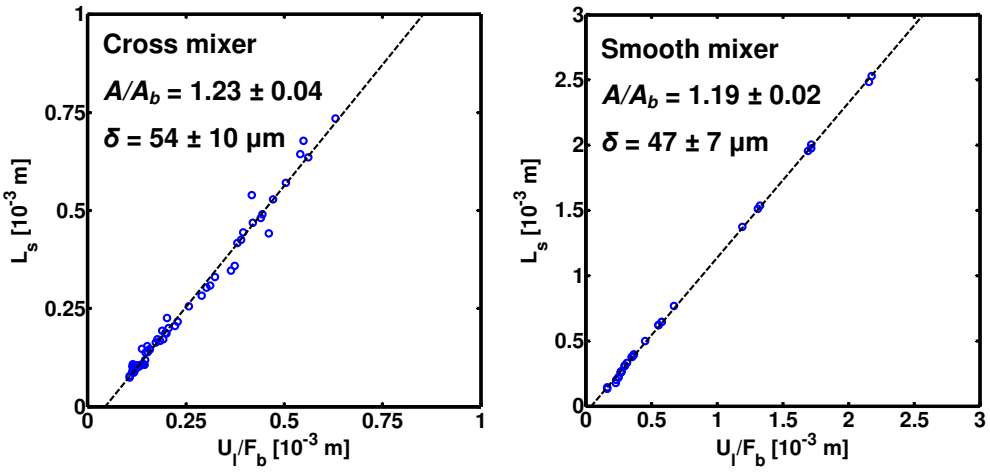

Figure 2.3: The liquid slug length L_s is plotted versus the superficial liquid velocity U_l divided by the gas bubble formation frequency F_b for both the cross (left) and the smooth (right) mixers. The dotted line represents the linear fit according to equation (2.6). The values of the fitted parameters A/A_b and δ and their 95 % confidence intervals are given in the figures.

increasing Ca_b [2,13]. However, although the capillary numbers used in these studies are in the same range as those used in this work, the Reynolds and Weber numbers covered in this work indicate that inertial effects are significant. The observation that the cross-sectional bubble area does not vary with varying bubble velocity when inertial effects are present, may be due to a geometric effect similar to that suggested by Aussillous and Quéré for channels with a circular cross-section [5].

Since the pressure at the imaging location is not known, the local superficial gas velocity is also not known. Therefore, the local superficial gas velocity is calculated from experimental data, the fitted values of A/A_b and δ, and equation (2.2). The gas hold-up was calculated from equation (2.5). The data were compared to the Armand correlation [17], which is given in equation (2.7).

$$\varepsilon_g = 0.83 \frac{U_g}{U_g + U_l} \tag{2.7}$$

Figure 2.4 shows the gas hold-up as a function of the flow quality for both mixers. The Armand correlation and the parity line are also plotted.

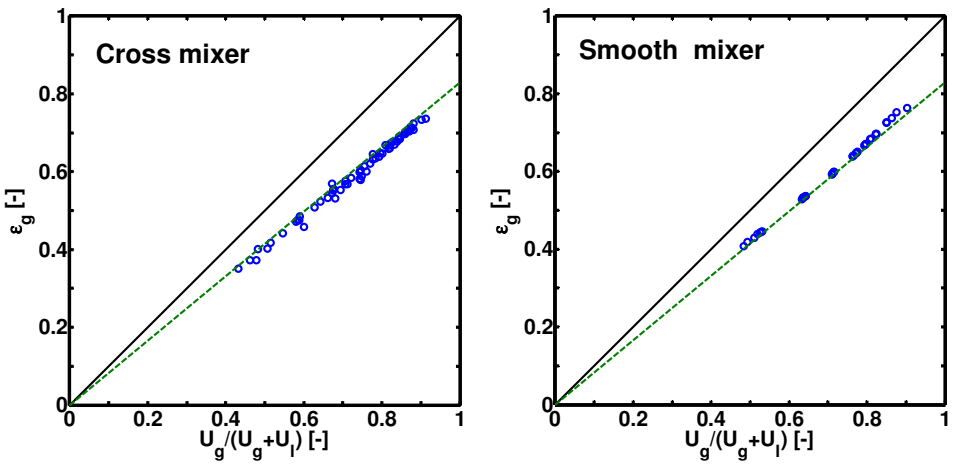

Figure 2.4: The gas hold-up, ε_g is plotted as a function of the flow quality, $U_g/(U_g+U_l)$ for both the cross (left) and the smooth mixer (right). The Armand correlation (dashed line) and the parity line (solid line) are also plotted.

The Armand correlation was obtained for air-water Taylor flows in a horizontally oriented, smooth, brass tube with an inner diameter of 26 mm. The gas hold-up was estimated from the weight of the tube and was measured at various gas qualities. Correlating the two parameters resulted in the Armand correlation, without addressing the physical interpretation of the constant. Upon comparing equation (2.5) to the Armand correlation, the constant 0.83 in their correlation can be considered to be the dimensionless cross-sectional bubble area A_b/A. This value is close to the values obtained for A_b/A in this work: 0.82 for the cross mixer and 0.84 for the smooth mixer. Chung *et al.* [18] obtained similar linear relationships for a nitrogen-water flow in glass capillaries of circular cross-section with diameters of 500 and 251 μm. However, for smaller diameters (100 and 50 μm) they obtained a non-linear relationship between the gas hold-up and flow quality, which is not confirmed by the data in this work at similar channel diameters. Chung *et al.* suggest that the difference in their results for the various channel diameters might be due to limitations of their set-up. For large bubble velocities and liquid hold-ups in the 100 and 50 μm channels, it might be possible that their imaging system does not capture all the bubbles passing the measurement location, thus underestimating the gas hold-up. Serizawa *et al.* [19] have verified the Armand correlation for an air-water flow in a silica capillary of circular cross-section with an internal diameter of 20 μm. Ide *et al.* [20] performed experiments with nitrogen-water Taylor flow in a glass channel with a circular cross-sectional area and a diameter of 100 μm. They found the gas hold-up as a function of $U_g/(U_g+U_l)$ to vary with the volume of gas in between the gas control valve and the gas-liquid mixer. When there was only a small volume of gas between the gas control valve and the gas-liquid mixer, their experiments confirmed the Armand correlation.

The validity of the Armand correlation in both this work and in literature for horizontal air-water and nitrogen-water Taylor flows implies that the liquid film thickness occupies a fixed fraction of the channel cross-section over a wide range of channel diameters and bubble velocities. This is in agreement with the qualitative analysis of Aussillous *et al.* [5] that, for Taylor flows with significant inertial effects, the liquid film thickness converges to a fixed fraction of the channel width.

2.5 Conclusions

In small reactor channels operated under Taylor flow, conditions are often such that inertial effects can not be ignored, so that classical lubrication theory can no longer be used for estimating the liquid film thickness. Furthermore, the cross-sectional area of these channels in monolithic reactors and microfluidic devices are often square or rectangular. Therefore, in this work, the gas hold-up and its relation to the liquid film thickness are studied in channels with a rectangular cross-sectional area of 100x50 μm^2 under conditions where inertial effects are significant.

A mass balance based model for Taylor flow without flow in the liquid film was used to calculate the local superficial gas velocity and the gas hold-up from data obtained from image analysis. Experimental data are obtained for a nitrogen-water system and bubble velocities range from 0.24 to 7.12 m/s. The gas hold-up as a function of flow quality follows Armand's experimentally obtained correlation.

The model shows that the validity of the Armand correlation implies that the fraction of cross-sectional channel area occupied by the liquid film is not dependent on the bubble velocity. In literature, the Armand correlation is also obtained for nitrogen-water and air-water Taylor flows for a wide range of bubble velocities and channel diameters. This indicates that the liquid film thickness is not only independent of the bubble velocity, but also occupies a fixed fraction of the channel cross-section independent of the channel diameter. This behaviour differs from the results reported for viscous fluids, where inertial effects are not significant, and the fraction of cross-sectional channel area occupied by the liquid film increases with increasing bubble velocity.

Nomenclature

A area of the channel cross-section [m^2]

A_b area of the bubble cross-section [m^2]

Bo Bond number [-]

Ca_b capillary number based on the properties of the liquid and the gas bubble velocity [-]

D_h hydraulic diameter of the channel [m]

F_b bubble formation frequency [s^{-1}]

g gravitational constant [m/s^2]

L_b length of a gas bubble [m]

L_{nose} length of the nose of a gas bubble [m]

L_s length of a liquid slug [m]

L_{tail} length of the tail of a gas bubble [m]

Re_b Reynolds number based on the properties of the liquid and the gas bubble velocity [-]

u_b velocity of a gas bubble [m/s]

u_f average velocity of the liquid in the film based on the cross-sectional channel area occupied by the liquid film [m/s]

U_g local superficial gas velocity [m/s]

U_g^0 superficial gas velocity at a temperature of 20^0C and a pressure of 1 bar [m/s]

U_l superficial liquid velocity [m/s]

w width of the channel [m]

We_b Weber number based on the properties of the liquid and the gas bubble velocity [-]

Greek symbols

δ correction on slug length for the liquid in the slug surrounding the nose and tail of a gas bubble [m]

ε_g gas hold-up [-]

μ_l viscosity of the liquid [Pa·s]

ρ_l density of the liquid [kg/m^3]

ρ_g density of the gas [kg/m^3]

σ surface tension [N/m]

subscripts

b gas bubble

f liquid film

g gas

l liquid

s liquid slug

References

[1] Thulasidas, T. C., Abraham, M. A., Cerro, R. L., Flow patterns in liquid slugs during bubble-train flow inside capillaries. *Chem. Eng. Sci.*, 52(17), 2947-2962, 1997

[2] Kolb, W. B., Cerro, R. L., Coating the inside of a capillary of square cross section. *Chem. Eng. Sci.*, 46(9), 2181-2195, 1991

[3] Berčič, G., Pintar, A., The role of gas bubbles and liquid slug lengths on mass transport in the taylor flow through capillaries. *Chem. Eng. Sci.*, 52(21-22), 3709-3719, 1997

[4] Bretherton, F. P., The motion of long bubbles in tubes. *J. Fluid. Mech.*, 10, 166-188, 1961

[5] Aussillous, P., Quéré, D., Quick deposition of a fluid on the wall of a tube. *Phys. Fluids*, 12(10), 2367-2371, 2000

[6] Taylor, G. I., Deposition of a viscous fluid on the wall of a tube. *J. Fluid Mech.*, 10(2), 161-165, 1961

[7] Kreutzer, M. T., Kapteijn, F., Moulijn, J. A., Kleijn, C. R., Heiszwolf, J. J., Inertial and interfacial effects on pressure drop of Taylor flow in capillaries. *AIChE Journal*, 51(9), 2428-2440, 2005

[8] Heil, M., Finite Reynolds number effects in the Bretherton problem. *Phys. Fluids*, 13(9), 2517-2521, 2001

[9] Giavedoni, M. D., Saita, F. A., The axisymmetric and plane cases of a gas phase steadily displacing a Newtonian liquid - A simultaneous solution of the governing equations. *Phys. Fluids*, 9(8), 2420-2428, 1997

[10] Giavedoni, M. D., Saita, F. A., The rear meniscus of a long bubble steadily displacing a Newtonian liquid in a capillary tube. *Phys. Fluids*, 11(4), 786-794, 1999

[11] Kolb, W. B., Cerro, R. L., The motion of long bubbles in tubes of square cross section. *Phys. Fluids*, 5(7), 1549-1557, 1993

[12] Hazel, A. L., Heil, M., The steady propagation of a semi-infinite bubble into a tube of elliptical or rectangular cross-section. *J. Fluid. Mech.*, 470, 91-114, 2002

[13] Thulasidas, T. C., Abraham, M. A., Cerro, R. L., Bubble-train flow in capillaries of circular and square cross section. *Chem. Eng. Sci.*, 50(2), 183-199, 1995

[14] Ratulowski, J., Chang, H. C., Transport of gas bubbles in capillaries. *Phys. Fluids*, 1(10), 1642-1655, 1989

[15] Kreutzer, M. T., Kapteijn, F., Moulijn, J. A., Heiszwolf, J. J., Multiphase monolith reactors: Chemical reaction engineering of segmented flow in microchannels. *Chem. Eng. Sci.*, 60(22), 5895-5916, 2005

[16] Haverkamp, V., Hessel, V., Löwe, H., Menges, G., Warnier, M. J. F., Rebrov, E. V., De Croon, M. H. J. M., Schouten, J. C., Liauw, M. A., Hydrodynamics and mixer-induced bubble formation in micro bubble columns with single and multiple channels. Chem. Eng. Technol., 29(9), 1015-1026, 2006

[17] Armand, A. A., The resistance during the movement of a two-phase system in horizontal pipes. *Izv. Vses. Teplotekh. Inst.*, 1, 16-23, 1946

[18] Chung, P. M. Y., Kawaji, M., The effect of channel diameter on adiabatic two-phase flow characteristics in microchannels. *Int. J. Multiphase Flow*, 30(7-8 SPEC. ISS.), 735-761, 2004

[19] Serizawa, A., Feng, Z., Kawara, Z., Two-phase flow in microchannels. *Experimental Thermal and Fluid Science*, 26(6-7), 703-714, 2002

[20] Ide, H., Kimura, R., Kawaji, M., Optical Measurement of Void Fraction and Bubble Size Distributions in a Microchannel. *Heat Transfer Engineering*, 28(8), 713-719, 2007

Chapter 3

Pressure drop of gas-liquid Taylor flow in round micro capillaries for low to intermediate Reynolds numbers

This chapter has been published as:

Warnier, M.J.F., De Croon, M.H.J.M., Rebrov, E.V., Schouten, J.C., Pressure drop of gas-liquid Taylor flow in round micro-capillaries for low to intermediate Reynolds numbers. *Microfluid. Nanofluid.*, 2009, *in press*

Abstract

In this paper a model is presented that describes the pressure drop of gas-liquid Taylor flow in round capillaries with a channel diameter typically less than 1 mm. The analysis of Bretherton [1] for the pressure drop over a single gas bubble for vanishing liquid film thickness is extended to include a non-negligible liquid film thickness using the analysis of Aussillous and Quéré [3]. This result is combined with the Hagen-Poiseuille equation for liquid flow using a mass balance based Taylor flow model previously developed by the authors [4]. The model includes the effect of the liquid slug length on the pressure drop similar to the model of Kreutzer *et al.* [2]. Additionally, the gas bubble velocity is taken into account, thereby increasing the accuracy of the pressure drop predictions compared to those of the model of Kreutzer *et al.* Experimental data were obtained for nitrogen-water Taylor flow in a round glass channel with an inner diameter of 250 μm. The capillary number Ca_{gl} varied between $2.3 \cdot 10^{-3}$ and $8.8 \cdot 10^{-3}$ and the Reynolds number Re_{gl} varied between 41 and 159. The presented model describes the experimental results with an accuracy of ± 4% of the measured values.

3.1 Introduction

A gas-liquid flow moving through one or several small channels (diameters are typically < 1 mm) is often encountered in micro reactors or in micro scaled heat transfer equipment. An important design parameter for these type of devices is the pressure drop and not only for dimensioning of compressors and pumps and operation of the device. If the pressure drop is a significant fraction of the channel inlet pressure, then gas phase expansion along the channel length is not negligible. The values of all hydrodynamic parameters depending on the volumetric gas flow rate, such as mass and heat transfer coefficients, are therefore also a function of the axial position in the channel. Therefore, the pressure profile needs to be known in order to properly determine reactor performance.

Most experimental work available in the literature concerning pressure drop of gas-liquid flows in small channels covers a span of flow patterns. It should be noted that in this context small channels are defined as channels in which surface tension forces dominate gravitational forces [5]. The pressure drop is usually described with a flow pattern independent correlation based on either a Lockhart-Martinelli [6] or a homogeneous flow type of approach [7,8,9]. The accuracy with which these correlations predict experimental results is usually not satisfactory and becomes worse when the correlation found by one author is used to predict the data of another. One reason for the failure of the Lockhart-Martinelli and homogeneous flow correlations at predicting the pressure drop of gas-liquid flows in small channels is the absence of the effect of surface tension on the pressure drop. Contrary to larger channels, for which these correlations were developed, the effect of surface tension on the pressure drop is not negligible compared to the influence of inertial and viscous forces. Chen *et al.* [10] therefore developed a homogeneous flow type correlation for channels with a diameter smaller than 10 mm that includes surface tension effects in the form of Bond and Weber numbers. They collected 11 data sets from literature and compared their correlation and several other homogeneous flow and Lockhart-Martinelli type correlations to the data sets and none of them were capable of accurately predicting the pressure drops. The failure of the Lockhart-Martinelli and homogeneous flow type models in predicting pressure drops of gas-liquid flows in small channels, even when including surface tension effects, suggests that models are needed which take more details of the hydrodynamics, such as the spatial gas-liquid distribution and the velocity distribution of both phases, into account. This also means that there will not be one correlation or model capable of describing the pressure drop for all possible flow patterns, but that a detailed

pressure drop model has to be developed for each individual flow pattern. In this respect, it should be noted that Lockhart and Martinelli themselves state that “slug flow, in which alternate slugs of liquid and gas move down the tube, is eliminated from consideration” in the development of their model [6].

The focus in this work will henceforth be on obtaining a model for the pressure drop of gas-liquid Taylor flow in channels with a diameter smaller than 1 mm. The reason for considering gas-liquid Taylor flow in favor of other regimes is that it is one of the main flow regimes of interest for performing gas-liquid and gas-liquid solid reactions in micro structured reactors and monoliths [11,12,13,5]. The gas-liquid Taylor flow regime consists of an alternating sequence of gas bubbles and liquid slugs moving through a small channel. The length of the gas bubbles is larger than the channel diameter and a thin liquid film separates the gas bubbles from the channel walls. Furthermore, the liquid in the slugs forms recirculation cells for capillary numbers ($Ca_b = \mu u_b/\sigma$) smaller than 0.5 [14,15]. This further improves radial mass transfer rates compared to those of mass transfer driven solely by diffusion because of convection of liquid to and from the channel wall at, respectively, the back and front of the gas bubbles.

3.2 Previous work on pressure drop in gas-liquid Taylor flow

3.2.1 The pressure drop over a single gas bubble

The thickness of the liquid film surrounding a Taylor gas bubble is a defining parameter for describing the hydrodynamics of gas-liquid Taylor flow. It has been the subject of study since Fairbrother and Stubbs [16] first showed that a single bubble in a small diameter tube moves faster than the average velocity in the tube. The liquid film around the gas bubble causes the bubble to move through a smaller cross-section than that of the channel. Fairbrother and Stubbs found the excess velocity of the bubble to be a function of the capillary number.

Bretherton [1] expanded on this work and analytically derived an expression for the liquid film thickness in channels with a circular cross-section as a function of the capillary number. Bretherton’s analysis is valid for very small liquid film thickness d_f and in absence of

significant inertial and gravitational forces, i.e. $Ca_b \rightarrow 0$ and $We_b=\rho_l D_h u_b^2/\sigma << 1$, and results in:

$$\frac{d_f}{D_c} = 0.67 Ca_b^{\frac{2}{3}} \tag{3.1}$$

In the same work Bretherton also presented an expression for the pressure drop over a single Taylor gas bubble moving through a liquid filled channel with a circular cross-section:

$$\Delta P_b = 7.16\left(3Ca_b\right)^{\frac{2}{3}} \frac{\sigma}{D_c} \tag{3.2}$$

Several authors making use of finite element calculations have confirmed the results from Bretherton's analysis for both the liquid film thickness and the pressure drop over a Taylor gas bubble for low capillary numbers ($Ca_b < 5 \cdot 10^{-3}$). For larger capillary numbers, where the liquid film occupies a significant portion of the channel ($d_f > 0.02 D_c$), deviations from Bretherton's equations are observed, which was already indicated by Bretherton himself [1]. A few authors have also taken inertial effects into account in their finite element calculations, indeed finding deviations from Bretherton's equations as the capillary number increases [17,18,19,20,21]. However, none of these authors suggests new expressions for predicting the liquid film thickness and the pressure drop over a Taylor gas bubble when the liquid film thickness occupies a significant portion of the channel and/or inertial effects are significant. Aussillous and Quéré [3] have applied a scaling analysis to Bretherton's result for the liquid film thickness to account for both effects. They did not, however, discuss the implications of their work for the pressure drop over a Taylor gas bubble. They also did not quantify their results other than the effect of non-negligible liquid film thickness, for which they fitted the result of their scaling analysis to Taylor's data [22] to obtain:

$$\frac{d_f}{D_c} = \frac{0.67 Ca_b^{\frac{2}{3}}}{1 + 3.34 Ca_b^{\frac{2}{3}}} \tag{3.3}$$

This result is consistent with Bretherton's result, since equation (3.3) approaches equation (3.1) for $Ca_b \rightarrow 0$. They found the range of maximum Ca_b for which equation (3.3) described their experimental results to scale with $(Ca_b/Re_b)^{0.75}$. Although the exact values of Ca_b and

Re_b for which equation (3.3) can be applied thus depend on the physical properties of the liquid and the capillary radius, the equation was capable of describing all their experimental result for $Ca_b < 0.01$ and $Re_b < 150$.

3.2.2 Pressure drop model by Kreutzer *et al.* [2]

Bretherton's [1] work is rarely mentioned by authors who experimentally study pressure drop of gas-liquid flows in small channels, despite its success. On the other hand, the authors studying the problem using numerical methods do not compare their simulation results to experimental results, other than those of Bretherton and Taylor [22] for single bubbles.

A notable exception to the former statement is the work of Kreutzer *et al.* [2], who performed both numerical calculations including inertial effects as well as experiments on gas-liquid Taylor flow and compared their results to Bretherton's work. They identified two sources determining the pressure drop in a gas-liquid Taylor flow: (i) frictional pressure drop in the liquid slugs, and (ii) the pressure drop over the gas bubbles due to effects near the caps of the bubbles, for which the limit for $Ca_b \rightarrow 0$ was described by Bretherton. The pressure drop due to frictional losses in the gas bubbles was not taken into account, because it is negligible compared to the frictional losses in the liquid due to the large difference in viscosity of gas and liquid. In their experiments, the Bond number ($Bo=\rho_l g D_c^2/\sigma$) was in the order of 1 and gravity effects could therefore be neglected [23,24]. Kreutzer *et al.* did not include gravity effects in their numerical calculations and used a no-shear boundary condition at the gas-liquid interface. Due to the absence of gravity effects and shear of the gas bubble, the liquid film surrounding the gas bubbles is stagnant and does not contribute to the pressure drop.

Kreutzer *et al.* consider the liquid flow in the slugs to be a fully developed Hagen-Poiseuille flow which is disturbed by the gas bubbles, causing an excess pressure drop. The pressure drop for a fully developed Hagen-Poiseuille liquid flow in a pipe is given by:

$$-\frac{\mathrm{d}P}{\mathrm{d}z} = f_{Fanning}\left(\frac{1}{2}\rho U^2\right)\frac{4}{D_c} \tag{3.4}$$

where the Fanning friction factor $f_{Fanning}$ is equal to $16/Re$ for pipes with a circular cross-section and $Re=\rho D_c U/\mu$. Kreutzer *et al.* account for effects near the bubble caps by adding

an extra term to the friction factor, which is inversely proportional to the liquid slug length L_s and further depends on the physical properties of the liquid and the channel diameter. Their modified friction factor for the flow in the liquid slugs f_s is of the form:

$$f_s = \frac{16}{Re_{gl}}\left(1 + a\frac{D_c}{L_s}\left(\frac{Re_{gl}}{Ca_{gl}}\right)^b\right) \tag{3.5}$$

in which a and b are constants. The Fanning friction factor $f_{Fanning}$ in equation (3.4) is then replaced with the liquid slug friction factor f_s as defined in equation (3.5). The average velocity of the liquid in the slug is equal to the average cross-sectional velocity in the channel U_g+U_l. The equation for the pressure drop over the liquid slugs then becomes:

$$-\left(\frac{\mathrm{d}P}{\mathrm{d}z}\right)_s = f_s\left(\frac{1}{2}\rho_l\left(U_g + U_l\right)^2\right)\frac{4}{D_c} = \frac{2f_s Re_{gl}\mu_l\left(U_g + U_l\right)}{D_c^2} \tag{3.6}$$

where the Reynolds number is now given by $Re_{gl}=\rho_l D_c(U_g+U_l)/\mu_l$[1]. It should be noted that $f_s Re_{gl}$ in the right-hand term in equation (3.6) is a constant not depending on any velocity and equals 16 for a fully developed single phase Hagen-Poiseuille flow in a pipe with a circular cross-section.

Since only a part of the channel length is occupied by liquid slugs, the pressure drop over the liquid slugs must be multiplied with the fraction of channel length occupied by the slugs, $L_s/(L_b+L_s)$, to obtain the pressure drop over the channel $(dP/dz)_c$:

$$-\left(\frac{\mathrm{d}P}{\mathrm{d}z}\right)_c = -\left(\frac{\mathrm{d}P}{\mathrm{d}z}\right)_s\left(\frac{L_s}{L_b + L_s}\right) \tag{3.7}$$

Footnote 1: Bretherton [1] and Aussillous and Quéré [3] base their Reynolds, Weber and capillary numbers on the bubble velocity u_b. Kreutzer et al. [2] base all these dimensionless numbers on the sum of the superficial gas and liquid velocities U_g+U_l. For negligible film thickness, these are equivalent since $u_b \rightarrow U_g+U_l$ for $d_f \rightarrow 0$. For non negligible liquid film thickness, the bubble velocity can be a significant amount larger than U_g+U_l, and care must be taken which velocity is used. In this work, the Reynolds, Weber and capillary numbers based on the bubble velocity are indicated by the subscript "b" and those based on U_g+U_l are indicated by the subscript "gl".

Kreutzer *et al.* performed both numerical calculations at various flow conditions and experiments at varying gas and liquid velocities using several liquids. They fitted the constants *a* and *b* in equation (3.5) to both data sets and the results are given in table 3.1. The pressure drop correlation fitted to their experiments predicts larger pressure drops for a given Taylor flow than the correlation fitted to their CFD simulations. They attribute the difference to Marangoni effects, where impurities in the gas and liquid may cause the gas-liquid surface to "harden" and the no-shear boundary condition at the gas-liquid interface should be replaced by a no-slip boundary condition. Kreutzer's experiments were performed for approximately $3 \cdot 10^{-3} < Ca_{gl} < 4 \cdot 10^{-2}$, $1.5 \cdot 10^{2} < Re_{gl} < 1.4 \cdot 10^{3}$, and $1 < We_{gl} < 15$. The value of constant *a* in equation (3.5) is either 0.17 or 0.07 depending on whether impurities are present or not. For Reynolds numbers close to unity, they suggest using equation (3.8) for the liquid slug friction factor instead of equation (3.5), which they obtained from rewriting equation (3.2) and further using equations (3.6) and (3.7).

Table 3.1 Values for the constants a and b in equation (3.5) in the model of Kreutzer et al. from both their experiments and numerical calculations [2].

	a	***b***
Numerical	0.07	0.33
Experimental	0.17	0.33

$$f_s = \frac{16}{Re_{gl}} \left(1 + \frac{7.16 D_c \left(3 Ca_b\right)^{\frac{2}{3}}}{32 L_s Ca_b} \right) \tag{3.8}$$

It should be noted that this result is based on Bretherton's analysis and is therefore only valid for very thin liquid films and thus for $Ca_b < 5 \cdot 10^{-3}$ and $We_b << 1$. Kreutzer *et al.* compared the pressure drop over a single Taylor gas bubbled obtained from numerical calculations for $Re_{gl} = 1$ to the values predicted using equation (3.2) and found a good agreement for $2 \cdot 10^{-3} \leq Ca_{gl} \leq 4 \cdot 10^{-2}$. This suggests that the applicability of (3.8) extends to $Ca_{gl} \leq 4 \cdot 10^{-2}$, however, no experiments were performed in order to validate this.

3.3 Motivation and scope of this work

Lockhart-Martinelli [6] and homogeneous flow type models fail to accurately predict the pressure drop of gas-liquid Taylor flow in small channels, because surface tension effects and/or hydrodynamic details of the flow, such as the spatial gas-liquid distribution and the velocity distributions of both phases, are not taken into account. Kreutzer *et al.* [2] presented a semi-empirical model that successfully described their data obtained from experiments for $Re_b > 150$. Lower Reynolds numbers can be easily achieved in channels with a diameter in the order of 100 µm or smaller. For Reynolds numbers in the order of 1, Kreutzer *et al.* presented a model for the pressure drop of gas-liquid Taylor flow based on Bretherton's [1] results for the pressure drop over a single gas bubble. However, the model was neither compared to experimental results nor to numerical calculations and no suggestions are made for a pressure drop model for Reynolds numbers in the range $1 < Re_b < 150$.

Therefore, in this work, a model is developed for describing the pressure drop of gas-liquid Taylor flow with negligible liquid film velocities for $Re_b < 150$ and $Ca_b < 0.01$ using the approach of Kreutzer *et al.* The extension of Bretherton's analysis by Aussillous and Quéré [3] is used to obtain an expression for the pressure drop over a single gas bubble accounting for non-negligible liquid film thickness. A mass balance based model for gas-liquid Taylor flow previously developed by the authors [4] is used to describe the fraction of channel length occupied by liquid having a non-zero velocity causing the liquid frictional pressure drop. The mass balance based model is then also used to obtain the pressure drop per unit channel length from the liquid frictional pressure drop and the pressure drop over a single gas bubble. The pressure drop model is then compared to data obtained from experiments with nitrogen/water Taylor flow in a glass capillary with a circular cross-section and a diameter of 250 µm. The results from these experiments are also compared to model predictions using the model by Kreutzer *et al.* and the Lockhart-Martinelli-Chisholm [6,25] correlation (the model is described in appendix 3.A) to determine if the newly developed model truly is a significant improvement compared to currently available models and often used correlations. Even though gas-liquid Taylor flow was not considered in the development of the Lockhart-Martinelli-Chisholm model [6], the model has been applied to the Taylor flow regime by various authors and is therefore considered in this work. The values of various hydrodynamic parameters are obtained from analysis of images of the flows. Since the pressure drop model is partly based on the mass balance based model, the latter is briefly discussed first.

3.4 Mass balance based model

Consider a gas-liquid Taylor flow moving through a channel with a cross-sectional area A. The gas bubbles have a velocity u_b, a length L_b and occupy a fraction of the cross-sectional area of the channel A_b/A. The liquid slugs have a length L_s. The flow is divided into unit cells consisting of one gas bubble, its surrounding liquid film and one liquid slug and the unit cell length is L_b+L_s (Figure 3.1).

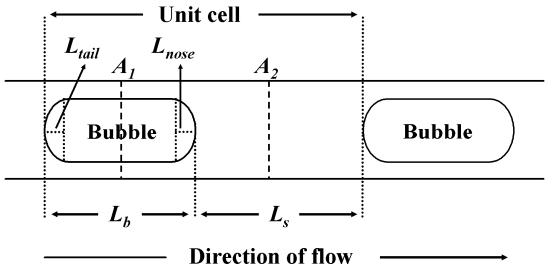

Figure 3.1 Schematic of Taylor flow showing the definitions of the unit cell, gas bubble length L_b and the liquid slug length L_s. The lengths of the nose L_{nose} and tail L_{tail} sections of the gas bubble are also indicated.

Continuity requires that the overall average velocity through any cross-section of the channel perpendicular to the direction of flow is the sum of the superficial gas U_g and liquid U_l velocities, which are based on the channel cross-section A. The flow through plane A_1 consists of the gas bubble moving with velocity u_b through a cross-section A_b, and the liquid film moving at an average velocity u_f through a cross-section A-A_b, giving:

$$\frac{A_b}{A}u_b + (1 - \frac{A_b}{A})u_f = U_g + U_l \tag{3.9}$$

The flow through plane A_2 consists solely of liquid which occupies the whole cross-section of the channel A and the average velocity of the liquid in the slug is therefore equal to U_g+U_l.

The superficial gas velocity U_g is equal to the bubble volume times the bubble formation frequency F_b, divided by the channel cross-sectional area A. If the bubble volume is taken to be the bubble length L_b times its cross-sectional area A_b, then it is overestimated because part of the volume $A_b(L_{nose}+L_{tail})$ consists of liquid. This liquid volume depends on

the bubble geometry, but can arbitrarily be written as the bubble cross-sectional area A_b times a length δ. This length δ is then a correction on the bubble length to account for the overestimation of the gas bubble volume if it were taken to be equal to $A_b L_b$. In case of a bubble with a circular cross-section and hemispherical bubble caps, it can be shown that δ is 1/3 of the bubble diameter D_b. The superficial gas velocity U_g is then given by:

$$U_g = \frac{A_b}{A} F_b \left(L_b - \delta \right) \tag{3.10}$$

The bubble formation frequency F_b is equal to the number of unit cells passing a certain location in the channel per unit of time, which is the reciprocal of the time it takes for a unit cell to travel its own length: $(L_b+L_s)/u_b$. The bubble formation frequency is therefore given by:

$$F_b = \frac{u_b}{L_b + L_s} \tag{3.11}$$

If equations (3.10) and (3.11) are substituted into equation (3.9), the following expression is obtained for the superficial liquid velocity U_l:

$$U_l = \frac{A_b}{A} F_b \left(L_s + \delta \right) + (1 - \frac{A_b}{A}) u_f \tag{3.12}$$

The velocity of the liquid in the film surrounding the bubble u_f is zero for horizontal Taylor flow as used in this work.

3.5 Pressure drop model

3.5.1 Model development

Aussillous and Quéré [3] incorporated the effect of a non-negligible liquid film thickness in Bretherton's [1] analysis by replacing the term $Ca_b^{2/3}$ with $Ca_b^{2/3}/(1+3.34 Ca_b^{2/3})$. Bretherton's result for the pressure drop over a single Taylor gas bubble can similarly be modified to account for a non-negligible liquid film thickness, giving:

$$\Delta P_b = 7.16 \frac{\sigma \left(3Ca_b\right)^{\frac{2}{3}}}{D_c \left(1+3.34Ca_b^{\frac{2}{3}}\right)} \tag{3.13}$$

The pressure drop over a unit cell, ΔP_{uc}, is the sum of the frictional pressure drop of the liquid flowing in the slug, ΔP_s, and the pressure drop over the Taylor gas bubble, ΔP_b. The flow of liquid in the slug is assumed to be fully developed and is therefore given by the Hagen-Poiseuille equation. The deviations thereof near the bubble caps are exactly what are accounted for in Bretherton's analysis and are thus incorporated by ΔP_b. Continuity requires the average velocity in the liquid slug to be U_g+U_l. As shown in the derivation of the mass balance based model, to properly account for the total amount of liquid with an average velocity of U_g+U_l in one liquid slug, the liquid slug length is $L_s+\delta$. The frictional pressure loss in one liquid slug is then given by:

$$\Delta P_s = \left(\frac{16}{Re_{gl}}\right)\left(\frac{4}{D_c}\right)\left(\frac{1}{2}\rho_l \left(U_g+U_l\right)^2\right)\left(L_s+\delta\right) = \frac{32\mu_l \left(U_g+U_l\right)}{D_c^2}\left(L_s+\delta\right) \tag{3.14}$$

Note that the Reynolds number is based on the average velocity of the liquid U_g+U_l and is not equal to the bubble Reynolds number Re_b, which is based on u_b. The pressure drop over a unit cell is then given by:

$$\Delta P_{uc} = \Delta P_s + \Delta P_b = \frac{32\mu_l \left(U_g+U_l\right)}{D_c^2}\left(L_s+\delta\right) + 7.16 \frac{\sigma \left(3Ca_b\right)^{\frac{2}{3}}}{D_c \left(1+3.34Ca_b^{\frac{2}{3}}\right)} \tag{3.15}$$

The length of a unit cell is L_b+L_s and thus the number of unit cells per unit length of channel is $1/(L_b+L_s)$. The pressure drop over a unit length of channel, $-(dP/dz)_c$, is therefore given by:

$$-\left(\frac{\mathrm{d}P}{\mathrm{d}z}\right)_c = \frac{\Delta P_{uc}}{L_b + L_s} = \frac{1}{L_b + L_s}\left(\frac{32\mu_l\left(U_g + U_l\right)}{D_c^2}\left(L_s + \delta\right) + 7.16\frac{\sigma\left(3Ca_b\right)^{\frac{2}{3}}}{D_c\left(1 + 3.34Ca_b^{\frac{2}{3}}\right)}\right) \tag{3.16}$$

Equation (3.16) can be rewritten to:

$$-\left(\frac{\mathrm{d}P}{\mathrm{d}z}\right)_c = ... \\ ....\frac{32\mu_l\left(U_g + U_l\right)}{D_c^2}\left(\frac{L_s + \delta}{L_b + L_s}\right)\left(1 + 7.16\frac{D_c\sigma\left(3Ca_b\right)^{\frac{2}{3}}}{32\mu_l\left(U_g + U_l\right)\left(L_s + \delta\right)\left(1 + 3.34Ca_b^{\frac{2}{3}}\right)}\right) \tag{3.17}$$

This result can be interpreted as follows: the term $32\mu_l(U_g+U_l)/D_c^2$ is the pressure drop per unit length of liquid for a fully developed Hagen-Poiseuille liquid flow moving at the average velocity U_g+U_l. The term $(L_s+\delta)/(L_b+L_s)$ is the volumetric fraction of channel in which liquid is moving at an average velocity of U_g+U_l. Therefore, these two terms combined are the pressure drop per unit channel length based on a fully developed Hagen-Poiseuille in the liquid slugs. The remaining term in equation (3.17) accounts for the additional pressure drop over the gas bubbles per unit channel length.

It can be shown from the mass balance based model that $(L_s+\delta)/(L_b+L_s)$ can be rewritten to $U_l/(U_g+U_l)$. The part of equation (3.17) describing the frictional pressure drop over a unit channel length due to fully developed liquid flow can then be rewritten as follows:

$$\frac{32\mu_l\left(U_g + U_l\right)}{D_c^2}\left(\frac{L_s + \delta}{L_b + L_s}\right) = \frac{32\mu_l U_l}{D_c^2} \tag{3.18}$$

This result indicates that any change of the frictional pressure drop over a unit length of channel due to changing the liquids average velocity by varying the gas flow rate, is negated by the change of the volumetric channel fraction occupied by that liquid.

Furthermore, the group $\sigma/(\mu_l(U_g+U_l))$ in the third term on the right hand side of equation (3.17) is the inverse of the capillary number based on the average velocity in the channel, Ca_{gl}. This can be rewritten to the inverse of the capillary number based on the bubble velocity Ca_b using equation (3.9) for a stagnant liquid film:

$$\frac{\sigma}{\mu_l\left(U_g+U_l\right)}=\frac{A}{A_b}\frac{1}{Ca_b} \tag{3.19}$$

By substituting equations (3.18) and (3.19) into equation (3.17), the following expression for the frictional pressure drop over a unit length of channel is obtained:

$$-\left(\frac{\mathrm{d}P}{\mathrm{d}z}\right)_c=\frac{32\mu_l U_l}{D_c^2}\left(1+\frac{7.16\cdot 3^{\frac{2}{3}}}{32}\frac{D_c}{\left(L_s+\delta\right)}\left(\frac{A}{A_b}\right)\frac{1}{\left(Ca_b^{\frac{1}{3}}+3.34Ca_b\right)}\right) \tag{3.20}$$

The liquid slug friction factor f_s is then given by:

$$f_s=\frac{16}{Re_{gl}}\left(1+\frac{7.16\cdot 3^{\frac{2}{3}}}{32}\frac{D_c}{\left(L_s+\delta\right)}\left(\frac{A}{A_b}\right)\frac{1}{\left(Ca_b^{\frac{1}{3}}+3.34Ca_b\right)}\right) \tag{3.21}$$

The cross-sectional area of the bubble A_b directly depends on the liquid film thickness. The corrected liquid slug length $L_s+\delta$ also depends on the bubble diameter and thus on the liquid film thickness. Both parameters can therefore be expressed as a function of the bubble velocity u_b using Aussillous and Quéré's result given in equation (3.3) and this can be substituted into equations (3.20) and (3.21). At first glance, this would result in the pressure drop being a complicated function of the capillary number and thus of the bubble velocity.

However, the term $(L_s+\delta)^{-1}(A/A_b)$ in equations (3.20) and (3.21) can be rewritten as a function of the superficial liquid velocity U_l and the bubble frequency F_b using equation (3.12) for a stagnant liquid film:

$$\frac{1}{\left(L_s+\delta\right)}\frac{A}{A_b}=\frac{F_b}{U_l} \tag{3.22}$$

Although it is not clear at first glance, the combined term $(L_s+\delta)^{-1}(A/A_b)$ in equations (3.20) and (3.21) is not a function of bubble velocity and thus is not dependent on the pressure and this simplifies the calculation of the pressure profiles. Substituting this result into equations (3.20) and (3.21) gives:

$$-\left(\frac{\mathrm{d}P}{\mathrm{d}z}\right)_c=\frac{32\mu_l U_l}{D_c^2}\left(1+\frac{7.16\cdot 3^{\frac{2}{3}}}{32}\frac{D_c F_b}{U_l}\frac{1}{\left(Ca_b^{\frac{1}{3}}+3.34Ca_b\right)}\right) \tag{3.23}$$

and

$$f_s=\frac{16}{Re_{gl}}\left(1+\frac{7.16\cdot 3^{\frac{2}{3}}}{32}\frac{D_c F_b}{U_l}\frac{1}{\left(Ca_b^{\frac{1}{3}}+3.34Ca_b\right)}\right) \tag{3.24}$$

respectively. Note that, apart from the constant 3.34, none of the other constants in equations (3.23) and (3.24) were obtained from a fitting procedure. The constant 3.34 was obtained by Aussillous and Quéré [3] from fitting their equation to the data of Taylor [22].

3.5.2 Comparison with the model of Kreutzer *et al.* [2]

Kreutzer *et al.* [2] found an expression for the liquid slug friction factor based on Bretherton's [1] analysis as given in equation (3.8). Bretherton's analysis is valid for vanishing liquid film thickness and thus for $Ca_b \rightarrow 0$. The liquid slug friction factor obtained in this work as given in equation (3.21) can also be evaluated for these conditions. For $Ca_b \rightarrow 0$, the liquid film

thickness approaches zero and the bubble cross-sectional area A_b approaches the channel cross-sectional area A. Furthermore, $Ca_b^{1/3} >> 3.34 Ca_b$ and equation (3.21) then becomes:

$$f_s = \frac{16}{Re}\left(1 + \frac{7.16 \cdot 3^{\frac{2}{3}}}{32}\frac{D_c}{\left(L_s+\delta\right)}\frac{1}{Ca_b^{\frac{1}{3}}}\right) \tag{3.25}$$

The only difference between equations (3.25) and (3.8) is that in Kreutzer *et al.*'s result, using Bretherton's analysis, the liquid slug length is given by L_s and in our work it is defined as $L_s+\delta$. It is not exactly clear how Kreutzer *et al.* have defined their slug length. In this work, it is defined as the shortest distance between the tail section of a gas bubble and the nose section of the trailing bubble. Kreutzer *et al.* take the volumetric fraction of the channel of liquid moving at an average velocity of U_g+U_l to be $L_s/(L_b+L_s)$. With our definition of L_s, the amount of liquid surrounding the nose and tail sections of the bubbles having a non-zero velocity, is not taken into account. As explained in the description of the mass balanced based model, this volume is accounted for when L_s is replaced with $L_s+\delta$. Applying this correction to equation (3.8) results in it being identical to equation (3.25) and the model developed in this work is indeed in accordance with Bretherton's work as applied by Kreutzer *et al.*

The same correction on the liquid slug length is applied to the model of Kreutzer *et al.* in order to be able to properly compare their results with those obtained in this work. Equations (3.6) and (3.7) can be combined and $(L_s+\delta)/(L_b+L_s)$ is substituted for $L_s/(L_b+L_s)$, following the same line of reasoning as in the derivation of equation (3.18), to give:

$$-\left(\frac{\mathrm{d}P}{\mathrm{d}z}\right)_c = \frac{2\mu_l U_l}{D_c^2} f_s Re_{gl} \tag{3.26}$$

Replacing L_s with $L_s+\delta$ in equation (3.5) then gives the following result for the slug friction factor f_s:

$$f_s = \frac{16}{Re_{gl}}\left(1 + a\frac{D_c}{L_s+\delta}\left(\frac{Re_{gl}}{Ca_{gl}}\right)^{0.33}\right) \tag{3.27}$$

These are the two equations that will be used further throughout this work as the adapted model of Kreutzer *et al.*

3.6 Experimental

All experiments were carried out with nitrogen gas and demineralised water at a temperature of 20±1 ^{0}C. The gas flow was regulated by a mass flow controller (Bronkhorst F-200C) and the superficial gas velocity was varied between 0.06 m/s and 0.33 m/s (these values are given at a temperature of 20^{0}C and a pressure of 1 bar). The superficial liquid velocity was varied between 0.10 and 0.34 m/s using an Isco 100DM syringe pump. The ranges of Reynolds, capillary and Weber numbers used in this work are given in Table 3.2.

The liquid flow was split into two equal flows which were contacted with the nitrogen flow at an angle of 90^0 with respect to the direction of flow of the nitrogen in a stainless steel cross-mixer (Valco ZX.5) (Fig. 3.2). The inner diameter of the channels in the cross-mixer was 250 µm.

A differential pressure sensor (Honeywell 26PC 05 KD, response time of 1 ms), measuring the pressure difference with ambient pressure, was connected at a distance of 13 cm downstream from the cross-mixer to ensure a fully developed Taylor flow passing the sensor. The flow then entered the glass capillary 3 cm downstream from the pressure sensor and exited the capillary under ambient conditions (T=293 K and P_{exit}=1.03·10^5 Pa).

Table 3.2 Superficial gas U_g and liquid U_l velocities used in this work. The capillary, Reynolds and Weber numbers covered in the experiments are also given. These numbers are based on the average velocity at the channel exit.

		min	max
U_g	[m/s]	0.06	0.33
U_l	[m/s]	0.10	0.34
$U_l/(U_g+U_l)$	[-]	0.33	0.84
Ca_{gl}	[-]	$2.3\cdot10^{-3}$	$8.8\cdot10^{-3}$
Re_{gl}	[-]	41	159
We_{gl}	[-]	0.09	1.41

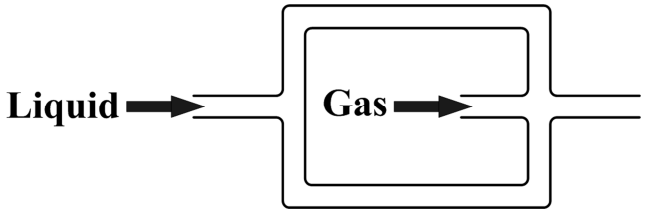

Figure 3.2 Schematic drawing of the cross-mixer. The liquid flow is split into two equal flows and contacted with the gas flow at an angle of 90°. All channels in the cross-mixer have a diameter of 250 µm.

The transparent, glass capillary had a length of 1 meter and a circular cross-section with an inner diameter of 250 µm. All of the connectors and tubing had an inner diameter of 250 µm.

The recording time for each of the studied 45 combinations of gas and liquid velocities was 2 seconds and the recording of the pressure signal was synchronized with the recording of the images. A Redlake MotionPro CCD camera connected to a Zeiss Axiovert 200 MAT inverted microscope was used to record images of the Taylor flow at a frame rate of 2500 frames per second. An exposure time of 20 µs was used, which was sufficiently short for preventing any significant motion blur. The length of one pixel represented 3.8 µm of channel length. A channel length of 3.04 mm was captured in the images of which the center point was located 29.5 cm downstream from the pressure sensor.

The gas bubbles in all the movies had a length shorter than the channel length captured in the images. The frame rate of 2500 frames per second was sufficiently short to ensure that no gas bubble travelled more than the unit cell length between the recordings of two consecutive images so that the individual bubbles could be tracked. For every movie, the length of every individual bubble was averaged over all frames in which it was completely visible. These values were then averaged to obtain the average bubble length L_b for that movie. The bubble frequency F_b is the number of tracked bubbles in one movie divided by the measurement time. The average velocity of a single bubble was obtained by dividing the distance travelled by its centre of mass in the movie by the time that the bubble was present in that movie. The bubble velocity was first determined for every single bubble and then averaged over all bubbles in one movie to give the average bubble velocity u_b. For each movie, the standard deviation of the bubble velocity was less than 0.5% of the average value, indicating that velocity fluctuations within the time of recording of one movie are negligible. The same procedure was followed for the liquid slugs for those movies in which

the length of the liquid slugs was smaller than the channel length captured by the images. For those movies in which the liquid slugs were not completely visible in one frame, equation (3.11) was used to calculate the slug length, since the bubble velocity, the bubble formation frequency, and the bubble length were known.

3.7 Results and discussion

In this section, for the sake of legibility, the adapted model of Kreutzer *et al.* [2] and that of Lockhart, Martinelli and Chisholm [6,25] will be referred to as, respectively, the "Kreutzer model" and the "LMC model".

A summary of the values obtained for the various hydrodynamic parameters from image analysis is given in Table 3.3.

The pressure measured at the sensor location varied between $0.93 \cdot 10^5$ and $2.34 \cdot 10^5$ Pa. Since the pressure at the channel exit equals $1.03 \cdot 10^5$ Pa, the volumetric gas flow rate at the pressure sensor was between 0.53 and 0.31 times that at the channel exit, assuming ideal isothermal expansion. Expansion of the gas phase between the two locations is therefore significant and the superficial gas velocity and the gas bubble velocity are not constant over the channel length. This is especially important for the LMC model (see appendix 3.A) and the model developed in this work (see equations (3.23) and (3.24)) since the pressure drop depends on, respectively, the superficial gas velocity and the gas bubble velocity. For these models, the pressure drop is a function of the axial position in the channel and the pressure is therefore not a linear function of the channel length. The pressure drop in the Kreutzer model, as described by equations (3.26) and (3.27), does not

Table 3.3 Summary of the minimum and maximum values obtained for the various hydrodynamic parameters from image analysis.

		min	max
L_s/D_h	[-]	3	23.95
L_b/D_h	[-]	1.77	3.56
$L_s/(L_b+L_s)$	[-]	0.46	0.93
u_b	[m/s]	0.15	0.47
F_b	[s^{-1}]	61	243

directly depend on the superficial gas nor on the bubble velocity. However, the correction on the liquid slug length δ is equal to $D_b/3$ for gas bubbles with hemispherical caps, which is a valid assumption in this work, and therefore depends on the liquid film thickness. The liquid film thickness is a function of the bubble velocity as given in equation (3.3), and so equation (3.27) is a function of the bubble velocity.

In order to be able to properly compare experimental results and model predictions, the pressure difference between the sensor location and the channel exit is calculated and compared to the measurement of the differential pressure sensor. This procedure requires calculation of the pressure profiles rather than the pressure drop. The pressure profiles are calculated numerically using the assumptions that:

- the gas phase obeys the ideal gas law,
- gas expansion is isothermal,
- absorption of the gas phase into the liquid has a negligible effect on the volumetric gas flow rate,
- the liquid phase is incompressible.

The boundary condition for all models is that the pressure at the exit of the channel equals $1.03 \cdot 10^5$ Pa. The superficial gas velocity at the exit conditions is therefore also known. For the LMC model the calculations are then straightforward, since the pressure drop depends on the local superficial gas velocity U_g (Appendix 3.A), which can easily be related to the pressure using the ideal gas law. Calculating the pressure profile from the model presented in this work as well as from the Kreutzer model requires an additional step since the pressure drop depends on the bubble velocity u_b and not directly on U_g. The bubble velocity is related to the superficial gas velocity and to the cross-sectional area of the gas bubble A_b as described in equation (3.9) and thus depends on the liquid film thickness. The liquid film thickness depends on the bubble velocity as described by Aussillous and Quéré (equation (3.3)). Therefore the bubble velocity and the liquid film thickness are calculated by an iteration of equations (3.9) and (3.3) for every axial position in the channel while calculating the pressure profile.

Kreutzer *et al.* [2] found two values for the constant *a* in equation (3.27): 0.17 and 0.07 based on, respectively, their experimental and numerical data. They explain the difference to be caused by impurities in the gas and/or liquid phases during the experiments. The experimental results obtained in this work are compared to the Kreutzer model for both values of *a* and the results are given in Figure 3.3. The Kreutzer model was developed for Re_{gl}>150 and indeed fails to describe the experimental data for Re_{gl}<150 using either value for *a*. The model consistently over predicts the experimental results for *a*=0.17 and under predicts them for *a*=0.07. The accuracy of the model predictions is expected to increase when Re_{gl} approaches and exceeds 150. The opposite trend is observed for *a*=0.17, *e.g.* for increasing Re_{gl} the deviation of the model predictions from the experimental values becomes larger. The expected trend is observed for *a*=0.07, but the scatter is large. Therefore, the constant *a* was fitted to the data in this work in order to improve the performance of the model. The best agreement between the Kreutzer model and the experimental data is obtained for *a*=0.10. Henceforth, this value of parameter *a* is used when comparing the Kreutzer model to the experimental data and the other two models.

Figure 3.4 shows the calculated pressure difference between the sensor location and the channel exit versus the

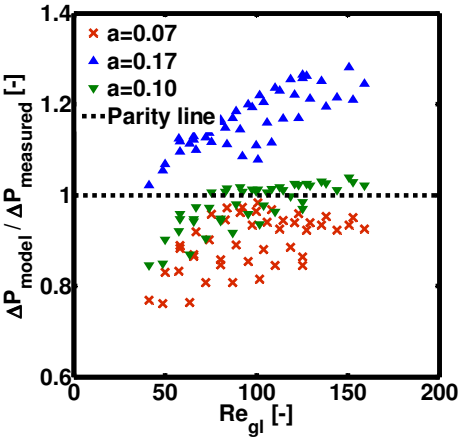

Figure 3.3 The pressure difference between the channel exit and the sensor location, as calculated with the model by Kreutzer et al. [2] divided by the measured pressure difference is plotted as a function of the Reynolds number Re_{gl} for three values of the constant a. The capillary number Ca_{gl} varied between $2.3 \cdot 10^{-3}$ and $8.8 \cdot 10^{-3}$.

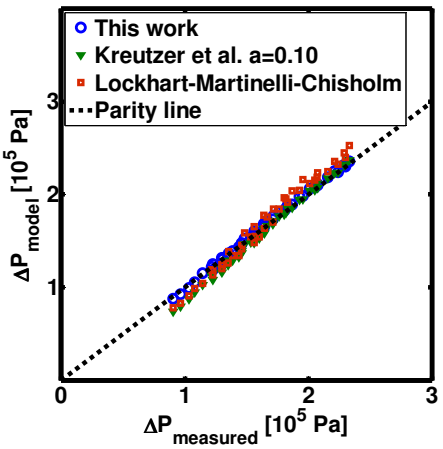

Figure 3.4: The pressure difference between the channel exit and the sensor location as calculated with the three models versus the measured pressure difference.

measured pressure difference for all three models. Figure 3.5 shows the same data, but then plotted as the ratio of the model predictions and the measured data versus Re_{gl} in order to better visualize the differences between model and measured values.

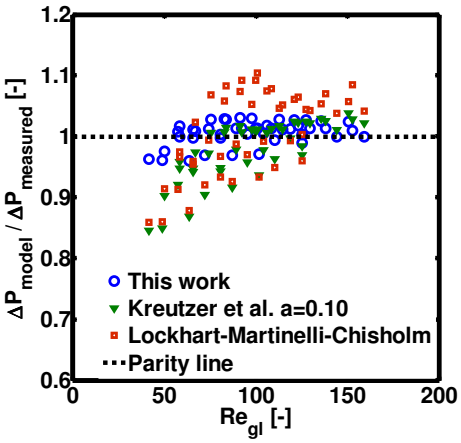

Figure 3.5 The ratio between the pressure difference between the channel exit and the sensor location as calculated with the three models and the measured pressure difference versus Re_{gl}. The capillary number Ca_{gl} varied between $2.3 \cdot 10^{-3}$ and $8.8 \cdot 10^{-3}$.

The LMC model under predicts the measured data at the smallest measured pressure differences, while it over predicts the data at the largest measured pressure differences. With increasing measured pressure difference, the accuracy of the model first increases until the model predicts larger values than the measured data. The accuracy of the model then decreases with increasing measured pressure difference. The LMC model predicts values of -14% to +10% of the measured value. The Kreutzer model is more accurate than the LMC model and its predictions vary between -15% and +4% of the measured value. Contrary to the predictions of the LMC model, the accuracy of the predictions by the Kreutzer model increases with increasing Re_{gl}, as expected. The model developed in this work predicts the pressure drop within a range of -4% to +3 % of the experimental data, which is a significantly smaller range than those of both the Kreutzer and LMC models.

The inability of the LMC model to accurately describe the experimental results obtained in this work confirms that both surface tension and hydrodynamic properties of the two phase flow, such as the spatial gas-liquid distribution and the velocity distributions of both phases, have to be considered when developing a model for the pressure drop of gas-liquid Taylor flow in small channels. The Kreutzer model does include surface tension effects and takes hydrodynamic properties into account in the form of the liquid slug length L_s, but it does not include the local velocities of the phases. Furthermore, it is a semi-empirical model and apart from the two values of the fitting parameter *a* reported by Kreutzer *et al.* themselves, a different value for *a* was found in this work. Kreutzer *et al.* state that they expect impurities in the gas and/or liquid phases in their experiments to be the cause of

finding a different value for *a* than the value obtained from their numerical calculations. The value found for *a* in this work is in between the limiting values obtained by Kreutzer *et al.* If impurities are indeed the cause of these differences, then the value of *a* obtained in this work implies some concentration of impurities present in our experiments as well. These effects should then also be of significance on the accuracy of the model developed in this

work. However, without taking possible impurities into account, the model developed in this work describes the experimental data within an error of ± 4%. This suggests that no significant concentration of impurities was present during our experiments and Marangoni effects therefore can not explain the different value of the fitting parameter *a* obtained in this work. It should be noted that the introduction of the group $a(Re/Ca)^{0.33}$ in the Kreutzer model is based on their experimental observations, but physical interpretation of the group $a(Re/Ca)^{0.33}$ is lacking. The parameter *a* may very well be a function of other hydrodynamic parameters causing the differences in values observed for *a.* In order to obtain an understanding of the nature of the fitting parameter *a,* the model developed in this work is compared in more detail with the Kreutzer model.

An expression for *a* is obtained from combining the expression for the liquid slug friction factor f_s obtained by Kreutzer *et al.* as given in equation (3.27) with the expression for f_s derived in this work as given in equation (3.21):

$$a = \frac{7.16 \cdot 3^{\frac{2}{3}}}{32}\left(\frac{A}{A_b}\right)\left(\frac{Ca_{gl}}{Re_{gl}}\right)^{\frac{1}{3}}\left(Ca_b^{\frac{1}{3}} + 3.34Ca_b\right)^{-1} \tag{3.28}$$

The parameter *a* thus depends on the liquid properties and is velocity dependent. A/A_b is a function of the liquid film thickness and thus of the bubble velocity following the equation of Aussillous and Quéré (equation (3.3)). The values of *a* can be calculated for all experiments performed in this work using the bubble velocities obtained from image analysis and the local superficial gas velocities at the imaging location. The latter is known from the pressure profiles and the ideal gas law. Note that these values of *a* are estimates, since *a* is a function of the axial position in the channel and only the values at the imaging location are used. The result is shown in Figure (3.6). When fitting the Kreutzer model to a data set, one value of *a* is obtained. It was already shown that the Kreutzer model described our experimental data best for a=0.10. The data displayed in Figure (3.6) are averaged in order

to be able to make the comparison with the one value obtained in the fitting procedure. When doing so, a=0.11 is obtained and this is, as expected, close to the value resulting from fitting the model to the experimental data. This result confirms that parameter a as described by equation (3.28) is a lumped parameter containing all velocity effects not explicitly taken into account in the Kreutzer model. The value found for a upon fitting the model to a data set depends on the exact combination of velocities covered in the experiments and the liquid properties and this can explain the differences between the value of a found in this work and the values found by Kreutzer *et al.* Furthermore, the variation of parameter a with varying bubble velocity decreases with increasing bubble velocity and thus with increasing Reynolds and capillary numbers. Although the capillary numbers used in this work are within the range of those used by Kreutzer *et al.*, the Reynolds numbers used in their experiments are larger than those in this work and the influence of the bubble velocity on the value of parameter a is less in their experiments. This may be the reason why Kreutzer *et al.* observed no or little influence of the bubble velocity on the value of parameter a. However, for Re_{gl} <150 the effect of the bubble velocity on the additional pressure drop caused by the presence of the gas bubbles has to be taken into account.

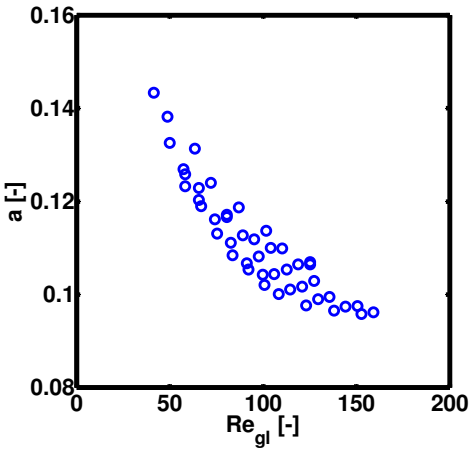

Figure 3.6 Parameter a in the model of Kreutzer et al. [2] is calculated using equation (28) and plotted as a function of Re_{gl}. The capillary number Ca_{gl} varied between $2.3\,10^{-3}$ and $8.8\,10^{-3}$.

3.8 Conclusions

In this paper a model has been developed to describe the pressure drop of gas-liquid Taylor flow in small round channels (diameter typically smaller than 1 mm). The model takes two sources of pressure drop into account: (i) frictional pressure drop caused by laminar flow in the liquid slugs, and (ii) an additional pressure drop over a single gas bubble due to the bubble disturbing the otherwise parabolic velocity profile in the liquid slugs. The pressure

drop over a single gas bubble is described by the classical theory of Bretherton [1] of which the applicability is extended up to a capillary number Ca_{gl} of 0.01 and Reynolds numbers Re_{gl} in the order of 10^2 using the scaling analysis of Aussilous and Quéré [3]. The pressure drop per unit channel length is obtained by combining the contributions of both sources using a mass balance based Taylor flow model previously developed by the authors [4]. The model shows that (i) the additional pressure drop caused by the presence of the gas bubbles depends on the bubble frequency and the bubble velocity, and (ii) its contribution to the overall pressure drop relative to that of the frictional pressure drop in the liquid phase decreases with increasing gas bubble velocity.

The model is compared to experimental data obtained for nitrogen-water Taylor flow in a glass channel with a circular cross-section and an inner diameter of 250 µm. The Reynolds number Re_{gl} is varied between 41 and 159 and the capillary number Ca_{gl} varied between $2.3 \cdot 10^{-3}$ and $8.8 \cdot 10^{-3}$. The model developed in this work describes the experimental data within an accuracy of ± 4% without fitting any of the constants to the data obtained in this work.

Both the model and the experimental data are compared to the Lockhart-Martinelli-Chisholm model [6,25] and the model of Kreutzer *et al.* [2]. The model of Kreutzer *et al.* is a semi-empirical model and is fitted to the experimental data obtained in this work and the fitted model predicts the measured pressure drop with increasing accuracy as the Reynolds number increases to 150. The Lockhart-Martinelli-Chisholm model was not developed for gas-liquid Taylor flow, which was explicitly indicated by the authors themselves [6]. Their model is therefore not expected to accurately describe the pressure drop in gas-liquid Taylor flow, yet it has been applied to this flow regime by other authors and was therefore included in this work. Contrary to the other two models, it takes neither surface tension nor any hydrodynamic properties of gas-liquid Taylor flow into account and, as expected, the values of the pressure drop predicted by the Lockhart-Martinelli-Chisholm model deviate more from the measured values than the predictions of the other two models.

The model of Kreutzer *et al.* has been specifically developed for gas-liquid Taylor flow for Reynolds numbers larger than 150 and considers the same two sources of pressure drop as the model developed in this work. Furthermore, both models similarly take the spatial gas-liquid distribution into account in the form of, respectively, the liquid slug length and the gas bubble frequency. The main difference between the two models is that the

dependence of the pressure drop on the gas bubble velocity is not incorporated in the model of Kreutzer *et al.*, while it is included in the model developed in this work. The decreasing accuracy of the model of Kreutzer *et al.* with decreasing Reynolds number, and thus with decreasing gas bubble velocity, is shown to be due to the model not taking the effect of the gas bubble velocity on the pressure drop into account. This result therefore shows that, other than the spatial distribution of the gas and liquid phases, the velocity distribution of the gas and liquid phases needs to be included when describing the pressure drop of gas-liquid Taylor flow in small channels.

The model developed in this work is valid for gas-liquid Taylor flow in round channels for $Ca_b < 0.01$, $Re_b < 150$ and negligible velocity of the liquid in the film surrounding the gas bubbles. When these conditions are met, the expression for the pressure drop over a single Taylor gas bubble is known from combining the analysis of Bretherton and that of Aussillous and Quéré, as shown in this work. Unfortunately, such an expression is not available when either the channel is not axisymetric, the liquid flow is not laminar, inertial effects are significant, or the liquid film surrounding the Taylor gas bubbles is not stagnant. Efforts to describe the pressure drop of gas-liquid Taylor taking one or more of these effects into account have been made, such as the model by Kreutzer *et al.* who developed their semi-empirical model when inertial effects are significant, but the understanding is still far from complete.

Nomenclature

a fit parameter [-]

A area of the channel cross-section [m^2]

A_b area of the bubble cross-section [m^2]

b fit parameter [-]

Bo Bond number [-]

Ca_b capillary number based on the liquid properties and the gas bubble velocity [-]

Ca_{gl} capillary number based on the liquid properties and the sum of the superficial gas and liquid velocities [-]

D_b gas bubble diameter [m]

D_c channel diameter [m]

d_f liquid film thickness [m]

F_b frequency of bubbles [s^{-1}]

$f_{Fanning}$ Fanning friction factor [-]

f_s slug friction factor [-]

g gravitational constant [m/s^2]

L_b length of a gas bubble [m]

L_{nose} length of the nose of a gas bubble [m]

L_s length of a liquid slug [m]

L_{tail} length of the tail of a gas bubble [m]

P pressure [Pa]

P_{exit} pressure at the channel exit [Pa]

Re_b Reynolds number based on the liquid properties and the gas bubble velocity [-]

Re_g Reynolds number based on the liquid properties and the superficial gas velocity [-]

Re_{gl} Reynolds number based on the liquid properties and the sum of the superficial gas and liquid velocites [-]

Re_l Reynolds number based on the liquid properties and the superficial liquid velocity [-]

u_b velocity of a bubble [m/s]

u_f average velocity of the liquid in the film based on the cross-sectional channel area occupied by the liquid film [m/s]

U_g superficial gas velocity [m/s]

U_l superficial liquid velocity [m/s]

We_b Weber number based on the liquid properties and the gas bubble velocity [-]

We_{gl} Weber number based on the liquid properties and sum of the superficial gas and liquid velocities [-]

z axial position in the channel [m]

Greek symbols

δ correction on slug length for the liquid in the slug surrounding the nose and tail of bubble [m]

μ_g viscosity of the gas [Pa·s]

μ_l viscosity of the liquid [Pa·s]

ρ_g density of the gas [kg/m^3]

ρ_l density of the liquid [kg/m^3]

σ surface tension [N/m]

χ Lockhart-Martinelli parameter [-]

ϕ_l Lockhart-Martinelli parameter [-]

Subscripts

b gas bubble

c channel

s liquid slug

uc unit cell

Abbreviations

LMC model The model of Lockhart, Martinelli and Chisholm [6,25]

Kreutzer model The model of Kreutzer *et al.* [2]

References

[1] Bretherton, F. P., The motion of long bubbles in tubes. *J. Fluid. Mech.*, 10, 166-188, 1961

[2] Kreutzer, M. T., Kapteijn, F., Moulijn, J. A., Kleijn, C. R., Heiszwolf, J. J., Inertial and interfacial effects on pressure drop of Taylor flow in capillaries. *AIChE Journal*, 51(9), 2428-2440, 2005

[3] Aussillous, P., Quéré, D., Quick deposition of a fluid on the wall of a tube. *Phys. Fluids*, 12(10), 2367-2371, 2000

[4] Warnier, M. J. F., Rebrov, E. V., De Croon, M. H. J. M., Hessel, V., Schouten, J. C., Gas hold-up and liquid film thickness in Taylor flow in rectangular microchannels. *Chem. Eng. J.*, 135S, S153-S158, 2007

[5] Angeli, P., Gavriilidis, A., Hydrodynamics of Taylor flow in small channels: A review. *Proc. Inst. Mech. Eng. Part C J. Mech. Eng. Sci.*, 222(5), 737-751, 2008

[6] Lockhart, R. W., Martinelli, R. C., Proposed Correction of Data for Isothermal Two-Phase Component Flow in Pipes. *Chem. Eng. Prog.*, 45(1), 39-48, 1949

[7] Triplett, K. A., Ghiaasiaan, S. M., Abdel-Khalik, S. I., LeMouel, A., McCord, B. N., Gas-liquid two-phase flow in microchannels Part II: Void fraction and pressure drop. *Int. J. Multiphase Flow*, 25(3), 395-410, 1999

[8] Kawahara, A., Chung, P. M. Y., Kawaji, M., Investigation of two-phase flow pattern, void fraction and pressure drop in a microchannel. *Int. J. Multiphase Flow*, 28(9), 1411-1435, 2002

[9] Chung, P. M. Y., Kawaji, M., The effect of channel diameter on adiabatic two-phase flow characteristics in microchannels. *Int. J. Multiphase Flow*, 30(7-8 SPEC. ISS.), 735-761, 2004

[10] Chen, I. Y., Yang, K. S., Wang, C. C., An empirical correlation for two-phase frictional performance in small diameter tubes. *Int. J. Heat Mass Transf.*, 45(17), 3667-3671, 2002

[11] Kreutzer, M. T., Kapteijn, F., Moulijn, J. A., Heiszwolf, J. J., Multiphase monolith reactors: Chemical reaction engineering of segmented flow in microchannels. *Chem. Eng. Sci.*, 60(22), 5895-5916, 2005

[12] Hessel, V., Löwe, H., Angeli, P., Gavriilidis, A., Gas-liquid and gas-liquid-solid microstructured reactors: Contacting principles and applications. *Ind. Eng. Chem. Res.*, 44(25), 9750-9769, 2005

[13] Günther, A., Jensen, K. F., Multiphase microfluidics: From flow characteristics to chemical and materials synthesis. *Lab Chip Miniaturisation Chem. Biol.*, 6(12), 1487-1503, 2006

[14] Thulasidas, T. C., Abraham, M. A., Cerro, R. L., Flow patterns in liquid slugs during bubble-train flow inside capillaries. *Chem. Eng. Sci.*, 52(17), 2947-2962, 1997

[15] Kolb, W. B., Cerro, R. L., The motion of long bubbles in tubes of square cross section. *Phys. Fluids*, 5(7), 1549-1557, 1993

[16] Fairbrother, F., Stubbs, A. E., Studies in electro-endosmosis. Part VI. The "Bubble-tube" method of measurement. *J. Chem. Soc.*, 1, 527-529, 1935

[17] Giavedoni, M. D., Saita, F. A., The axisymmetric and plane cases of a gas phase steadily displacing a Newtonian liquid - A simultaneous solution of the governing equations. *Phys. Fluids*, 9(8), 2420-2428, 1997

[18] Ratulowski, J., Chang, H. C., Transport of gas bubbles in capillaries. *Phys. Fluids*, 1(10), 1642-1655, 1989

[19] Westborg, H., Hassager, O., Creeping motion of long bubbles and drops in capillary tubes. *J. Colloid Interface Sci.*, 133(1), 135-147, 1989

[20] Heil, M., Finite Reynolds number effects in the Bretherton problem. *Phys. Fluids*, 13(9), 2517-2521, 2001

[21] Fujioka, H., Grotberg, J. B., The steady propagation of a surfactant-laden liquid plug in a two-dimensional channel. *Phys. Fluids*, 17(8), 1-17, 2005

[22] Taylor, G. I., Deposition of a viscous fluid on the wall of a tube. *J. Fluid Mech.*, 10(2), 161-165, 1961

[23] Edvinsson, R. K., Irandoust, S., Finite-Element Analysis of Taylor Flow. *AIChE Journal*, 42(7), 1815-1823, 1996

[24] Hazel, A. L., Heil, M., The steady propagation of a semi-infinite bubble into a tube of elliptical or rectangular cross-section. *J. Fluid. Mech.*, 470, 91-114, 2002

[25] Chisholm, D., A theoretical basis for the Lockhart-Martinelli correlation for two-phase flow. *Int. J. Heat Mass Transf.*, 10(12), 1767-1778, 1967

Appendix 3.A

The Lockhart-Martinelli-Chisholm [6,25] approach is based on correlating the gas and liquid single phase pressure drops to give the two-phase pressure drop. For the gas phase, the single phase pressure drop is given by:

$$-\left(\frac{dP}{dz}\right)_g = \frac{32\mu_g U_g}{D_h^2} \tag{3.A1}$$

For the liquid phase, the single phase pressure drop is given by:

$$-\left(\frac{dP}{dz}\right)_l = \frac{32\mu_l U_l}{D_h^2} \tag{3.A2}$$

The Lockhart-Martinelli parameter χ is given by:

$$\chi^2 = \frac{\left(\frac{dp}{dz}\right)_l}{\left(\frac{dp}{dz}\right)_g} \tag{3.A3}$$

Chisholm [25] suggested the following equation for the Lockhart-Martinelli parameter ϕ_l^2:

$$\phi_l^2 = 1 + \frac{C}{\chi} + \frac{1}{\chi^2} \tag{3.A4}$$

in which $C = 5$ when the flow in both the gas and liquid phases are laminar, as is the case in this work. The two-phase pressure drop can then be calculated by:

$$-\left(\frac{dP}{dz}\right)_c = -\phi_l^2 \left(\frac{dP}{dz}\right)_l \tag{3.A5}$$

Chapter 4

On chip determination of pressure drop in gas-liquid Taylor flow

Abstract

In this chapter, a method is developed to obtain the pressure drop of gas-liquid Taylor flows in micro-channels of an arbitrary cross-sectional area by combining data obtained from analysis of images of the Taylor flows recorded at different locations in the channel with a mass balance based Taylor flow model already used and described in chapters 2 and 3. This method can be used for determining the pressure drop in micro-fluidic chips, where directly measuring the pressure or pressure drop is not always feasible, while imaging facilities often are available.

The method was applied to water/nitrogen Taylor flow in channels with square and rectangular cross-sectional areas of 50x50 μm^2 and 100x50 μm^2, respectively, and to isopropanol/nitrogen Taylor flow in a channel with a cross-sectional area of 100x50 μm^2. The experimental data were compared to predictions from the model of Kreutzer *et al.* [1], the Lockhart-Martinelli-Chisholm model [2,3] and the model developed in chapter 3.

From the results it can be concluded that the method developed in this chapter yields realistic values for the pressure drop of gas-liquid Taylor flow in micro-channels with a non-circular cross-sectional area. It, therefore, appears to be a viable method for determining the pressure drop of gas-liquid Taylor flow in micro-channels. However, a more firm validation of the method by comparison with data obtained by another measurement technique still needs to be done.

4.1 Introduction

Gas-liquid Taylor flows are encountered in microfluidic chips for a number of applications besides performing gas-liquid solid reactions. An overview of the various applications is given in the introduction of the review article by Günther and Jensen [4]. All these applications deal with movement of a fluid through one or several channels, which may be interconnected. Measuring the pressure in such a device and having an understanding of the pressure drop can be important for their design.

In microfluidic chips, the channels generally have a non-circular cross-section. Trapezoidal, triangular, square, and rectangular cross-sections are encountered. While mechanistic models are available for gas-liquid Taylor flow in microfluidic channels with a circular cross-sectional area, most notably the model developed in chapter 3 and the model Kreutzer *et al.* [1], such models are not available for other channel geometries. Furthermore, measuring the pressure and pressure drop in microfluidic chips is considerably more difficult than for larger channels, since pressure transducers can not easily be connected to the channels. Several methods for measuring the pressure and/or pressure drop in microfluidic devices have been developed based on a variety of principles. For instance, dynamic pressure drop variations were estimated from visual observation of deformation of red and white blood cells [5]. The local pressure in a microfluidic channel was determined by optically measuring the pressure dependent deformation of a membrane connected to a microfluidic channel with a tap line [6]. Differences in pressure drop over a gas bubble were determined by visual observation of gas bubbles moving through two parallel, connected channels [7]. The local pressure in a microfludic channel was measured by optically determining the volume of a known trapped quantity of air sealed off by a liquid plug in a section of the chip connected to a microfluidic channel [8].

In this chapter, an alternative method is presented for determining the pressure drop of gas-liquid Taylor flows in microchannels solely from data which can be obtained from analysis of images of gas-liquid Taylor flow recorded at various locations in a microfluidic channel. The main principle is rather straightforward. For a known gas feed flow rate at a certain reference pressure, the pressure at the imaging location can be estimated from the ideal gas law and the volumetric flow rate at the imaging location. The latter is equal to the number of gas bubbles passing that location per unit time multiplied by their average volume. The pressure profile can then be determined by varying the measurement location

over the channel length, for a given set of gas and liquid feed flow rates. The bubble formation frequency can easily be obtained from image analysis, but obtaining the gas bubble volume requires knowledge of the bubble shape, which is not easily obtained from the images, especially for channels with non-circular cross-sections. The bubble volume depends on the bubble cross-sectional area and the shape of the nose and tail sections of the bubbles. Data for the liquid film thickness are available for channels with a square cross-sectional area [9,10,11,12]. The data from the first three references regarding the dependence of the diagonal bubble diameter on the capillary number were fitted by Kreutzer *et al.* [13]. For other channel geometries, no such data are available.

However, in chapter 2 it was shown that the volumetric gas flow rate at the imaging location can be obtained from data available from image analysis and a Taylor flow mass balance, without a priori knowledge of the exact bubble geometry. The local superficial gas velocity will thus be determined for various locations in a given channel, for each set of gas and liquid velocities. The pressure profile over the channel length is then calculated using the ideal gas law. This method will be used to obtain the pressure drop data of water/nitrogen Taylor flow in channels with square and rectangular cross-sectional areas of 50x50 μm^2 and 100x50 μm^2, respectively, and of isopropanol/nitrogen Taylor flow in a channel with a cross-sectional area of 100x50 μm^2.

Neither pressure drop models specifically developed for gas-liquid Taylor flow in non-circular channels, nor experimental data sets containing both pressure drop data, as well as the details of the gas-liquid Taylor flows over the length of a channel, are currently available in literature. Therefore, the experimental data are compared to predictions from the model of Kreutzer *et al.* [1], the Lockhart-Martinelli-Chisholm model [2,3] and the model developed in chapter 3. None of these models were developed for channels with a non-circular cross-sectional and are, therefore, not expected to precisely describe the experimental data. However, some degree of accuracy is expected, since the order of magnitude of the pressure drop is determined by the liquid phase pressure drop and all models, in some form, account for the presence of the gas phase. The goal of comparing the experimental data to the various model predictions is not to accurately model the pressure drop of gas-liquid Taylor flow in in non-circular channels. Rather, the comparison is made to evaluate whether the data obtained with the new method are of comparable magnitude as the model predictions.

4.2 Pressure drop estimation from image analysis

Consider a gas-liquid Taylor flow moving through a channel with a cross-sectional area A. The gas bubbles have a velocity u_b, a length L_b and occupy a fraction of the cross-sectional area of the channel A_b/A. The liquid slugs have a length L_s. These definitions are illustrated schematically in Figure 4.1.

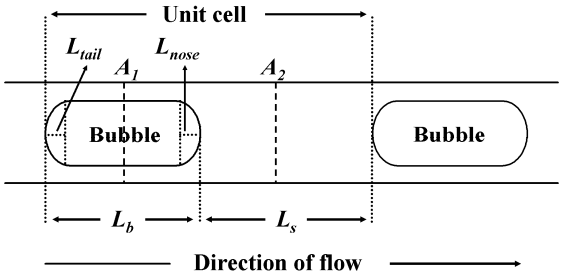

Figure 4.1: Schematic of Taylor flow showing the definitions of the unit cell, gas bubble length L_b and the liquid slug length L_s. The lengths of the nose L_{nose} and tail L_{tail} sections of the gas bubble are also indicated.

In chapter 2 it was shown that a mass balance through planes A_1 and A_2 yields the following equations for a gas-liquid Taylor flow with a stagnant liquid film surrounding the gas bubbles:

$$u_b = \frac{A}{A_b}\left(U_g + U_l\right) \tag{4.1}$$

$$u_b = F_b\left(L_b + L_s\right) \tag{4.2}$$

$$U_l = \frac{A_b}{A} F_b\left(L_s + \delta\right) \tag{4.3}$$

$$U_g = \frac{A_b}{A} F_b\left(L_b - \delta\right) \tag{4.4}$$

The superficial gas and liquid velocitis U_g and U_l, respectively, are based on the channel cross-sectional area A and F_b is the gas bubble formation frequency. The parameter δ is the correction on the liquid slug length to account for part of the volume $A_b(L_{nose}+L_{tail})$ consisting of liquid with a non zero velocity. This liquid volume depends on the bubble geometry, but can arbitrarily be written as the bubble cross-sectional area A_b times a length δ (see chapter 2 for more details).

In chapter 2, it was also shown that the cross-sectional bubble area A_b and the correction on the liquid slug length δ did not vary significantly with the gas bubble velocity, for nitrogen-water flows in rectangular channels with a cross-sectional area of 100x50 μm^2. The parameters A_b/A and δ can, therefore, be obtained from a linear fit of the liquid slug length L_s against the superficial liquid velocity divided by the bubble formation frequency F_b. The superficial gas velocity at the imaging location can then be calculated using equation (4.4). The ideal gas law is then used to calculate the pressure at the imaging location $P_{imaging}$, resulting in equation (4.5). The pressure profile over the channel length, and thus the pressure drop, can then be obtained by varying the imaging location along the channel length for a given set of gas and liquid velocities.

$$P_{imaging} = \frac{A U_g^0 P^0}{A_b F_b \left(L_b - \delta \right)} \tag{4.5}$$

4.3 Gas-liquid Taylor flow pressure drop models

The experimental results will be compared to the values predicted by the model developed in chapter 3, the model of Kreutzer *et al.* [1], and the Lockhart-Martinelli-Chisholm [2,3] model as described in Appendix 3.A. For the sake of legibility, the models will henceforth be referred to as, respectively, the Warnier model, the Kreutzer model, and the LMC model. The Warnier model is given in equation (4.6) and the Kreutzer model, which was slightly modified for the sake of compatibility with the Taylor flow mass balance, is given in equation (4.7).

$$-\left(\frac{\mathrm{d}P}{\mathrm{d}z}\right)_{Warnier} = \frac{32\mu_l U_l}{D_h^2}\left(1+\frac{7.16\cdot 3^{\frac{2}{3}}}{32}\frac{D_h F_b}{U_l}\frac{1}{\left(Ca_b^{\frac{1}{3}}+3.34Ca_b\right)}\right) \tag{4.6}$$

$$-\left(\frac{\mathrm{d}P}{\mathrm{d}z}\right)_{Kreutzer} = \frac{32\mu_l U_l}{D_h^2}\left(1+0.17\frac{D_h}{L_s+\delta}\left(\frac{Re_b}{Ca_b}\right)^{0.33}\right) \tag{4.7}$$

The Warnier and Kreutzer models are both based on the pressure drop of a fully developed single phase liquid flow and the presence of the gas bubbles is accounted for in a correction term. The correction term is, for both models, dependent on the inverse of the liquid slug length. Note that the term F_b/U_l in the Warnier model can be related to the inverse of the liquid slug length using equation (4.3). The main difference between the Warnier and Kreutzer models is that the correction term of the latter does not depend on the gas bubble velocity, while its effect on the pressure drop is incorporated in the Warnier model. The reader is referred to chapter 3 for further discussion of the details of the models.

No attempt was made to adapt the models to channels with rectangular or square cross-sectional areas, other than using the appropriate hydraulic diameter D_h and replacing the constant 32 by 30.95 or 28.2 for channels with a cross-sectional area of, respectively, 100x50 μm^2 and 50x50 μm^2.

4.4 Experimental

The microfluidic structures were etched in fused silica glass chips by Deep Reactive Ion Etching and were constructed by LioniX BV. The entrance and exit holes were constructed by powder blasting. Two types of chips were constructed varying from each other in the width of the microfluidic channels, while their layout on the chip, which is shown in Figure 4.2, was the same for both types. The depth of the microfluidic structures was 50 μm for

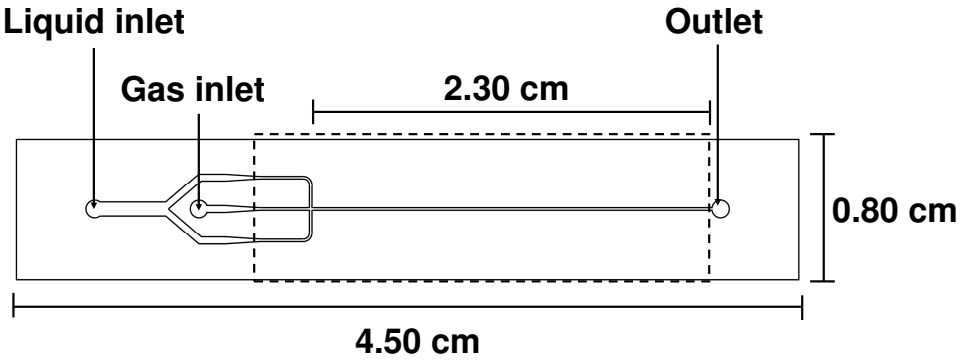

Figure 4.2: Layout of the microfluidic structures in the fused silica chips. Two types of chips were used with this layout, varying from each other in width of the channels in the section encompassed by the dashed lines. A channel width of 50 µm and 100 µm was used for the "square" and "rectangular" types, respectively. The depth of all structures was 50 µm. The length of channel downstream of the mixer, measured from the connection between channel and mixer, was 2.3 cm.

both chips. The width of the gas and liquid feed channels, the mixer and the downstream channel was 50 µm for one chip, thus resulting in channels with a square cross-sectional area. For the other chip, the width of the channels was 100 µm and the channels had a rectangular cross-sectional area.

Experiments were carried out with nitrogen and demineralized water or with nitrogen and isopropanol. The gas flow was regulated by one of the two mass flow controllers depending on the required gas flow rate (Bronkhorst F-200C/Bronkhorst F-201C). For the experiments carried out with isopropanol, the liquid flow was regulated with an Isco 100DM syringe pump, while a pressurized tank and a set of mass flow controllers (Bronkhorst L13V02/Bronkhorst L23V02) were used for the experiments with demineralized water. All experiments were performed at a temperature of 20^0 C. An overview of the range of superficial gas and liquid velocities as well as the corresponding Reynolds $Re_{gl}^0=\rho_l D_h(U_g^0+U_l)/\mu_l$, capillary $Ca_{gl}^0=\mu_l(U_g^0+U_l)/\sigma$ and Weber numbers $We_{gl}^0=\rho_l D_h(U_g^0+U_l)^2/\sigma$ are given in Table 4.1.

Images of the flows were recorded by a Redlake MotionPro CCD camera connected to a Zeiss Axiovert 200 MAT inverted microscope. The images were recorded at a resolution of 1280x48 pixels at a rate of 10,000 frames per second. An exposure time of 12 µs was sufficient to eliminate significant motion blur. The width of one pixel represented 3.6 µm of channel length. All images captured $3\cdot10^{-3}$ m of channel length. For all the

Table 4.1: Superficial gas U_g^0 and liquid U_l velocities used in this chapter. The ranges of the capillary, Reynolds and Weber numbers covered in the experiments are also given and are based on the liquid properties and the sum of the superficial gas and liquid velocities. These numbers are based on a temperature of 20 ^{0}C and a pressure of 1 bar, which is indicated by the superscript "0".

Liquid	A [μm^2]	U_g^0 [m/s]	U_l [m/s]	$U_g^0/(U_g^0+U_l)$ [-]	Ca_{gl}^0 [-]	Re_{gl}^0 [-]	We_{gl}^0 [-]
Water	50 x 50	1.7-3.0	0.3-1.2	0.61-0.88	0.03-0.05	99-176	2.7-8.7
	100 x 50	0.7-3.5	0.4-1.2	0.41-0.90	0.02-0.05	82-263	1.4-14.4
Isopropanol	100 x 50	0.8-2.5	0.1-0.6	0.70-0.93	0.09-0.28	23-76	2.0-21.3

water/nitrogen experiments, images were recorded at 6 positions in the channel at each combination of gas and liquid flow rates. For the isopropanol/nitrogen experiments, images were recorded at 5 positions in the channel at each combination of gas and liquid flow rates. The center of the channel section captured by the images recorded at the first location was positioned $1.8 \cdot 10^{-3}$ m downstream of the connection of the channel and the mixer. The center of each subsequent imaging location was positioned $3 \cdot 10^{-3}$ m further downstream of the previous location.

For each movie, every individual bubble was tracked and its length was averaged over all frames it occurred in. These values were then averaged to obtain the average bubble length L_b for that movie. The same was done for the liquid slugs, giving the average slug length L_s. The bubble frequency F_b is the number of tracked bubbles divided by the measurement time. The average velocity of a single bubble was obtained by dividing the distance traveled by its centre of mass in the movie by the time that the bubble was present in that movie. Like the average bubble and slug lengths, the velocity was first determined for every single bubble and then averaged over all bubbles to give the average bubble velocity u_b.

4.5 Results and discussion

4.5.1 Image analysis

A summary of the data obtained directly from image analysis for all experiments is given in Table 4.2.

Table 4.2: The results from image analysis are given as the minimum and maximum values found for each set of experiments. The values of the gas bubble length L_b and the liquid slug length L_s are given as a fraction of the channel width w.

Liquid	A [μm²]	L_b/w [-]	L_s/w [-]	$L_b/(L_b+L_s)$ [-]	u_b [m/s]	F_b [10^3 s^{-1}]
Water	50 x 50	1.25-5.10	0.99-6.18	0.17-0.81	0.50-1.85	2.97-6.14
	100 x 50	0.99-5.93	0.82-5.84	0.15-0.88	0.70-2.65	1.48-5.18
Isopropanol	100 x 50	1.58-13.02	0.58-2.01	0.44-0.96	0.97-2.22	1.10-7.25

The gas bubbles expand along the channel length and the bubble velocity and gas bubble length are, therefore, not constant along the channel length. The liquid, however, is incompressible and since gas bubbles can not coalesce, these should be constant over the channel length. In order to determine the variation of the hydrodynamics with time for the duration of a set of experiments, the variation of both the bubble frequency F_b and the liquid slug length L_s with position in the channel was determined. For each combination of gas and liquid velocities, channel cross-sectional area, and liquid phase, the respective coefficients of variation, *C.V.*, were determined by averaging the values of F_b and L_s over the channel length and dividing the corresponding standard deviations by these mean values. The maximum values of the respective coefficients of variation for each combination of liquid phase and channel cross-sectional area are given in Table 4.3. Although some variation of both F_b and L_s with position in the channel was observed, its magnitude is acceptable.

4.5.2 Determining A/A_b and δ

The dimensionless cross-sectional bubble area A_b/A and the correction on the liquid slug length δ are then determined from a linear fit of the liquid slug length L_s against the superficial liquid velocity divided by the bubble formation frequency U_l/F_b for each combination of channel cross-sectional area and liquid phase. The values and the 95% confidence intervals are given in Table 4.3. The value of A/A_b for the water/nitrogen Taylor flow in the square channel is equal to those found for water/nitrogen Taylor flow in rectangular channels with a cross-section of 100x50 μm^2 with varying mixer configurations. The latter results were described in chapter 2, in which it was shown that A/A_b can also be obtained from gas hold-up versus flow quality curves. The values of A/A_b determined from experiments in chapter 2 were shown to correspond to those found in literature for gas-hold up of water/nitrogen and water/air flows for a wide range of bubble velocities and channel

Table 4.3: The coefficients of variation C.V. of the bubble frequency F_b and the liquid slug length L_s for each combination of gas and liquid velocities were calculated from the values observed at the imaging locations. The maximum values are given for each combination of liquid phase and channel dimensions. The value of the inverse of the fraction of channel cross-section occupied by the gas bubble A/A_b and the values of the correction on the liquid slug length δ and their respective 95% confidence intervals are also given. The mean and standard deviation of the ratio of the superficial liquid velocity obtained from image analysis $U_{l,imaging}$ and the superficial liquid feed velocity U_l are also given for each combination of liquid and channel dimensions.

Liquid	A [μm²]	C.V. [-]		A/A_b [-]	δ [10^{-6} m]	$U_{l,imaging}$ / U_l [-]
		F_b	L_s			
Water	50 x 50	<0.07	<0.12	1.18 ± 0.03	33 ± 4	1±0.04
	100 x 50	<0.04	<0.04	1.06 ± 0.01	20 ± 4	1±0.04
Isopropanol	100 x 50	<0.08	<0.11	1.54 ± 0.02	50 ± 3	1±0.02

diameters. However, the value of A/A_b found for the water/nitrogen experiments in the rectangular channel described in this chapter is, unexpectedly, lower than the value found for the square channel, even though the gas bubble velocities, and thus the capillary numbers, were similar. The value of A/A_b for isopropanol/nitrogen is larger than those found for all the water/nitrogen experiments. This was expected, since the viscosity of isopropanol is larger than that of water and its surface tension is smaller, which results in a thicker liquid film. Thulasidas *et al.* [11] determined $u_b/(U_g+U_l)$ for gas-liquid Taylor flows in a square channel for a wide range of gas bubble velocity based capillary numbers $Ca_b=\mu_l u_b/\sigma$. From equation (4.1) it is clear that this parameter is equal to A/A_b. The values of Ca_b varied between $0.7 \cdot 10^{-2}$ and $4 \cdot 10^{-2}$ for the water/nitrogen experiments. For this range of capillary numbers, Thulasidas *et al.* found a value of A/A_b of approximately 1.2 to 1.3, which corresponds to the results obtained in the square channel and those described in chapter 2. For the isopropanol/nitrogen experiments, Ca_b varied between 0.09 and 0.2. In this range of capillary numbers, Thulasidas *et al.* found values of A/A_b of approximately 1.5 to 1.7, which is comparable to the value of 1.54 ± 0.02 found in this chapter. Furthermore, they show that the variation of A/A_b with varying Ca_b was small for $Ca_b < 0.02$, which covers most of the water/nitrogen data. The variation A/A_b is larger for $Ca_b > 0.02$, but since the range of Ca_b covered by the isopropanol/nitrogen experiments is small, variations around the mean value of A/A_b are also small. This explains finding one value of A/A_b for each set of experiments with small confidence intervals.

A similar trend is observed for the values of the correction on the liquid slug length δ. The results in chapter 2 show the value of δ to be approximately half the channel width for water/nitrogen Taylor flow in channels with 100x50μm^2 cross-sectional areas. This result is also found for the isopropanol/nitrogen Taylor flow in the channel with the same rectangular cross-sectional area. However, the value of δ found for water/nitrogen in the channel with a rectangular cross-section is lower and is approximately 0.2 times the channel width. The value of δ found for the water/nitrogen Taylor flow in the channel with a square cross-section is approximately 0.66 times the channel width, which is somewhat larger than those found in the channels with a rectangular cross-section. However, the value of δ depends on the bubble shape, and therefore also on the geometry of the channel cross-section. Finding somewhat different values of δ for experiments in channels with differerent cross-sectional area can thus be expected. Furthermore, it is important to note that δ/L_s varies from 0.03 to 0.85, indicating that 3% to 45% of the liquid having a non-zero velocity is located around the nose and tail sections of a gas bubble.

Even though an explanation for the surprisingly lower values of A/A_b and δ of water/nitrogen Taylor flow in the rectangular channel is yet to be found, the small values of the 95% confidence intervals of both parameters for all liquid and channel cross-sectional areas indicate that a linear fit was indeed warranted for all experiments. This implies that the gas bubble cross-sectional area and the amount of liquid surrounding the nose and tail sections of the gas bubbles did not significantly vary with the gas bubble velocity for the ranges of velocities used in each set of experiments.

The accuracy of this procedure can be evaluated by calculating the ratio of the superficial liquid velocity calculated from the imaging data $U_{l,imaging}$ and the actual superficial liquid feed velocity U_l. $U_{l,imaging}$ is calculated using the fitted values of A/A_b and δ, and equation (4.4). The mean of this ratio is 1 for all sets of experiments and the standard deviation is 0.04 or less. Note that the coefficient of variation of $U_{l,imaging}/U_l$ is equal or smaller than those of F_b and L_s, (Table 4.3) even though $U_{l,imaging}$ depends on the product of F_b and L_s. Thus, for a given superficial liquid feed velocity, an increase of the bubble formation frequency is accompanied by a decrease of the liquid slug size or vice versa, as is expected for a constant superficial liquid velocity. The error in estimating the superficial liquid velocity is then approximately ± 8 % of the actual value.

4.5.3 Pressure drop

For each combination of gas and liquid velocities, liquid phase and channel cross-sectional area, the pressure at each imaging location $P_{imaging}$ was calculated with equation (4.5) and the corresponding values of A/A_b and δ, as given in Table 4.3. The pressure drop was then obtained from a linear fit of the pressure as a function of location in the channel. A typical example of the obtained pressure profiles over the channel length and the corresponding linear fit is given in Figure 4.3.

In order to check the validity of a linear fit, for every combination of gas and liquid velocities, channel cross-sectional area and liquid phase, the value of $P_{imaging}$ at a given location is compared to the value P_{fit} calculated from a linear fit through those values. The results are given in Figure 4.4 in the form of a parity plot and show that assuming a linear pressure profile over the considered channel length is valid. Furthermore, it shows that the variations in bubble formation frequency andliquid slug length with location in the channel, as shown in Table 4.3, cause a difference between $P_{imaging}$ and P_{fit} of less than ±10% for 219 of the 223 data points.

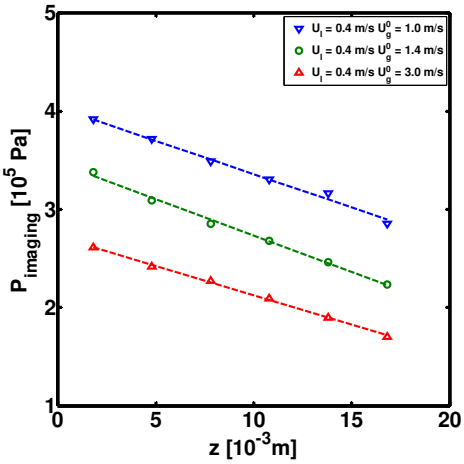

Figure 4.3: A typical example of the pressure profiles obtained from image analysis and the Taylor flow mass balance, where z is the location of the centre of the images in the channel downstream of the mixer. The dashed lines indicate the linear fit through the data points for each combination of gas and liquid velocities. These data were obtained in the channel with a 100x50 μm² cross-sectional area using water and nitrogen.

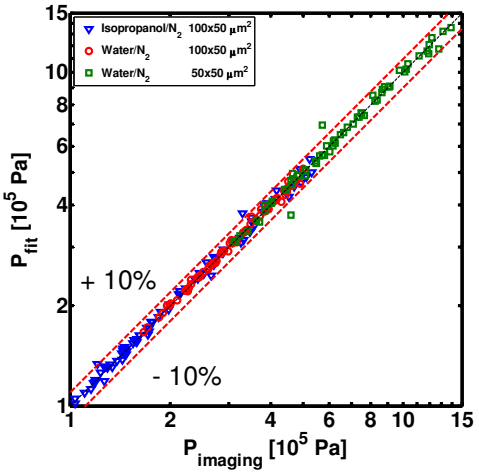

Figure 4.4: For every combination of gas and liquid velocities, channel cross-sectional area and liquid phase, the values of the pressure at each imaging location obtained from image analysis and the Taylor flow mass balance $P_{imaging}$ are compared to the values P_{fit} obtained from a linear fit through those values.

The values for the pressure drop determined in this way, are now compared to the three models discussed in section 4.2: the LMC model, the Kreutzer model and the Warnier model. For a given combination of gas and liquid velocities, liquid phase and channel cross-sectional area, the pressure drop at each imaging location was calculated with the models and averaged over all imaging locations. This value is then compared to the pressure drop determined from image analysis and the Taylor flow mass balance $-(dP/dz)_{imaging}$. For each model, these data are then plotted in a parity plot. The results are given in Figure 4.5.

The Warnier and Kreutzer models describe the results obtained for isopropanol/nitrogen and water/nitrogen Taylor flow in the 100x50 µm^2 channels within ±50% of the measured values. None of the models are capable of describing the experimental results for the water/nitrogen Taylor flow in the channel with a cross-sectional area of 50x50 µm^2 with a similar degree of accuracy. Furthermore, the LMC model is the least accurate for all the experimental results. The accuracy of the Warnier and Kreutzer models is comparable, although the details vary for the various combinations of liquid and channel cross-sectional area.

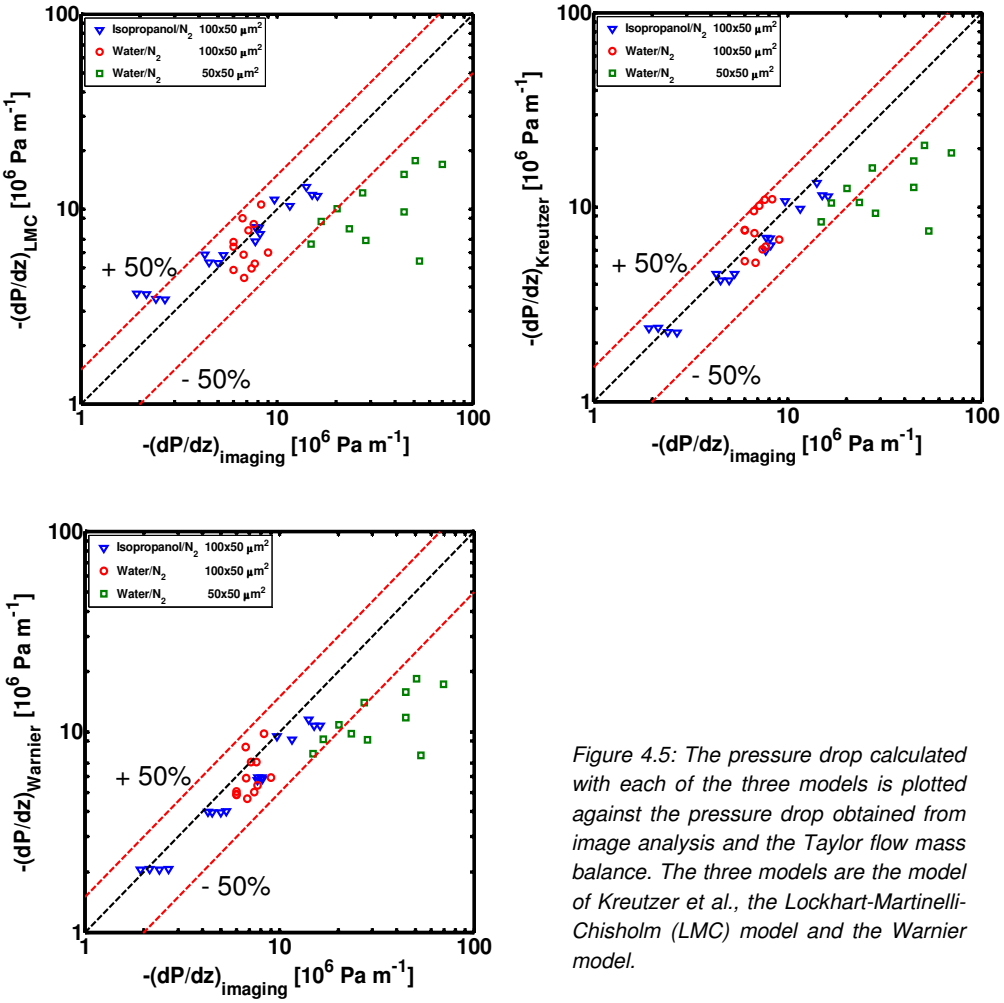

Figure 4.5: The pressure drop calculated with each of the three models is plotted against the pressure drop obtained from image analysis and the Taylor flow mass balance. The three models are the model of Kreutzer et al., the Lockhart-Martinelli-Chisholm (LMC) model and the Warnier model.

Although neither of the models is expected to precisely describe the pressure drop of gas-liquid Taylor flows in channels with a non-circular cross-sectional area, it is expected that, especially, the Kreutzer model and the Warnier model predict the pressure drop with some degree of accuracy, as it is largely determined by the liquid slug length and the liquid superficial feed velocity, which are known and incorporated in both models. The experimental data obtained with the new method for the channels with a cross-sectional area of 100x50 µm^2 are within ± 50% of the values predicted by both models. This indicates that realistic values for the pressure drop are obtained with this method. The experimental

data for the water/nitrogen Taylor flow in the channel with a cross-sectional area of 50x50 μm^2 are not accurately described by any of the three models. This can be due to an increase of inaccuracy of either the models, due the method used in this work, or due to experimental error. There is no apparent reason why the accuracy of the method would depend on the cross-sectional area of the channel. It was also determined that variations of the bubble formation frequency and liquid slug length between measurement locations for a given combination of gas and liquid velocities, liquid phase and channel cross-sectional area do not cause such large, systematic errors. Whether the models are less accurate for the channel with a square cross-sectional area or whether an experimental error is the cause of these results is not known.

4.6 Conclusions

In this chapter, a method is developed for determining the pressure drop of gas-liquid Taylor flows in micro-channels by combining data obtained from analysis of images of the Taylor flows with a mass balance based Taylor flow model. This method can be used for determining the pressure drop in micro-fluidic chips with channels of an arbitrary cross-section, where directly measuring the pressure or pressure drop is not always feasible, while imaging facilities often are available.

The data required from image analysis are: the liquid slug length, the gas bubble length and the bubble formation frequency. These data must be available for a single location for various liquid velocities, while the gas feed velocity may, but does not need to, vary. The local superficial gas velocities can then be determined from the mass balance based Taylor flow model, provided that the cross-sectional area of the gas bubbles does not vary greatly with the range of gas bubble velocities. For each combination of superficial gas and liquid feed flow rates, the pressure at that measurement location is then easily determined from the known gas feed flow rate, the local superficial gas velocity, and the ideal gas law. A pressure profile over the channel length can then be determined by applying this procedure at several locations in the channel for the same combinations of gas and liquid feed flow rates.

The method was applied to water/nitrogen Taylor flow in channels with square and rectangular cross-sectional areas of 50x50 μm^2 and 100x50 μm^2, respectively, and to

isopropanol/nitrogen Taylor flow in a channel with a cross-sectional area of 100x50 μm^2. The observed pressure profile for each combination of gas and liquid velocities, liquid phase, and cross-sectional area of the channel were linear over a distance of 1.8 mm.

The experimental data were compared to predictions from the model of Kreutzer *et al.* [1] the Lockhart-Martinelli-Chisholm model [2,3] and the model developed in chapter 3, since literature data with sufficient information or detailed pressure drop models for non-circular channels are not available. The Lockhart-Martinelli-Chisholm model was shown to least accurately describe the experimental data, as expected (see chapter 3 for a more detailed discussion). None of the models were capable of describing the data obtained for water/nitrogen Taylor flow in the channel with a rectangular cross-sectional area of 50x50 μm^2. The cause is not clear, but may be an experimental error or a decreased accuracy of the model predictions for the channel with a square cross-sectional area. However, from comparison of the water/nitrogen and isopropanol/nitrogen Taylor flow data in the, rectangular channels, it can be concluded that the method developed in this chapter yields realistic values for the pressure drop of gas-liquid Taylor flow in micro-channels with non-circular cross-sectional areas. Since no a priori knowledge of the gas bubble geometry is required, the method may be applied to channels of arbitrary cross-sectional area, as long as the liquid film surrounding the gas bubbles is static. However, a more firm validation of the method by comparison with data obtained with another measurement technique still needs to be done.

Nomenclature

A	area of the channel cross-section [m^2]
A_b	area of the bubble cross-section [m^2]
Ca_b	capillary number based on the properties of the liquid and the gas bubble velocity [-]
D_h	hydraulic diameter: 4 x the channel cross-sectional area divided by the wetted perimeter [m]
F_b	frequency of bubbles [s^{-1}]
L_b	length of a gas bubble [m]
L_{nose}	length of the nose of a gas bubble [m]
L_s	length of a liquid slug [m]
L_{tail}	length of the tail of a gas bubble [m]
P^0	reference pressure, 10^5 [Pa]
P_{fit}	pressure at a location in the channel obtained from a linear fit of the pressure profile [Pa]
$P_{imaging}$	pressure at a location in the channel obtained from image analysis and the Taylor flow mass balance [Pa]
Re_b	Reynolds number based on the properties of the liquid and the gas bubble velocity [-]
Re_{gl}	Reynolds number based on the properties of the liquid and the sum of the superficial gas and liquid velocities [-]
u_b	velocity of a gas bubble [m/s]
U_g	superficial gas velocity [m/s]
U_g^0	superficial gas feed velocity at the reference pressure P^0 and a temperature of 20 ^{0}C [m/s]
U_l	superficial liquid velocity [m/s]

$U_{l,imaging}$	superficial liquid velocity obtained from image analysis and the Taylor flow mass balance [m/s]
w	width of the channel [m]
We_b	Weber number based on the properties of the liquid and the gas bubble velocity [-]
We_{gl}	Weber number based on the properties of the liquid and the superficial gas and liquid velocities [-]
z	axial position in the channel [m]

Greek symbols

δ	correction on slug length for the liquid in the slug surrounding the nose and tail of bubble [m]
μ_l	viscosity of the liquid [Pa·s]
ρ_l	density of the liquid phase [kg/m^3]
σ	surface tension [N/m]

Subscripts

b	gas bubble
s	liquid slug

Abbreviations

Kreutzer model	The model of Kreutzer *et al.* [1]
LMC model	The model of Lockhart-Martinelli and Chisholm [2,3]
Warnier model	The model developed in chapter 3.

References

[1] Kreutzer, M. T., Kapteijn, F., Moulijn, J. A., Kleijn, C. R., Heiszwolf, J. J., Inertial and interfacial effects on pressure drop of Taylor flow in capillaries. *AIChE Journal*, 51(9), 2428-2440, 2005

[2] Lockhart, R. W., Martinelli, R. C., Proposed correlation of data for isothermal two-phase, two-component flow in pipes. *Chem. Eng. Prog.*, 45(1), 39-48, 1949

[3] Chisholm, D., A theoretical basis for the Lockhart-Martinelli correlation for two-phase flow. *Int. J. Heat Mass Transf.*, 10(12), 1767-1778, 1967

[4] Günther, A., Jensen, K. F., Multiphase microfluidics: From flow characteristics to chemical and materials synthesis. *Lab Chip Miniaturisation Chem. Biol.*, 6(12), 1487-1503, 2006

[5] Abkarian, M., Faivre, M., Stone, H. A., High-speed microfluidic differential manometer for cellular-scale hydrodynamics. *Proc. Natl. Acad. Sci. U. S. A.*, 103(3), 538-542, 2006

[6] Kohl, M. J., Abdel-Khalik, S. I., Jeter, S. M., Sadowski, D. L., An experimental investigation of microchannel flow with internal pressure measurements. *Int. J. Heat Mass Transf.*, 48(8), 1518-1533, 2005

[7] Fuerstman, M. J., Lai, A., Thurlow, M. E., Shevkoplyas, S. S., Stone, H. A., Whitesides, G. M., The pressure drop along rectangular microchannels containing bubbles. *Lab Chip Miniaturisation Chem. Biol.*, 7(11), 1479-1489, 2007

[8] Srivastava, N., Burns, M. A., Microfluidic pressure sensing using trapped air compression. *Lab Chip Miniaturisation Chem. Biol.*, 7(5), 633-637, 2007

[9] Kolb, W. B., Cerro, R. L., Coating the inside of a capillary of square cross section. *Chem. Eng. Sci.*, 46(9), 2181-2195, 1991

[10] Hazel, A. L., Heil, M., The steady propagation of a semi-infinite bubble into a tube of elliptical or rectangular cross-section. *J. Fluid. Mech.*, 470, 91-114, 2002

[11] Thulasidas, T. C., Abraham, M. A., Cerro, R. L., Bubble-train flow in capillaries of circular and square cross section. *Chem. Eng. Sci.*, 50(2), 183-199, 1995

[12] Fries, D. M., Trachsel, F., von Rohr, P. R., Segmented gas-liquid flow characterization in rectangular microchannels. *Int. J. Multiphase Flow*, 34(12), 1108-1118, 2008

[13] Kreutzer, M. T., Kapteijn, F., Moulijn, J. A., Heiszwolf, J. J., Multiphase monolith reactors: Chemical reaction engineering of segmented flow in microchannels. *Chem. Eng. Sci.*, 60(22), 5895-5916, 2005

Chapter 5

Gas-liquid flow regimes and Taylor gas bubble and liquid slug lengths for various channel cross-sectional areas and mixer designs

Parts of this chapter are excerpts from:

Haverkamp, V., Hessel, V., Löwe, H., Menges, G., Warnier, M.J.F., Rebrov, E.V., De Croon, M.H.J.M., Schouten, J.C., Liauw, M.A., Hydrodynamics and mixer-induced bubble formation in micro bubble columns with single and multiple channels. *Chem. Eng. Technol.*, 29(9), 1015-1026, 2006

Abstract

The work presented in this chapter concerns controlling the gas bubble and liquid slug lengths in gas-liquid Taylor flow. First, the influence of mixer design, liquid phase and channel dimensions on the flow maps in microchannels is studied. Furthermore, the bubble length as a function of mixer design, liquid phase, and superficial gas and liquid velocities is investigated.

Experimental results showed that the ratio of the gas bubble length and the width of the channel depends linearly on the ratio of the gas and liquid flow rates in the mixer. This result also implies that, for a given mixer and channel, the gas bubble and liquid slug lengths can not be varied independently from each other. However, if the geometry of the mixer can be varied independently from the dimensions of the downstream channel, then the gas bubble length, liquid slug length and total flow rate can be chosen independently from each other.

5.1 Introduction

Monoliths and microreactors for gas-liquid and gas-liquid-solid reactions are generally operated in the gas-liquid Taylor flow regime [1,2,3], which consists of sequences of a gas bubble and a liquid slug. The length of the gas bubbles is larger than the channel diameter and a thin liquid film separates the gas bubbles from the channel walls. For horizontal and vertical channels in which gravitational forces are negligible, the liquid film is stagnant. This liquid film ensures a short diffusion path length for the gas phase diffusing through the film to the channel wall, where the catalyst is often located. Furthermore, for liquids and bubble velocities typically applied in gas-liquid-solid reactions, most of the liquid in the slugs forms recirculation cells, which move at the same velocity as the gas bubbles. The thin liquid film and the liquid circulation cells make Taylor flow a suitable flow regime for three-phase reactions where mass transfer to the wall is of influence on the reaction rate.

The key hydrodynamic parameters in gas-liquid Taylor flow are: the gas bubble length, the liquid slug length, the gas bubble velocity and the liquid film thickness. For proper design of reactors operating under Taylor flow conditions, it is required to understand how mass transfer rates, heat transfer rates and pressure drop depend on these parameters. As the understanding of pressure drop and gas-liquid-solid mass transfer as a function of the various hydrodynamic properties of gas-liquid Taylor flow is growing [1,2], it is also important to be able to control these hydrodynamics by manipulating parameters that can be directly influenced, *e.g.* the gas and liquid feed velocities, the geometry of the gas-liquid contactor and the geometry of the channel.

5.1.1 Taylor flow and flow pattern maps

The first subject of interest is for which combination of superficial gas and liquid velocities Taylor flow occurs, as several other flow patterns are also found in small channels. An overview of the various flow patterns is given in Figure 5.1. In bubbly flow, the gas bubbles are smaller than the channel diameter. Taylor flow is defined as the flow regime in which the gas bubble length is larger than the channel diameter. In annular flow, the gas is surrounded by continuous liquid film along the whole length of channel. Ring flow is similar to annular flow, except that waves are now formed in the liquid film moving downstream. Churn flow is similar to ring flow, but the gas core is occasionally disrupted and small gas bubbles are

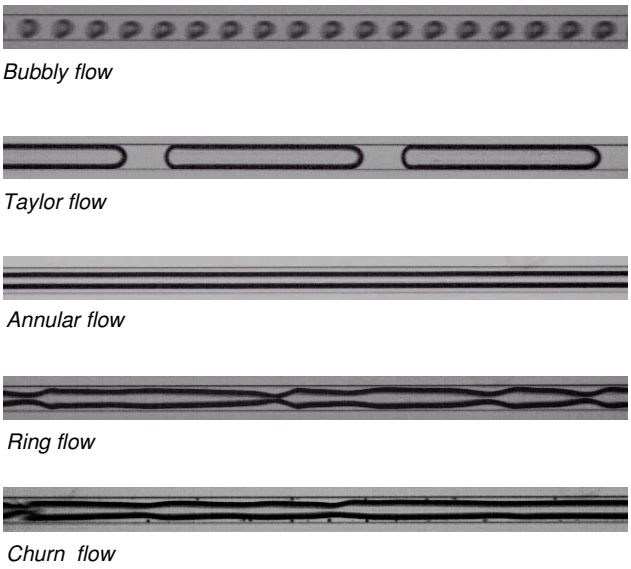

Figure 5.1: Various flow patterns observed in this work. The image of bubbly flow was recorded for a nitrogen-isopropanol flow in a glass channel with a cross-sectional area of 100x50 μm^2. The other images were recorded for nitrogen-water flows in glass channels with a cross-sectional area of 100x50 μm^2.

present in the liquid film. Furthermore, in churn flow the shape of a given liquid wave is less uniform along the channel perimeter.

Note that, in this context, small channels are defined as channels in which surface tension forces dominate gravitational forces [1]. This type of information is typically presented in a flow pattern map, of which numerous are available in literature. Generally nitrogen or air is used in combination with water, although some authors have also presented flow maps for other liquids. Flow maps in small channels are available for channel diameters in the order of 10^{-5} to 10^{-3} m, and for various channel and gas-liquid geometries. An excellent overview and discussion of the available flow maps and the varied parameters is given in a recent review publication by Shao and Gavriilidis [4]. They also conclude that the various flow maps show the greatest amount of overlap when the superficial gas and liquid velocities are used as coordinates.

5.1.2 Gas bubble and liquid slug lengths

Apart from knowing at which combinations of gas and liquid velocities gas-liquid Taylor flow can be achieved, it is also important to know how to control the gas bubble length. Note that,

for a gas-liquid Taylor flow with a stagnant liquid film surrounding the gas bubble, the following equation can be derived from the mass balance based model discussed in chapters 2, 3 and 4:

$$\frac{U_g}{U_l} = \frac{L_b - \delta}{L_s + \delta} \tag{5.1}$$

where L_b is the gas bubble length, L_s is the length of a liquid slug, U_g is the superficial gas velocity, U_l is the superficial liquid velocity, and δ is a correction on the liquid slug and gas bubble length in order to account for the liquid surrounding the nose and tail sections of a gas bubble. The reader is referred to chapter 2 for more details.

Equation (5.1) shows that, assuming the superficial gas and liquid velocities, U_g and U_l are known, controlling the gas bubble length L_b implies also controlling the liquid slug length L_s.

Two main mechanisms for gas bubble formation in small channels are known in literature. The first mechanism is break-up of a gas jet surrounded by a co-flowing liquid, which is initiated by instabilities at the shear layer at the liquid–gas interface and surface tension [5]. These then grow and eventually lead to a break-up of the gas jet to form a gas bubble. The frequency at which this happens is fixed for a given set of gas and liquid flow rates, which leads to monodisperse gas bubbles, but was not quantified.

The second mechanism is the so-called “squeezing” mechanism observed in T-mixers and cross-mixers [6,7,8]. For T- and cross-mixers, the liquid compresses the gas phase, respectively, against the channel wall or between two liquid streams until a gas bubble is formed. For gas and liquid feed channels of which the height and width are equal to those of the downstream channel, the following equation is found to describe the data:

$$\frac{L_b}{w} = a\frac{U_g}{U_l} + b \tag{5.2}$$

This equation is based on continuity and the assumptions that 1) necking of the gas phase starts when the gas bubble has nearly filled the complete cross-sectional area of the channel, and 2) necking occurs by the liquid filling the mixer without any resistance from the

gas. Cubaud *et al.* [6] investigated bubble formation in a cross-mixer for gas bubble velocities varying from 0.15 to 3 m/s and report the values of *a* and *b* to be approximately 1. Garstecki *et al.* [7] used a T-mixer and also found a value of 1 for both parameters for both gas-liquid and liquid-liquid systems. Van Steijn *et al.* [8] take into account that the gas bubble will never completely fill the cross-sectional area, resulting in liquid bypassing the gas bubble, even when its formation is nearly complete. They found the values of both *a* and *b* to be approximately 1.5 for a T-mixer.

5.2 Experimental

The data described in this chapter have been obtained doing the experiments described in chapters 2 and 4. The reader is referred to those chapters for details of the used set-ups and applied imaging techniques. Only the necessary information required for interpreting the data in this chapter are included in this section.

Flow maps were constructed for five different combinations of microfluidic chip and gas and liquid phases. The microfluidic chips used in chapter 2 are, henceforth, referred to as the “cross” and “smooth” mixer and their respective designs are shown in Figure 5.2. Nitrogen-water flows were applied in these chips. The layout of the microfluidic chips used in chapter 3 is shown in Figure 5.3. Nitrogen-water flows were used in the chips with the rectangular and square cross-sectional areas, while isopropanol-water flows were only used in the channels with a rectangular cross-sectional area. All flow maps were measured at the end of each channel, approximately 3 mm upstream of its exit.

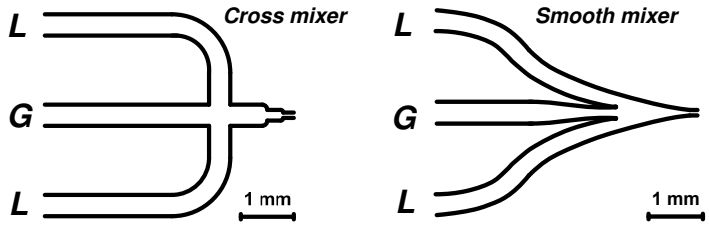

Figure 5.2: Geometries of the two mixers used for realizing two-phase flow in a downstream channel with a rectangular cross-section of 100 x 50 μm² and a length of 2 cm. The depth of these structures is 50 μm. The bar represents 1 mm.

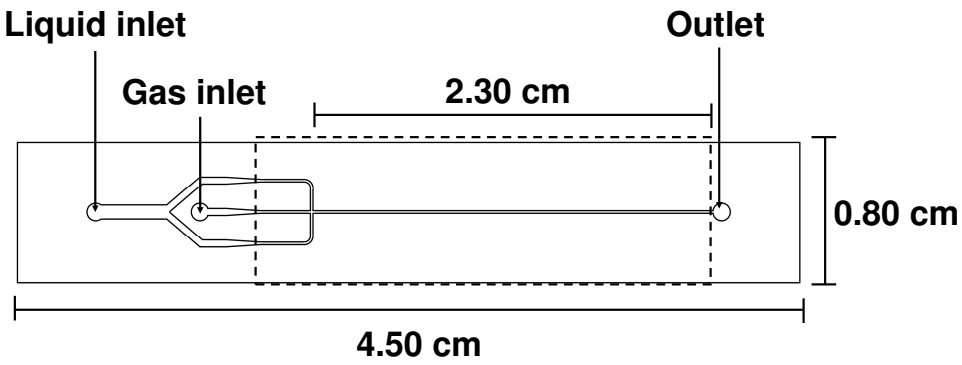

Figure 5.3: Layout of the microfluidic structures in the fused silica chips. Two types of chips were used with this layout, varying from each other in width of the channels in the section encompassed by the dashed lines. Channels with a with of 50 µm and 100 µm were used. The depth of all structures was 50 µm. The length of channel downstream of the mixer, measured from the connection between channel and mixer, was 2.3 cm.

When studying the gas bubble length as a function of superficial gas and liquid velocities, mixer, and channel geometry, the gas bubble length and superficial gas velocity have to be evaluated at the pressure in the mixer. However, for all of these experiments, the pressure in the mixer is not known. In the experiments described in chapter 4, the gas bubble length was measured close to the mixer and the local superficial gas velocity was also determined by the method developed in chapter 4. These data are, therefore, used in this chapter. An overview of the experimental conditions for these experiments is given in Table 5.1.

The data were recorded at a distance of 1.3 mm downstream of the mixer. The local superficial gas velocity $U_{g,imaging}$ was determined by combining data from image analysis with a mass balance based Taylor flow model. Equation (5.3) is used to calculate $U_{g,imaging}$.

Table 5.1: Overview of the mixer designs, channel dimensions and superficial gas U_g^0 and liquid U_l velocities used for studying the gas bubble length as a function of superficial velocities, mixer and channel geometry. The superficial gas velocity is given at a temperature of 20 ^{0}C and a pressure of 1 bar, which is indicated by the superscript "0".

Liquid	A	U_g^0	U_l	$U_g^0/(U_g^0+U_l)$	Ca_{gl}^0	Re_{gl}^0	We_{gl}^0
	[µm^2]	[m/s]	[m/s]	[-]	[-]	[-]	[-]
Water	50 x 50	1.7-3.0	0.3-1.2	0.61-0.88	0.03-0.05	99-176	2.7-8.7
	100 x 50	0.7-3.5	0.4-1.2	0.41-0.90	0.02-0.05	82-263	1.4-14.4
Isopropanol	100 x 50	0.8-2.5	0.1-0.6	0.70-0.93	0.09-0.28	23-76	2.0-21.3

$$U_{g,imaging} = \frac{A_b}{A} F_b \left(L_b - \delta \right) \tag{5.3}$$

The bubble frequency F_b and the bubble length L_b are directly obtained from analysis of the images. The parameters A_b/A and δ are, respectively, the fraction of cross-sectional area of the channel occupied by the gas bubble and a correction on the gas bubble length to account for the amount of liquid surrounding the nose and tail sections of a gas bubble. The parameters can be obtained from images of the Taylor flow and the mass balance model. The reader is referred to chapter 4 for further details.

5.3 Results and discussion

5.3.1 Flow maps

The flow maps measured for the various combinations of gas and liquid phases, the type of mixer, and the dimensions of the cross-sectional area of the channel are given in Figure 5.4.

A range of gas and liquid superficial velocities was found for which the flow regime periodically switches between Taylor flow and ring flow was found for all chips and liquids. This combination of regimes will henceforth be referred to as the Taylor-ring regime. The velocity with which a given liquid ring or gas bubble moves through the channel is not constant. For only a few combinations of gas and liquid velocities, the flow regime switched between Taylor flow and annular flow: the Taylor-annular regime. It was observed for water and nitrogen in the chips with the smooth and cross-mixers and for isopropanol and nitrogen in the chip with the 100x100x50 μm^3 mixer.

Direct comparison of the flow maps is complicated by the fact that the local superficial gas velocity varies with location in the channel, due to the large pressure drop relative to the average pressure in the channel. No pressure transducer was available in the set-ups and the local superficial gas velocity is not known. However, the gas mass flow rate is known and is expressed as the superficial gas velocity at reference conditions (U_g^0 at a temperature of 20 ^{0}C and a pressure of 1 bar) and this velocity is used as a coordinate in the flow maps.

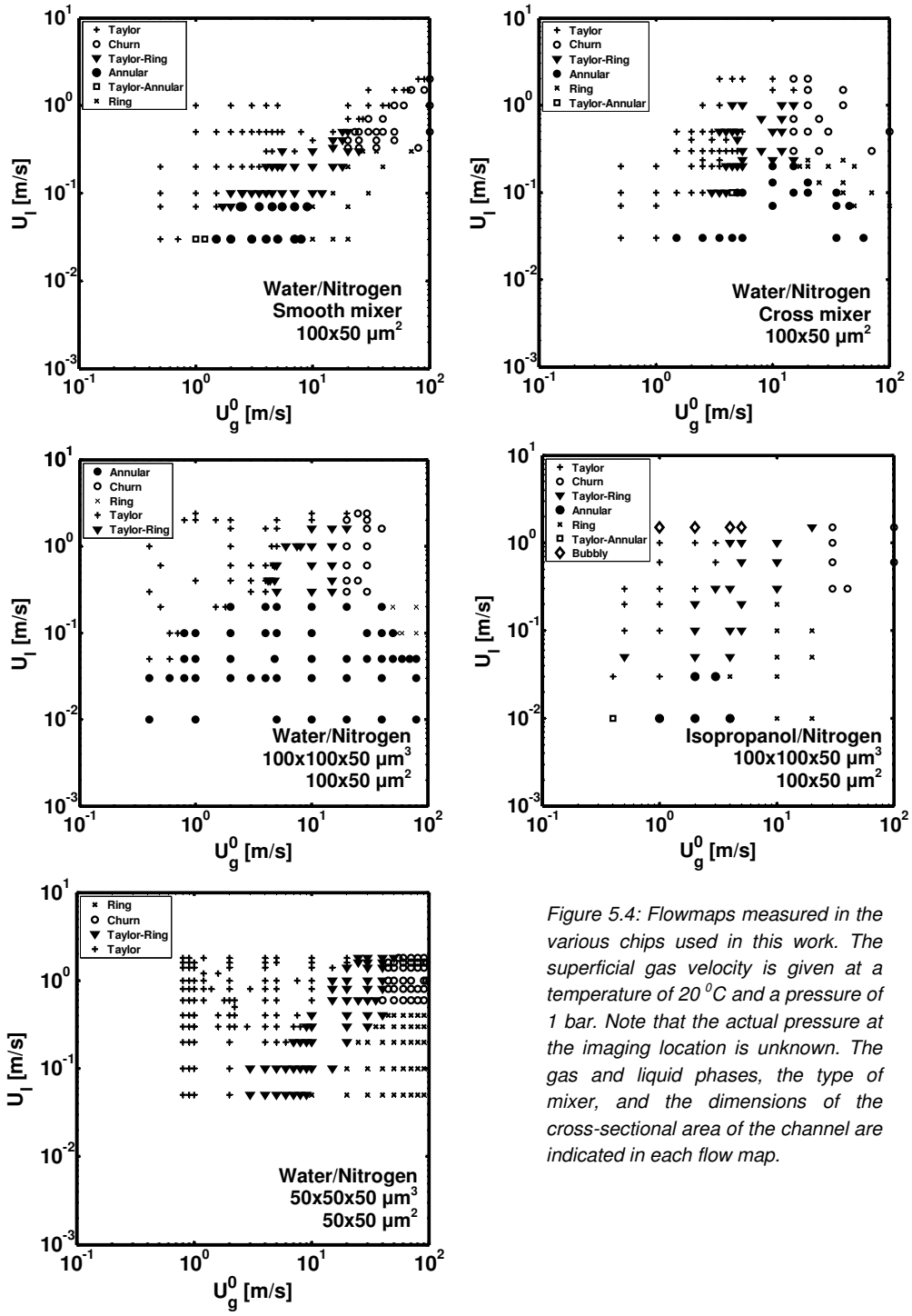

Figure 5.4: Flowmaps measured in the various chips used in this work. The superficial gas velocity is given at a temperature of 20 ^{0}C and a pressure of 1 bar. Note that the actual pressure at the imaging location is unknown. The gas and liquid phases, the type of mixer, and the dimensions of the cross-sectional area of the channel are indicated in each flow map.

The influence of the mixer design on the flow pattern map can be examined by comparing the flow maps obtained for nitrogen-water in three chips with different mixer designs, each followed by a channel with a rectangular cross-sectional area of 100x50 μm^2. The flow map for the chip with the smooth mixer differs significantly from that of the other two chips. When comparing the flow map of the smooth chip to the other two, 1) the transition from Taylor to churn flow, at a given liquid velocity, occurs at a higher superficial gas velocity, and 2), at a given liquid velocity, the transition from annular to ring flow is shifted to a lower superficial gas velocity. The transition from ring to churn flow appears to be independent of the superficial gas velocity and occurs at the same superficial liquid velocity ($U_l \approx 0.2$ m/s) for all three microfluidic chips. The transition from Taylor flow to annular flow varies little with mixer design. These results suggest that the design of the mixer geometry is mainly of influence for high superficial gas and/or liquid velocities, where inertial forces are significant.

The influence of the properties of the liquid was studied by comparing the flow maps for water-nitrogen and isopropanol-nitrogen flows obtained in the microfluidic chips with equal channel and mixer designs. Bubbly flow was observed for nitrogen-isopropanol, but not for nitrogen-water. Furthermore, when comparing the flow map of nitrogen-isopropanol to that of nitrogen-water, 1) the transition from annular to ring flow occurred at lower superficial gas velocities, and 2) the transition from annular to Taylor-ring flow occurred at lower superficial liquid velocities. Churn flow was found for the same range of superficial gas and liquid velocities, regardless of whether water or isopropanol was used. Thus, a change in properties of the liquid affects most regime transitions, except when both the superficial liquid and gas velocities are high and inertial forces are large compared to surface tension forces.

The influence of the geometry of the channel was investigated by comparing the flow maps obtained for nitrogen-water in chips with channels having a cross-sectional area of 100x50 μm^2 and 50x50 μm^2. Note that the sizes of the mixing chambers varied as indicated in Figure 5.4. Annular flow was not observed in the chip containing the channel with the smaller cross-sectional area. Upon reducing the size of the channel and mixer, the direct transition from Taylor to churn flow was no longer observed. Furthermore, for all superficial liquid velocities, Taylor flow was found up to larger superficial gas velocities for the chip with the smaller channel. For both chips, the transition from ring flow to churn flow was found to be independent of the superficial gas velocity. However, the superficial liquid velocity at which the transition occurred was different for the two chips. Since

the dimensions of both the mixer and the channel were varied, it is not possible to determine which parameter was of greater influence on the resulting flow map.

In general, the maximum superficial gas velocity for which Taylor flow can be obtained increases with increasing superficial liquid velocity. The maximum superficial gas and liquid velocities, for which Taylor flow could be obtained in all chips, were $U_g^0 \approx 2$ m/s and $U_l \approx 1$ m/s, respectively.

5.3.2 Gas bubble and liquid slug lengths

Data from the experiments discussed in chapter 4 were used in order to study the bubble length as a function of mixer design, liquid phase, and superficial gas and liquid velocities. In Figure 5.5, the gas bubble length divided by the width of the channel *w* was plotted against the ratio of the superficial gas velocity at the imaging location $U_{g,imaging}$ and the superficial liquid velocity U_l.

For all three data sets, the relation was linear, and could therefore be described by equation (5.2). The parameters *a* and *b* were fitted for each of the data sets and the

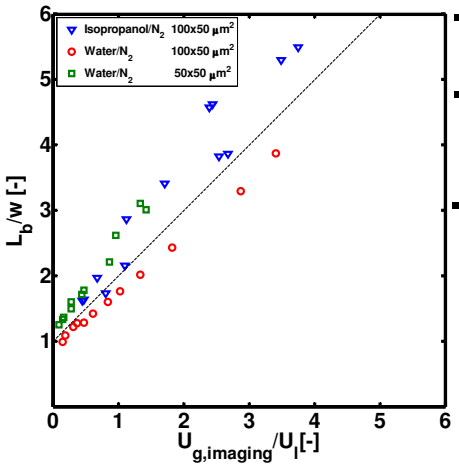

Liquid	A [µm²]	*a* [-]	*b* [-]
Water	50 x 50	1.40 ± 0.14	1.14 ± 0.01
	100 x 50	0.85 ± 0.03	0.91 ± 0.04
Isopropanol	100 x 50	1.19± 0.08	1.18 ± 0.36

Figure 5.5: Comparison of the ratio of the gas bubble length L_b and the width of the channel w to the ratio of sum of the superficial gas and liquid velocities dividied by the superficial liquid velocity. The dashed line corresponds to equation (5.2), where a and b are equal to 1. The fitted values of a and b and the respective values of the 95% confidence intervals are given in the table, for each data set.

respective values and their 95% confidence intervals, based on the fitting procedure, are also given in Figure 5.5. Although the values of *a* and *b* are different for each data set, they are in the order of 1, as found by Cubaud *et al*. for similar channel dimensions and gas and liquid velocities [6]. The exact values of *a* and *b* are expected to depend on the rate of necking and collapse of the gas, as well as of the amount of liquid leaking past the gas bubble while its being formed. The latter then also depends on the cross-sectional area of the bubble with respect to the shape of the channel cross-section before it "snaps off". Fu *et al.* [9] have shown that the collapse rate of the gas thread depends mainly on the gas and liquid velocities and, to a lesser degree, on the liquid viscosity, but not on the surface tension of the liquid. This supports the result that a simple model based on only the gas and liquid velocities and the dimensions of the channel and mixer is capable of describing the observed trends.

Further work is required in order to be able to predict the values of *a* and *b* for a given liquid and both mixer and channel dimensions. However, the linearity of the relation between the dimensionless gas bubble length and the ratio of the superficial gas and liquid velocities allows for easy extrapolation once *a* and *b* have been determined for a limited amount of experiments.

5.4 Implications of the results for controlling the gas bubble and liquid slug lengths independently

For a given mixer and channel, the ratio of superficial gas and liquid velocities not only determines the gas bubble length, but also the liquid slug length according to equation (5.1). Thus, the liquid slug length and the gas bubble length can not be controlled independently for a given mixer and channel. Note that the total superficial velocity does not affect the gas bubble and liquid slug lengths, as long as the ratio between the gas and liquid superficial velocity is constant.

Even though, for a given mixer and channel, the liquid slug length and the gas bubble length can not be controlled independently, it is possible to obtain the desired gas bubble and liquid slug lengths if these are known prior to designing the device. The width and height of the channels in the cross-mixer do not necessarily have to be equal to those in

the downstream channel. This can be used to control the gas bubble length at a given ratio of gas and liquid flow rates, as is illustrated in the following example.

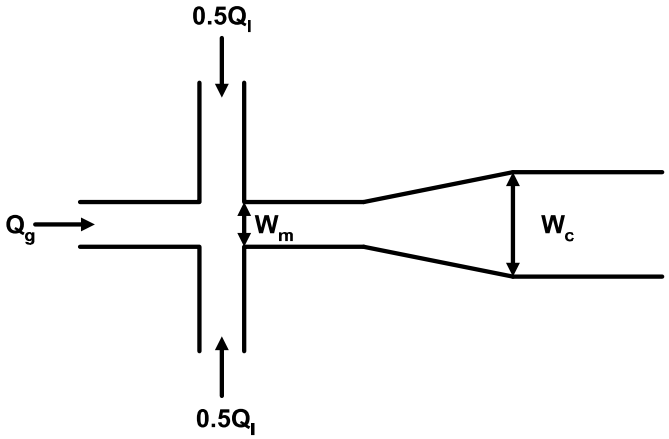

Figure 5.6: Schematic drawing of a cross-mixer in which the channels have a different width w_m than the downstream channel w_c. All channels have an equal depth h. Q_g and Q_l are, respectively, the gas and liquid feed flow rates.

Consider a microfluidic device as depicted in Figure 5.6. For the sake of simplicity, the height of all channels is equal to *h*. The channels in the mixer section all have a width w_m and the width of the main channel is w_c. The volumetric gas and liquid feed flow rates are Q_g and Q_l, respectively. In order to illustrate the principle, thickness of the the liquid film surrounding the gas bubble, the correction term on the gas and liquid slug lengths, and the gas bubble expansion due to pressure drop are not taken into account.

Since the gas bubbles do not coalesce, the volume of a gas bubble formed in the mixer is equal to that in the channel section, resulting in:

$$L_{b,m} w_m = L_{b,c} w_c \tag{5.4}$$

For a cross-mixer where all 4 channels have the same width and height, the bubble length in the mixer depends on the gas and liquid flow rates, similar to equation (5.2):

$$\frac{L_{b,m}}{w_m} = a\frac{Q_g}{Q_l} + b \tag{5.5}$$

The length of the gas bubble in the channel is then:

$$L_{b,c} = \left(a\frac{Q_g}{Q_l} + b \right)\frac{w_m^2}{w_c} \tag{5.6}$$

Furthermore, the ratio of gas and liquid flow rates is equal to the ratio of gas bubble and liquid slug lengths:

$$\frac{L_{b,c}}{L_{s,c}} = \frac{Q_g}{Q_l} \tag{5.7}$$

This example shows that:

- the ratio between gas bubble and liquid slugs lengths can be controlled by the ratio of gas and liquid flow rates,
- at this ratio of gas and liquid flow rates, the gas bubble length can be set by choosing the appropriate dimensions of the cross-mixer,
- the total flow rate, and thus the gas bubble velocity, can be varied without affecting the lengths of the gas bubbles and liquid slugs, provided that the ratio between gas and liquid flow rates is constant.

5.5 Conclusions

The work presented in this chapter concerns controlling the gas bubble and liquid slug lengths in gas-liquid Taylor flow. First, the influence of mixer design, liquid phase and

channel dimensions on the flow maps in microchannels was studied. The results show that that the design of the mixer geometry is mainly of influence for high superficial gas and/or liquid velocities, where inertial forces are significant. Varying the liquid phase between water and isopropanol affected most regime transitions, except when both the superficial liquid and gas velocities were high and inertial forces were large compared to surface tension forces. When decreasing the dimensions of the cross-sectional area of the channel and mixer from 100x50 μm^2 to 50x50 μm^2, annular flow was no longer observed and, at equal liquid velocities, Taylor flow was observed at higher gas velocities.

In general, the maximum superficial gas velocity for which Taylor flow could be obtained increased with increasing superficial liquid velocity. The maximum superficial gas and liquid velocities for which Taylor flow could be observed varied in the various experiments. However, Taylor flow was always observed when the superficial gas and liquid velocities were smaller than $U_g^0 \approx 2$ m/s and $U_l \approx 1$ m/s, respectively.

Experimental results showed that the ratio of the gas bubble length and the width of the channel depends linearly on the ratio of the gas and liquid flow rates in the mixer. This result was also found by other authors for cross-mixers [6] and T-mixers [7,8], where the gas and liquid feed channels had the same width and height as the downstream channel. These results also imply that the gas bubble and liquid slug lengths can not be varied independently for a given mixer and channel.

However, if the geometry of the mixer can be varied independently from the dimensions of the downstream channel, then the gas bubble length, liquid slug length and total flow rate can be chosen independently from each other. A simple example for a cross-mixer showed that:

- the ratio between gas bubble and liquid slugs lengths can be controlled by the ratio of gas and liquid flow rates,
- at this ratio of gas and liquid flow rates, the gas bubble length can be set by choosing the appropriate dimensions of the cross-mixer,
- the total flow rate, and thus the gas bubble velocity, can be varied without affecting the lengths of the gas bubbles and liquid slugs, provided that the ratio between the gas and liquid flow rates is constant.

Nomenclature

a fit parameter [-]

A area of the channel cross-section [m^2]

A_b area of the gas bubble cross-section [m^2]

b fit parameter [-]

Ca_{gl}^{0} capillary number based on the properties of the liquid and the sum of the superficial gas and liquid velocities at at a temperature of 20^0C and a pressure of 1 bar [-]

F_b bubble formation frequency [s^{-1}]

h height of a channel [m]

L_b length of a gas bubble [m]

L_s length of a liquid slug [m]

Re_{gl}^{0} Reynolds number based on the properties of the liquid and the sum of the superficial gas and liquid velocities at at a temperature of 20^0C and a pressure of 1 bar [-]

U_g local superficial gas velocity [m/s]

U_g^{0} superficial gas velocity at a temperature of 20^0C and a pressure of 1 bar [m/s]

U_l superficial liquid velocity [m/s]

w width of a channel [m]

We_{gl}^{0} Weber number based on the properties of the liquid and the sum of the superficial gas and liquid velocities at at a temperature of 20^0C and a pressure of 1 bar [-]

Greek symbols

δ correction on slug length for the liquid in the slug surrounding the nose and tail of a gas bubble [m]

subscripts

b gas bubble

c channel

f liquid film

g gas

imaging based on data obtained from image analysis

l liquid

m mixer

s liquid slug

References

[1] Angeli, P., Gavriilidis, A., Hydrodynamics of Taylor flow in small channels: A review. *Proc. Inst. Mech. Eng. Part C J. Mech. Eng. Sci.*, 222(5), 737-751, 2008

[2] Kreutzer, M. T., Kapteijn, F., Moulijn, J. A., Heiszwolf, J. J., Multiphase monolith reactors: Chemical reaction engineering of segmented flow in microchannels. *Chem. Eng. Sci.*, 60(22), 5895-5916, 2005

[3] Günther, A., Khan, S. A., Thalmann, M., Trachsel, F., Jensen, K. F., Transport and reaction in microscale segmented gas-liquid flow. *Lab Chip Miniaturisation Chem. Biol.*, 4(4), 278-286, 2004

[4] Shao, N., Gavriilidis, A., Angeli, P., Flow regimes for adiabatic gas-liquid flow in microchannels. *Chem. Eng. Sci.*, 64(11), 2749-2761, 2009

[5] Gordillo, J. M., Gañán-Calvo, A. M., Pérez-Saborid, M., Monodisperse microbubbling: Absolute instabilities in coflowing gas-liquid jets. *Phys. Fluids*, 13(12), 3839-3842, 2001

[6] Cubaud, T., Tatineni, M., Zhong, X., Ho, C. M., Bubble dispenser in microfluidic devices. *Physical Review E - Statistical, Nonlinear, and Soft Matter Physics*, 72(3), 1-4, 2005

[7] Garstecki, P., Fuerstman, M. J., Whitesides, G. M., Stone, H. A., Formation of droplets and bubbles in a microfluidic T-junction - Scaling and mechanism of break-up. *Lab Chip Miniaturisation Chem. Biol.*, 6(3), 437-446, 2006

[8] Van Steijn, V., Kreutzer, M. T., Kleijn, C. R., μ-PIV study of the formation of segmented flow in microfluidic T-junctions. *Chem. Eng. Sci.*, 62(24), 7505-7514, 2007

[9] Fu, T., Ma, Y., Funfschilling, D., Li, H. Z., Bubble formation and breakup mechanism in a microfluidic flow-focusing device. *Chem. Eng. Sci.*, 64(10), 2392-2400, 2009

Chapter 6

Partial hydrogenation of phenylacetylene in a micro capillary: experimental results and dimensioning of the catalyst layer thickness and capillary diameter

Abstract

The hydrogenation of phenylacetylene in isopropanol was performed over Pd supported on mesoporous titania films with a thickness of $120 \cdot 10^{-9}$ $m_{coating}$ coated on the walls of a glass capillary with an inner diameter of $2.5 \cdot 10^{-4}$ m_c. The reaction was performed in the Taylor flow and Taylor-ring-annular regimes at temperatures varying from 313 to 343 K. The phenylacetylene conversions were smaller than 0.2 and styrene selectivities were higher than 0.92. The pressure in the reactive capillaries was estimated from model calculations. Calculations based on the data for the Taylor flow regime show that the maximum thickness of the coating layer is $4 \cdot 10^{-6}$ $m_{coating}$ in order to avoid internal mass transfer limitations. At this maximum thickness of the coating layer, a channel diameter smaller than $1.47 \cdot 10^{-3}$ m_c is required in order to also avoid external mass transfer limitations. At these limiting values, the overall reaction rate coefficient has a value of 0.10 $m_l^3 m_c^{-3} s^{-1}$ and the amount of catalyst per volume unit of capillary is then 16.9 $kg_{coating}/m_c^3$. Furthermore, a scaling analysis showed that the ratio of the volumetric reaction rate of the catalyst and the volumetric mass transfer coefficient scales linearly with the channel diameter, for Taylor flow with a fixed bubble velocity, saturated liquid slugs, fixed catalyst coating thickness and a relatively thin liquid film and catalyst coating.

6.1 Introduction

One of the potential benefits of using micro-structured reactors for gas-liquid-solid reactions is the expected increased mass transfer rates that can be achieved in these devices, since traditional multi-phase reactors, e.g. slurry bubble columns and packed bed reactors, often operate under gas-liquid mass transfer limited conditions. Especially the application of monolith reactors and micro-capillary reactors, in which the catalyst has been coated on the walls of the micro-channels, has been the subject of research [1,2,3,4].

Apart from external mass transfer rate, the rate constant per unit of reactor volume also depends on whether mass transfer limitation in the catalyst occurs, and on the amount of catalyst per unit volume of capillary. The interfacial mass transfer rate depends strongly on the channel diameter and increases with decreasing channel diameter. The mass transfer rate in the catalyst layer by diffusion depends on the catalyst properties and the ratio between external catalyst surface and catalyst volume, i.e. the thickness of the catalyst layer and, to a lesser extent, the diameter of the micro-channel. The amount of catalyst per unit of capillary volume also depends on the catalyst layer thickness and the channel diameter. Therefore, it is important to choose the right combination of catalyst layer thickness and channel diameter for a given catalyst system in order to optimize the performance of the capillary.

Other than finding the optimum thickness of the catalyst layer and channel geometry, having reproducible fabrication methods for these catalyst coatings is also important for the design and construction of these devices. Rebrov and Berenguer-Murcia et al. [5] have recently published a new method for preparing thin film mesoporous titania catalyst supports. They deposited such a layer (thickness of $92\pm12\cdot10^{-9}$ m) containing 1 $wt\%_{coating}$ Pd nanoparticles on the interior of a glass micro capillary (inner diameter of $2.5\cdot10^{-4}$ m_c) and tested the performance of the catalyst in the hydrogenation of phenylacetylene. The focus of that work was on the catalyst fabrication method and demonstrating the catalysts activity over longer periods of time. It was shown that catalyst activity was maintained for over 1000 hours of operation at rates comparable to the homogeneous reaction using the same nanoparticles.

Since this is a promising catalyst for application in monolith and micro-capillary reactors, in this work, more experiments are performed with the focus on obtaining more

information on the catalyst activity and estimating the optimum catalyst layer thickness and channel diameter for further experiments.

6.2 Experiments

6.2.1 Catalyst preparation and properties

Two capillary micro reactors were constructed by coating the interior surface of a fused silica capillary with an internal diameter of $2.5 \cdot 10^{-4}$ m_c (Varian Inc.) with a mesoporous titania layer containing Pd nanoparticles. The development and characterization of such catalyst coatings was done by Rebrov and Berenguer-Murcia et al. [5], who also prepared the capillary micro reactors used in this study. Although the coatings used in this study have not been characterized, Rebrov and Berenguer-Murcia et al. have shown to be able to control the coating properties based on the applied recipe and processing conditions. The targeted properties of the coatings used in this work are given in Table 6.1.

6.2.2 Experimental set-up

One experimental set-up was used for both capillaries, but the length of the various pieces of tubing and capillaries were different for the set of experiments performed with capillary 1 and the set performed with capillary 2. All other pieces of equipment, including the gas-liquid mixer, were used in both set-setups. Figure 6.1 is a schematic overview of the used set-ups. The lengths and diameters of the various pieces of tubing are given in Table 6.2. The reactive capillaries were placed in a thermo stated GC-oven so that the reaction temperature could be regulated.

Table 6.1: Properties of the reactive capillaries used in this study. These catalyst layers were deposited on the interior surface of a glass capillary with a diameter of $2.5 \cdot 10^{-6}$ m. Note that these are the properties as aimed for during their synthesis. No characterization was done after their construction.

		Capillary 1	Capillary 2
Pd loading	**[wt%$_{coating}$]**	*1*	*2*
$d_{coating}$	**[10^{-9} $m_{coating}$]**	*120*	*120*
$\varepsilon_{coating}$	**[$m_l^3 m_{coating}^{-3}$]**	*0.4*	*0.4*
Length	**[m]**	*4.5*	*5*

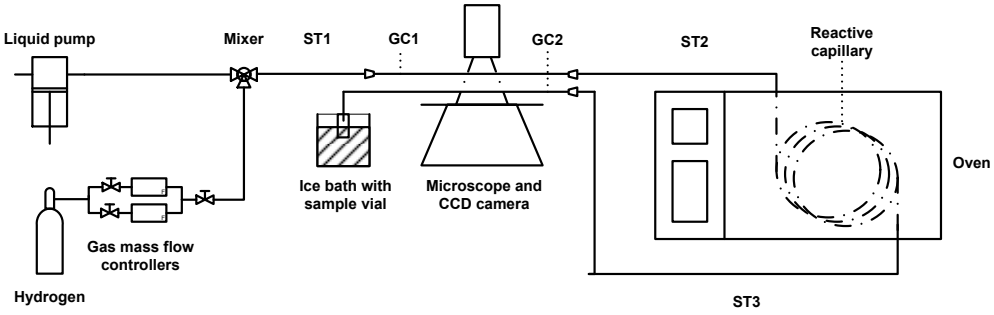

Figure 6.1: Schematic overview of both the set-ups used in this study. The difference between the two set-ups is the length of the various pieces of tubing and capillary. The length and diameters of these pieces are given in Table 6.2. The liquid flow is regulated using an ISCO 100D pump. One of two Bronckhorst mass flow controllers is used to control the hydrogen flow. The details of the mixer are given in figure 6.2. GC1 and GC2 are the transparant glass capillaries used to enable the recording of images of the flow, respectively, upstream and downstream of the reactive capillary.

Table 6.2: Length and diameter of the various pieces of tubing and capillary used in the two set-ups used in this study. The following abbreviations are used: "ST", indicating a piece of stainless steel tubing and "GC", indicating a glass capillary. Set-ups 1 and 2 were used with capillaries 1 and 2, respectively.

	Set-up 1		**Set-up 2**	
	Length [m]	**Diameter [10^{-6} m]**	**Length [m]**	**Diameter [10^{-6} m]**
ST1	0.18	250	0.18	250
GC1	0.97	140	0.75	140
ST2	1.09	250	0.89	250
ST3	0.22	250	1.20	250
GC2	1.36	140	1.36	140

The gas flow was regulated by one of two mass flow controllers depending on the required gas flow rate (Bronkhorst F-200C/Bronkhorst F-201C). The liquid flow was regulated with an Isco 100DM syringe pump. The liquid flow was split into two equal flows, which were contacted with the hydrogen flow in a stainless steel cross-mixer (Valco ZX.5) at an angle of 90^0 with respect to the direction of the gas flow (Figure 6.2). The inner diameter of the channels in the cross-mixer was $2.5 \cdot 10^{-4}$ m_c. A Redlake MotionPro CCD camera connected to a Zeiss Axiovert 200 MAT inverted microscope was used to record images of the gas-liquid flows at a frame rate of 500 frames per second for 10 seconds. An exposure

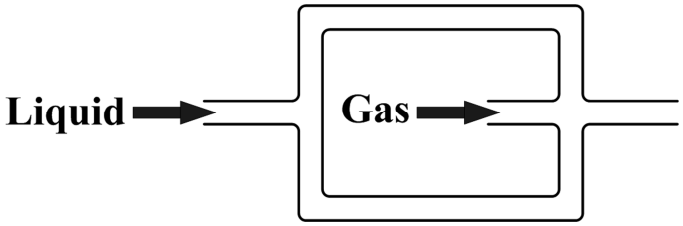

Figure 6.2: Schematic drawing of the cross-mixer. The liquid flow is split into two equal flows and contacted with the gas flow at an angle of 90°. All channels in the cross-mixer have a diameter of $2.5 \cdot 10^{-4}$ m.

time of 80 μs was used, which was sufficient for preventing any significant motion blur. The length of one pixel represented $3.8 \cdot 10^{-6}$ m of channel length. A channel length of $3.04 \cdot 10^{-3}$ m was captured in the images of which the center point was located 42 cm downstream from the cross-mixer. The flows in both the glass capillaries upstream and downstream (GC1 and GC2) of the reactive capillary were captured within one frame. Analysis of the images of the Taylor flow, using Matlab scripts written by the authors, gave: the number of bubbles passing the measurement location per unit time, the length of every observed gas bubble, the length of every observed liquid slug, and the velocity of every observed bubble.

6.2.3 Experimental conditons and procedure

All experiments were performed using a 10 % vol. solution of phenylacetylene in isopropanol which was fed to the reactive capillary ($D_c = 2.5 \cdot 10^{-4}$ m_c) at a superficial velocity of $1.7 \cdot 10^{-2}$ $m_l^3 m_c^{-2} s^{-1}$. The gas phase consisted of undiluted hydrogen. For all experiments carried out in the Taylor flow regime, the superficial gas velocity was 0.08 $m_g^3 m_c^{-2} s^{-1}$ (based on: $D_c = 2.5 \cdot 10^{-4}$ m_c, $T = 293$ K and $P = 1 \cdot 10^5$ Pa). In order to test if the observed reaction rates depend on the flow regime, experiments were also carried out at a superficial gas velocity of 4.53 $m_g^3 m_c^{-2} s^{-1}$. At this superficial gas velocity, the flow regime alternated between Taylor flow, ring flow and annular flow. Ideally, a steady annular or ring flow would be preferred, but while it was possible to achieve steady Taylor flow, it was not possible to obtain a steady ring or annular flow. An overview of the experimental conditions is given in Table 6.3.

The catalyst was reduced by flushing the capillary with undiluted hydrogen at a temperature of 473 K for 8 hours prior to its first use. After a run, the capillary was allowed to cool down while it was continuously flushed with isopropanol and hydrogen. Upon reaching ambient temperature, the hydrogen flow was shut down

Table 6.3: Overview of the experimental conditions used in the experiments. The superficial gas velocity is given at a temperature of 293 K and a pressure of $1 \cdot 10^5$ Pa. The superficial velocities are based on the diameter of the reactive capillary D_c, which is $2.5 \cdot 10^{-4}$ m_c.

	Reactive capillary	U_l [$m_l^3 m_c^{-2} s^{-1}$]	U_g [$m_g^3 m_c^{-2} s^{-1}$]	T [K]	Flow regime
Set-up 1	Capillary 1	0.017	0.080	313-343	Taylor
Set-up 2	Capillary 2	0.017	0.080	313-343	Taylor
	Capillary 2	0.017	4.526	313-343	Taylor-ring-annular

while maintaining an isopropanol flow until no hydrogen bubbles were present in the setup. Subsequently, the isopropanol pump was stopped and the capillary was thus completely filled with isopropanol during down time of the set-up. At the start of a new run with a previously used capillary, the catalyst was reduced by flushing the capillary with undiluted hydrogen for at least 2 hours at a temperature of 473 K. After every change in reaction conditions, the system was allowed to stabilize for 1 hour before liquid samples were taken and video images of the flows were recorded. The liquid was collected in a sampling vial cooled by an ice bath to prevent evaporation of liquid. The phenylacetylene conversion and selectivity were determined offline by GC-FID.

6.2.4 Estimating the pressure profiles and $k_{v,ov}$

Reaction rate

Chaudhari et al. [6] found the reaction from phenylacetylene to styrene to be first order in hydrogen and zeroth order in phenylacetylene until the phenylacetylene concentration is “very small”. They also showed that the secondary reaction of styrene to ethylbenzene is strongly inhibited by phenylacetylene as the reaction rate is relatively low and only increases “by several times” after phenylacetylene has been consumed. Similar results were also found by Jackson and Shaw [7], who state that the order of phenylacetylene changes from zeroth to first at a phenylacetylene to styrene ratio of 3:2, which corresponds to a phenylacetylene conversion of approximately 0.6. Since the reactions will be done for phenylacetylene conversions up to 0.2, the reaction rate can be described with a simple first order rate equation, depending on the hydrogen concentration in the liquid. The following equation can be derived for the change in the molar flow rate F_{H2} with changing position z in the reactive capillary.

$$-\frac{\mathrm{d}F_{H_2}}{\mathrm{d}z} = Ak_{v,ov}\frac{P}{H} \tag{6.1}$$

If the reaction would be limited by external mass transfer of hydrogen, a first order dependency will also be observed and equation (6.1) will also describe the results, albeit with different values for the overall volumetric reaction rate coefficient $k_{v,ov}$.

Pressure drop model selection: Taylor flow

In order to be able to properly interpret the reaction data, the pressure profile over the reactive capillary has to be known. Since no pressure transducers were available for these experiments, the pressure profile was calculated for each experiment. The Taylor flow pressure drop model developed in chapter 3 was used for all the experiments in the Taylor flow regime. This model was specifically developed for Taylor flow in small channels for Reynolds numbers Re_b up to 150 and capillary numbers Ca_b up to at least 0.01, and thus for We_b numbers up to 1.5. The maximum capillary, Reynolds and Weber numbers for the Taylor flow experiments done in this work are 0.03, 14 and 0.42, respectively and the model is thus expected to accurately describe the pressure drop in these experiments.

The pressure drop of a Taylor flow is described by (chapter 3):

$$-\left(\frac{\mathrm{d}P}{\mathrm{d}z}\right)_c = \frac{32\mu_l U_l}{D_c^2}\left(1+\frac{7.16\cdot 3^{\frac{2}{3}}}{32}\frac{D_c F_b}{U_l}\frac{1}{\left(Ca_b^{\frac{1}{3}}+3.34Ca_b\right)}\right) \tag{6.2}$$

The capillary number depends on the gas bubble velocity and thus on the pressure. Although the dependence of the superficial gas velocity on the pressure is straightforward by making use of the ideal gas law (equation (6.3)), the dependence of the gas bubble velocity u_b on the pressure P is more complicated, since it also depends on the liquid film thickness d_f (equation (6.4)), which, in turn, depends on the capillary number Ca_b and thus on the bubble velocity, as described by Aussillous and Quéré [8] (equation 6.5).

$$U_g = \frac{F_{H_2} RT}{A_c P} \tag{6.3}$$

$$\frac{A_b}{A_c} u_b = U_g + U_l \tag{6.4}$$

$$\frac{d_f}{D_c} = \frac{0.67 Ca_b^{\frac{2}{3}}}{1 + 3.34 Ca_b^{\frac{2}{3}}} \tag{6.5}$$

Therefore, when solving equation (6.2) numerically, the liquid film thickness and the gas bubble velocity at each location in the channel are calculated by an iteration of equations (6.4) and (6.5)

Pressure drop model selection: Taylor-ring-annular flow

Unfortunately, no such dedicated model is available for gas-liquid flows alternating between the Taylor, ring, and annular regimes. The options are then to: 1) use a dedicated model for Taylor flow, or 2) to use a more generic separated flow model, such as the Lockhart-Martinelli-Chisholm model [9,10], while accepting that neither can be expected to describe the pressure drop in these experiments with great accuracy. Using the model for the pressure drop of Taylor flow developed in chapter 3 is least appropriate, because inertial effects are not included in the model while they are significant in these experiments, as is evident from the ranges of Reynolds and Weber numbers used in these experiments (Re_{gl} < 675, We_{gl} < $1.1 \cdot 10^3$). Therefore, the Lockhart-Martinelli-Chisholm model was chosen to calculate the pressure profiles for the experiments performed in the Taylor-ring-annular regime. The model was specifically developed for annular flows, but does not include the effect of surface tension. Although surface tension forces are not negligible, as is evident from the occurrence of Taylor flow, the values of the Weber numbers for these experiments indicate that inertial forces are considerably larger than surface tension forces, allowing for some confidence in the estimation of the pressure profiles.

Calculation of the pressure profiles in GC2 and ST3

The gas and liquid exit capillary GC2 at ambient conditions (T=293 K and P = $1 \cdot 10^5$ Pa) and, since the gas and liquid feed flow rates and the gas and liquid conversions are known, the volumetric flow rates of both phases at exit conditions are also known. Using these values as boundary values, the pressure profiles in GC2 and ST3 were then calculated. The channel diameters of GC2 and ST3 are different and, in order to be able to calculate the pressure profile in ST 3, it was assumed that there were no significant pressure losses due to the change in channel diameter. This implies an instantaneous change in superficial gas and liquid velocities at the connection of the two channels since the mass flow rates are equal in both channels. For the Taylor flow it was furthermore assumed that the volumes of both the gas bubbles and the liquid slugs did not change as the channel diameter changed, thereby implying that the length of the gas bubbles and liquid slugs changed instantaneously while the bubble frequency was constant.

Calculation of the pressure profiles and $k_{v,ov}$ in the reactive capillaries: Taylor flow

To calculate $k_{v,ov}$ and the pressure profile over the reactive capillaries with Matlab, equations (6.1) and (6.2) need to be solved simultaneously, while also making use of equations (6.3), (6.4) and (6.5). In order to be able to solve this set of equations, the molar flow rates of hydrogen and the pressure at both the capillary entrance and exit need to be known. The molar flow rate of hydrogen at these locations is known from the molar feed flow rate of hydrogen and the hydrogen conversion. The pressure at the exit of the reactive capillary is assumed to be equal to the pressure at the entrance of ST3, which is known from calculating the pressure profile over ST3. This assumption implies that all changes in physical constants and the difference in superficial gas velocity, due to temperature difference between the reactive capillary and ST3, occur instantaneously and cause no additional pressure loss. The pressure at the entrance of the reactive capillary, however, is not known. To solve the problem using Matlab, a constant c is introduced in equation (6.2):

$$-\left(\frac{\mathrm{d}P}{\mathrm{d}z}\right)_c = c\frac{32\mu_l U_l}{D_c^2}\left(1+\frac{7.16\cdot 3^{\frac{2}{3}}}{32}\frac{D_c F_b}{U_l}\frac{1}{\left(Ca_b^{\frac{1}{3}}+3.34Ca_b\right)}\right) \tag{6.6}$$

If an arbitrary value of the pressure at the entrance of the reactive capillary is assumed, then all boundary conditions are known and the system can be solved obtaining values $k_{v,ov}$ and c. If the value of c is not equal to 1, which indicates that the calculated pressure profile is not in accordance with the model, the assumed value of the pressure at the inlet of the reactive capillary is adjusted and the procedure is repeated. This iterative loop is continued until the value of c is within 0.1% of 1.

Calculation of the pressure profiles and $k_{v,ov}$ in the reactive capillaries: Taylor-ring-annular flow

The model used to describe the pressure drop in the Taylor-ring-annular regime is the Lockhart-Martinelli-Chisholm model. The set of equations that need to be solved for these experiments are equations (6.1), (6.3) and the equations of the Lockhart-Martinelli-Chisholm model (see appendix 3.A). The molar feed flow rate of hydrogen in the experiments in Taylor-ring-annular regime is a factor 57 larger than that used in the Taylor flow experiments. It is expected that the hydrogen conversion is very small in the experiments carried out in Taylor-ring-annular regime. The influence of hydrogen consumption on the superficial gas velocity and thus on the pressure drop is then negligible. This simplifies the calculations of the values of $k_{v,ov}$ and the pressure profiles, since the pressure profiles can be calculated first, without taking hydrogen consumption into account, and these profiles can then be used for solving equation (6.1).

Physical properties of the phases

Since 90 vol. % of the liquid consists of isopropanol, it was assumed that the properties of the liquid phase were those of isopropanol. The values of the physical constants at the temperatures applied in the experiments were obtained by interpolation of literature data and are given in Table 6.4.

Table 6.4: Overview of the relevant physical properties of isopropanol and hydrogen at the temperatures applied in the experiments. Where applicable, the data were interpolated from the reported data in the source.

T [K]	σ [N m^{-1}] [11]	μ_l [Pa s] [11]	μ_g [Pa s] [11]	H [Pa m$_l^3$ mol^{-1}] [12]	$\mathcal{D}$ [m$_l^2$ s^{-1}] [13]
313	$1.98 \cdot 10^{-2}$	$1.3 \cdot 10^{-3}$	$9.2 \cdot 10^{-6}$	$2.51 \cdot 10^{4}$	$2.0 \cdot 10^{-9}$
323	$1.91 \cdot 10^{-2}$	$1.0 \cdot 10^{-3}$	$9.4 \cdot 10^{-6}$	$2.37 \cdot 10^{4}$	$2.6 \cdot 10^{-9}$
333	$1.83 \cdot 10^{-2}$	$0.8 \cdot 10^{-3}$	$9.6 \cdot 10^{-6}$	$2.23 \cdot 10^{4}$	$3.4 \cdot 10^{-9}$
343	$1.75 \cdot 10^{-2}$	$0.6 \cdot 10^{-3}$	$9.8 \cdot 10^{-6}$	$2.09 \cdot 10^{4}$	$4.4 \cdot 10^{-9}$

6.2.5 Experimental results

Conversion and selectivity

The conversion of phenylacetylene as a function of temperature for the three types of experiments is given in Figure 6.3. The phenylacetylene conversions for the experiments carried out in the Taylor flow regime with capillary containing the 1 $wt\%_{coating}$ Pd coating are equal to those carried out in the capillary containing 2 $wt\%_{coating}$ Pd. In the capillary containing 2 $wt\%_{coating}$ Pd, the conversion of phenylacetylene in the Taylor-ring-annular regime is larger than in the Taylor flow regime, for each temperature.

The selectivity towards styrene for all experiments is given in Figure 6.4. With increasing temperature, and thus with increasing phenylacetylene conversion, the selectivity towards styrene decreases slightly, but was above 0.92 for all experiments.

The hydrogen conversion is then calculated from the molar hydrogen feed flow rate, the selectivity towards styrene, and the phenylacetylene conversion and the result is given in Figure 6.5. The hydrogen conversion in the Taylor flow experiments at a given temperature is nearly the same for both capillaries and increases from 0.21 to 0.53 with increasing temperature. The hydrogen conversion for the experiments carried out in the

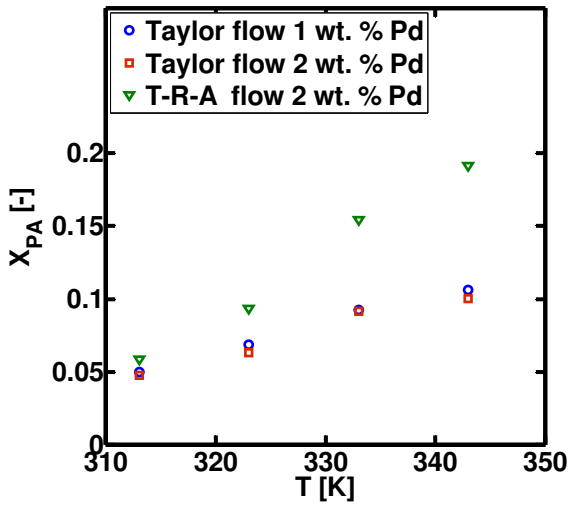

Figure 6.3: The conversion of phenylacetylene as a function of temperature for: the gas-liquid Taylor flow regime in the 1$wt\%_{Coating}$ and 2 $wt\%_{coating}$ capillaries and for the Taylor-ring-annular regime in the 2 $wt\%_{coating}$ capillary.

Taylor-ring-annular regime in the capillary with 2 wt%$_{coating}$ Pd increases from $2.4 \cdot 10^{-3}$ to $1.7 \cdot 10^{-2}$ with increasing temperature.

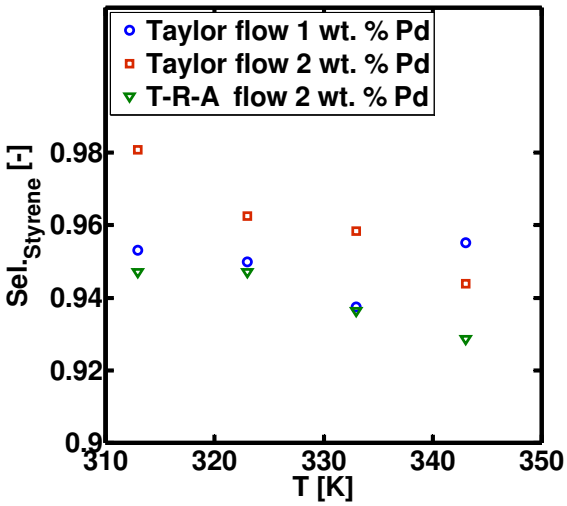

Figure 6.4: The selectivity towards styrene for: the gas-liquid Taylor flow regime in the 1wt% $_{ating}$ and 2 wt%$_{coating}$ and for the Taylor-ring-annular regime in the 2 wt%$_{coating}$ capillary.

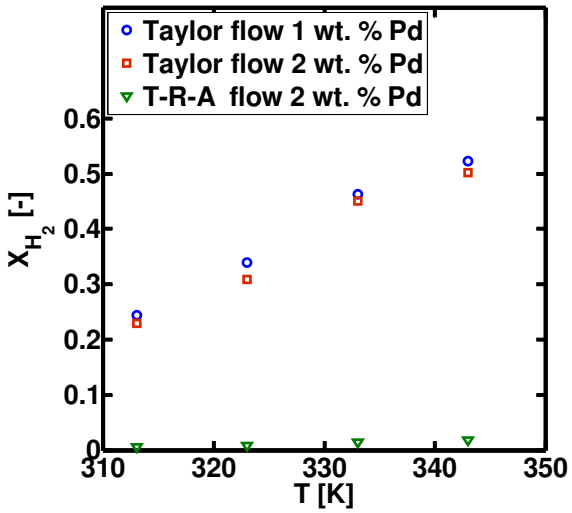

Figure 6.5: The conversion of hydrogen as a function of temperature for: the gas-liquid Taylor flow regime in the 1wt%$_{Coating}$ and 2 wt%$_{coating}$ capillaries and for the Taylor-ring-annular regime in the 2 wt%$_{coating}$ capillary.

Image analysis

Results from image analysis are only relevant for the Taylor flow regime, since the liquid film thickness for the annular and ring flow sections of the Taylor-annular-ring flow could not be accurately determined from these images. For every recorded movie, the standard deviations of the slug length L_s, the bubble length L_b, and the bubble velocity u_b were less than 0.5% of the respective average values for that movie. Thus, the hydrodynamics varied little during the time span of recording the movie, which was 10 seconds. There was, however, some variation in hydrodynamics over longer periods of time, although the standard deviation of each parameter was approximately 10% of its time averaged value. The values of the various parameters determined from image analysis of data recorded upstream of the reactive capillary (GC1) were averaged over all the experiments performed in that capillary. These results are given in Table 6.5.

Table 6.5: Averaged values (Av.) and their standard deviation (Std.) of the various hydrodynamic parameters obtained from image analysis of images recorded upstream of the reactive capillaries in GC1. Note that the diameter of GC1, $D_{c,GC1}$, is $1 \cdot 10^{-4}$ m, rather than $2.50 \cdot 10^{-4}$ m_c for the reactive capillary.

	$L_b/D_{c,GC1}$ [m_b m_c^{-1}]		$L_s/D_{c,GC1}$ [m_s m_c^{-1}]		F_b [s^{-1}]		u_b [m s^{-1}]	
	Av.	**Std.**	**Av.**	**Std.**	**Av.**	**Std.**	**Av.**	**Std.**
Capillary 1	119	11	101	11	4.2	0.3	0.13	0.01
Capillary 2	114	12	102	6	4.2	0.3	0.13	0.01

Pressure drop

The pressures at the entrance and exit of the reactive capillaries are given in Table 6.6. For the Taylor flow experiments, the difference in pressure drop at the capillary entrance and exit, due to gas consumption and gas expansion, was smaller than 3% of the value at the capillary entrance. For the experiments carried out in the Taylor-ring-annular regime, this difference was less than 6% of the value at the capillary entrance. The calculated pressure profiles over the reactive capillaries are, therefore, in good approximation, linear. Furthermore, the variation of the average pressure as a function of temperature, for a given capillary and flow regime, was less than 4% of the maximum average pressure for that capillary and flow regime.

Table 6.6: For each experiment, the temperature, the flow regime and the pressure at the entrance and exit of the reactive capillary are given. The pressure profiles over the reactive capillaries are, in good approximation, linear.

Reactive capillary	Flow regime	T [K]	$P_{entrance}$ [10^5 Pa]	P_{exit} [10^5 Pa]
Capillary 1	Taylor flow	313	4.5	3.9
	Taylor flow	323	4.4	3.9
	Taylor flow	333	4.3	3.9
	Taylor flow	343	4.3	3.9
Capillary 2	Taylor flow	313	4.8	4.2
	Taylor flow	323	4.7	4.2
	Taylor flow	333	4.5	4.1
	Taylor flow	343	4.5	4.1
Capillary 2	Taylor-ring-annular	313	12.8	11.0
	Taylor-ring-annular	323	12.6	10.9
	Taylor-ring-annular	333	12.4	10.9
	Taylor-ring-annular	343	12.2	10.9

Overall volumetric reaction rate coefficient $k_{v,ov}$ and activation energy E_{app}

The selectivity towards styrene was above 0.92 and varied only slightly with temperature. The assumption that the overall reaction rate of hydrogen is hardly influenced by the hydrogenation of styrene to ethylbenzene is warranted.

The overall volumetric reaction rate coefficient as a function of temperature is given in Figure 6.6. For the Taylor flow regime, the values of $k_{v,ov}$ at a given temperature are lower for the capillary with the larger Pd content, while both are larger than the values obtained for the Taylor-ring-annular regime.

For each of these three series of $k_{v,ov}$ as a function of temperature, the apparent activation energy E_{app} can be calculated from an Arrhenius plot of the same data. The results are given in Table 6.7. The apparent activation energy obtained from the experiments carried out in the Taylor flow regime is the same for both capillaries. For the Taylor-ring-annular flowregime, the apparent activation energy appears to be approximately 50 % larger. However, statistically, the values of the apparent activation energy can not be shown to differ significantly from each other, due to the larger overlap of the respective confidence intervals.

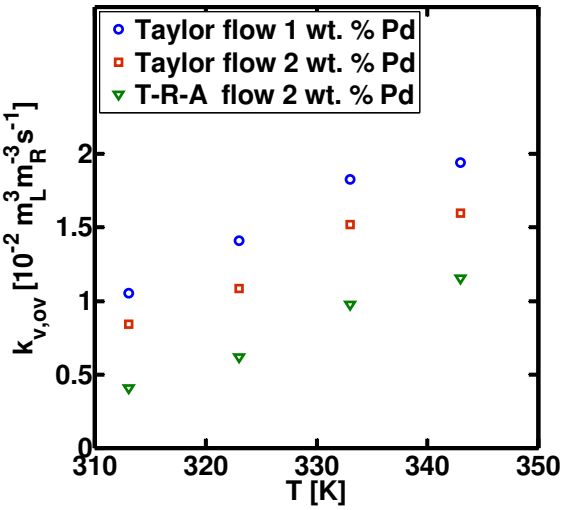

Figure 6.6: The overall reaction rate constant $k_{v,ov}$ as a function of temperature for: the gas-liquid Taylor flow regime in the 1wt%$_{Coating}$ and 2 wt%$_{coating}$ capillaries and for the Taylor-ring-annular regime in the 2 wt%$_{coating}$ capillary.

Table 6.7: Apparent activation energy E_{app} and the 95% confidence interval obtained from the Arrhenius plot of the data in Figure 6.6.

Reactive capillary	Flow regime	E_{app} [kJ/mol]	95 % c.i. [kJ/mol]
Capillary 1	Taylor flow	19	± 13
Capillary 2	Taylor flow	20	± 15
Capillary 2	Taylor-ring-annular	32	± 16

Catalyst deactivation

Deactivation of capillary 1 was observed at a temperature of 353K. Partial regeneration was possible after flushing the capillary with hydrogen for 8 hours at a temperature of 473 K. All the data presented in this work, have been recorded prior to heating the capillary 1 to 353K. Capillary 2 was never heated to temperatures beyond 343K.

6.2.6 Discussion

Volumetric reaction rate coefficient $k_{v,ov}$ and apparent activation energy E_{app}

External mass transfer rates in channels of comparable diameters are generally 2 orders of magnitude larger than the values of $k_{v,ov}$ observed in this work and internal diffusion limitations generally occur for catalyst layers one to two orders of magnitude thicker than used in this work. It is, therefore, expected that the reaction rates were not limited by either internal or external mass transfer. In this respect, the data in Figure 6.6 and Table 6.7 show a few unexpected results.

1) The value of $k_{v,ov}$ does not increase with increasing catalyst loading at a given temperature, similar pressure, and similar hydrodynamics

2) The value of $k_{v,ov}$ varies with the applied flow regime at equal catalyst loading and temperature.

3) The apparent activation energy is approximately half of the value reported in literature [6], where an activation energy of 52 kJ/mol was found for the same reaction on a 0.1 $wt\%_{catalyst}$ Pd/C catalyst and both internal and external mass transfer limitations were absent.

Although internal and external mass transfer limitations are not expected to be relevant, observations 1 and 2 could be explained by external mass transfer limitations. Observation 3 is typical for a reaction limited by internal mass transfer [14]. It should also be noted that the temperature dependency of the diffusion coefficient of hydrogen in isopropanol also yields an activation energy 23.6 kJ/mol. As will be shown later in this chapter, external mass transfer for Taylor flow can be described by film theory for these experiments, which depends linearly on the diffusion coefficient. If present, external mass transfer limitations would also have resulted in apparent activation energy of approximately 24 kJ/mol, provided that the thickness of the liquid film hardly varies with varying temperature. It will be first determined whether internal and/or external mass transfer effects were relevant in these experiments.

Furthermore, as the pressure profiles were calculated from models rather than measured, an analysis will be made of the effect of a measure of inaccuracy of these calculated profiles on the values of $k_{v,ov}$,, which may also have affected the values found for E_{app}.

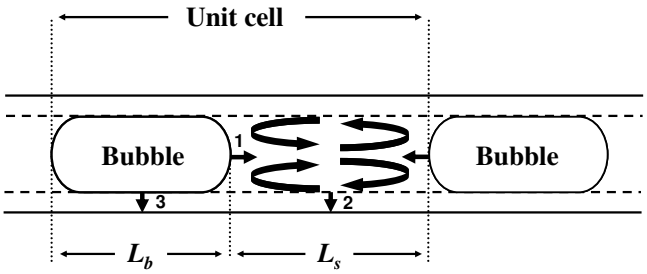

Figure 6.7: Three mass transfer steps for gas component mass transfer to the catalyst at the channel wall: 1) from the bubble caps to the liquid slug, 2) from the liquid slug through the liquid film to the catalyst, and 3) from the gas bubble through the liquid film to the catalyst. The definitions of a unit cell, the bubble length L_b and the liquid slug length L_s are also indicated.

Since catalyst deactivation was also observed at a temperature of 353 K, it will also be discussed whether catalyst deactivation at lower temperatures might have occurred and what its influence will be on the observed results. As the properties of the catalyst coatings of the capillaries were not determined after their synthesis, it is possible that the properties of the coatings were not as targeted for in one or both of the capillaries. It will also be discussed what implications this might have with respect to the observed results.

Estimating gas-liquid mass transfer coefficients

Assuming gas side mass transfer resistances are negligible, three steps for gas component mass transfer are identified [15] for a gas-liquid-solid reaction occurring at the channel wall under Taylor flow conditions, as illustrated in Figure 6.7:

1) mass transfer from the gas bubbles to the liquid slug,

2) mass transfer from the liquid slug to the catalyst and,

3) mass transfer from the gas bubble through the liquid film to the catalyst,

where steps 1 and 2 occur in series, parallel to step 3.

For mass transfer from the gas bubble to the wall of the channel through the liquid film (step 3), film theory can be used to calculate the mass transfer coefficient $k_{l,b}$. Multiplying $k_{l,b}$ with the interfacial area between the gas bubble and the liquid film, divided by the volume of a unit cell, gives the volumetric mass transfer coefficient:

$$k_{l,bf}a_{bf} = \frac{4}{D_c}\left(1-2\frac{d_{coating}}{D_c}-2\frac{d_f}{D_c}\right)\frac{\mathcal{D}}{d_f}\frac{L_b}{L_b+L_s} \tag{6.7}$$

Note that it is implicitly assumed that the liquid film is of equal thickness along the whole length of the gas bubble. Although this is not entirely correct, the influence thereof on the estimated mass transfer coefficient is small, as the combined length of both gas bubble caps amounts to approximately 5% of the total gas bubble length for the experiments carried out in this work. Using film theory rather than penetration theory to describe the mass transfer in the liquid film surrounding the gas bubbles is valid, since the value of the Fourier number (6.8) varied between 30 and 80 for the experiments carried out in this work. The concentration profile in the liquid film is, therefore, fully developed along most of the gas bubble length.

$$Fo = \frac{\mathcal{D}}{d_f^2}\frac{L_b}{u_b} \tag{6.8}$$

In principle, mass transfer from the liquid slug to the capillary wall, step 2, can also be described by film theory, as the Fourier number for the liquid film surrounding the slugs varied between 29 and 58. This leads to an equation similar to equation (6.7), although the thickness of the liquid film may be different and the term $L_b/(L_b+L_s)$ must be replaced by $L_s/(L_b+L_s)$. The capillary numbers in the reactive capillaries are in the order of $2\cdot10^{-3}$ and Kreutzer et al. [1] showed, by comparing the work of Thulasidas et al.[16] and Aussillous and Quéré [8], that for $Ca_b < 0.01$, there is no difference in the thickness of the liquid film surrounding the gas bubbles and the film surrounding the liquid slugs.

The only difference between mass transfer through a unit length of film surrounding the gas bubbles and through a unit length of film surrounding the liquid slug, is that the hydrogen concentration at the bubble-film interface is the saturation concentration, while it may be smaller at the slug-film interface. The concentration on the slug-film interface depends on the volumetric mass transfer coefficient of step 1 relative to that of step 2. Modeling the volumetric mass transfer coefficient for step 1 is more difficult than for the other steps, since it involves both diffusion and convection. Rather than modeling this explicitly, the maximum and minimum combined contribution of steps 1 and 2 to the overall volumetric mass transfer coefficient is more easily evaluated, which is sufficient for

estimating whether external mass transfer could have had an effect on the performed experiments.

The hydrogen concentration in the liquid slug can, in principle, vary between zero and the saturation concentration. The minimum mass transfer rate is obtained when the hydrogen concentration in the liquid slug is close to zero and only step 3) contributes to mass transfer. The volumetric mass transfer coefficient is then equal to $k_{l,bf}a_{bf}$ as given in equation (6.7). The maximum mass transfer rate to the catalyst is obtained when the liquid slug is saturated with hydrogen. In that case, the mass transfer rate through the liquid film is independent of whether the film is in contact with a gas bubble or a liquid slug. The volumetric mass transfer coefficient is then given by:

$$k_{l,bf}(a_{bf}+a_{sf}) = \frac{4}{D_c}\left(1-2\frac{d_{coating}}{D_c}-2\frac{d_f}{D_c}\right)\frac{\mathcal{D}}{d_f} \tag{6.9}$$

Thus, the equations for the minimum and maximum values for the combined volumetric mass transfer coefficient of steps 1,2 and 3, $k_{v,\ mass\ transfer}$ are equations (6.7) and (6.9), respectively.

For the experiments performed in this work, the following values of the parameters in equations (6.7), (6.8) and (6.9) are typical: $L_b/(L_b+L_s)$ = 0.55, d_f = 2.8·10^{-6} m$_l$ and $d_{coating}$ = 120 ·10^{-9} m$_{coating}$. The values of the minimum and maximum volumetric mass transfer coefficients and $k_{v,ov}$ at each temperature are given in Table 6.8. The minimum volumetric mass transfer coefficients are at least 2 to almost 3 orders of magnitude larger than $k_{v,ov}$, so external mass transfer limitation was not relevant in these experiments.

Table 6.8: Minimum and maximum values for the volumetric mass transfer coefficient $k_{v,mass\ transfer}$, for the Taylor flow experiments as calculated from equations (6.7) and (6.9), respectively, using $L_b/(L_b+L_s)$ = 0.55 and d_f = 2.810^{-6} m$_l$ at the temperatures used in the experiments. The overall volumetric reaction rate constants $k_{v,ov}$ for both capillaries are also given at these temperatures.

T [K]	$k_{v,mass\ transfer}$ [m$_l^3$ m$_c^{-3}$ s^{-1}]		$k_{v,ov}$ [m$_l^3$ m$_c^{-3}$ s^{-1}]	
	Minimum	**Maximum**	**Capillary 1**	**Capillary 2**
313	6.1	11.1	0.011	0.008
323	8.1	14.7	0.014	0.011
333	10.1	19.2	0.018	0.015
343	13.5	24.6	0.019	0.016

Although external mass transfer limitations in the Taylor-ring-annular regime are more difficult to model, the main principle is the same: diffusion of gas component through a liquid film. The thickness will most likely be different for Taylor, annular and ring sections of the liquid film for a given experiment, but will all be larger than the thickness of the liquid film observed in the Taylor flow regime at the same temperature, due to the larger velocities of the phases. However, even if liquid would occupy half of the channels cross-sectional area, resulting in $d_f = 3.6 \cdot 10^{-5}$ m_l, the values for $k_{v,mass\ transfer}$ based on equation (6.9), are still 2 orders of magnitude larger than the values for $k_{v,ov}$. Mass transfer limitations were therefore not relevant for the experiments carried out in the Taylor-ring-annular regime.

Effectiveness of the catalyst

Whether mass transfer limitations in the catalyst layer were significant for these experiments is determined by calculating the Thiele modulus φ and the effectiveness factor η. For a (pseudo-)first order reaction, the Thiele modulus is given by:

$$\varphi = d_{coating,eff} \sqrt{\frac{k_{v,coating}}{\mathcal{D}_{eff}}} \tag{6.10}$$

where $d_{coating,eff}$ is defined as the volume of the catalyst layer divided by the external surface area of the catalyst [14], $k_{v,coating}$ is the rate coefficient per unit volume of catalyst coating, and D_{eff} is the effective diffusion coefficient in the catalyst layer. For a circular capillary of diameter D_c and a catalyst coating of uniform thickness $d_{coating}$, the effective coating diameter $d_{coating,eff}$ is given by:

$$d_{eff,coating} = \frac{\left(\frac{D_c}{2}\right)^2 - \left(\frac{D_c}{2} - d_{coating}\right)^2}{2\left(\frac{D_c}{2} - d_{coating}\right)} \tag{6.11}$$

The targeted thickness of the catalyst layer is 120 nm and the channel diameter, prior to catalyst deposition, is $2.5 \cdot 10^{-4}$ m_c, resulting in $d_{coating,eff} = 120 \cdot 10^{-9}$ $m_{coating}$ and $k_{v,\ coating} = k_{v,ov} / 1.9 \cdot 10^{-3}$ $m_l^3 m_{coating}^{-3} s^{-1}$. The effective diffusion coefficient is given by:

$$\mathcal{D}_{eff} = \frac{\mathcal{D}\varepsilon_{coating}}{\tau} \tag{6.12}$$

The targeted porosity of the catalyst layer $\varepsilon_{coating}$ =0.4 $m_l^3 m_{coating}^{-3}$. The tortuosity factor τ is not known, but is assumed to be 1.7, which is a typical value for random pore structures [14].

$$\eta = \frac{\tanh(\varphi)}{\varphi} \tag{6.13}$$

The Thiele modulus varied between $8 \cdot 10^{-3}$ and $1.3 \cdot 10^{-2}$ for these experiments and thus the effectiveness factor η was equal to 1 for all experiments, indicating that internal mass transfer limitations were not present in any of the experiments.

Accuracy of the pressure profiles and its influence on the observed values of $k_{v,ov}$

In absence of mass transfer effects and an apparent first order dependency of the reaction rate on the partial hydrogen pressure, the value of $k_{v,ov}$ at a certain temperature is expected to be equal for the experiments carried out in the same capillary, regardless of the applied flow regime. However, from Figure 6.6 it is clear that, for the experiments carried out in capillary 2, the values of $k_{v,ov}$ are lower for the Taylor-ring-annular regime than for the Taylor flow regime. However, the trends of $k_{v,ov}$ versus temperature are the same, which is according to expectations, since the exact same catalyst was used and both internal and external mass transfer effects are absent.

Note that the Lockhart-Martinelli-Chisholm model was used to estimate the pressure profiles in the Taylor-ring-annular regime, because a better model was not available. The model is known to be inaccurate in describing the pressure drop of gas-liquid flows in micro channels, in some cases up to a mean deviation of 100 % of the measured values [17]. It is therefore likely that the pressure profiles calculated with this model, and hence the respective $k_{v,ov}$ values, are inaccurate. The gas and liquid mass feed flow rates were equal at all temperatures, but a change in reaction temperature will cause a different pressure drop over the reactive capillary due to the temperature depency of the physical properties of the phases. However, the effect on the average pressure in the reactive capillary is small, since the pressure drop over the reactive capillary is small compared to

the pressure at the exit of the reactive capillary, which is determined by the pressure drop over the non-heated section downstream of the reactive capillary. Thus, even though an error is likely for the value of $k_{v,ov}$ at a given temperature, approximately the same absolute error is made for all temperatures. The temperature dependency of $k_{v,ov}$ is, therefore, hardly influenced by this error. It is likely that this is the cause for the observed differences between the values of $k_{v,ov}$ in the Taylor flow regime and those in the Taylor-ring-annular regime, while the trends of $k_{v,ov}$ versus temperature, and thus the apparent activation energy, are similar for both regimes.

Furthermore, since both internal and external mass transfer limitations were shown not to be present during these experiments, it was expected that, for a given temperature, the value of $k_{v,ov}$ for the 2 $wt\%_{coating}$ Pd would be twice that for the 1 $wt\%_{coating}$ Pd. However, the expected trend is not observed (Figure 6.6) and the value of $k_{v,ov}$ is slightly lower for capillary 2, even though it has a higher Pd loading. If inaccuracy of the calculated pressure profiles for the Taylor flow would be the cause of the lower values of $k_{v,ov}$ in the capillary containing a higher catalyst loading, then 1) the actual pressures in capillary 2 should have been approximately half those in capillary 1, and 2) the model would have failed to predict this difference. Such a difference in pressure would cause a difference in observed gas bubble length and/or bubble frequency in the viewing capillaries upstream of the reactive capillaries (GC1). This difference was not observed from image analysis, supporting the calculated result of nearly equal pressure profiles in both capillaries. It is therefore concluded that the properties of one or both of the catalyst coatings were most likely not as targeted in their synthesis, leading to them having the same activity per unit of capillary volume.

Thus, inaccuracy of the pressure profiles, which is most likely for the Taylor-annular-ring regime, can be the cause of the “off-set” between the values for $k_{v,ov}$ for the two flow regimes in capillary 2. However, it can not explain why the value of $k_{v,ov}$ did not vary with catalyst loading.

Catalyst deactivation

Catalyst deactivation was observed in capillary 1 at a temperature of 353K and was only partly reversible by flushing with hydrogen at a temperature of 473 K for 8 hours. The onset of deactivation may have occurred at lower temperatures, which would then influence the

trend of $k_{v,ov}$ versus temperature and the apparent activation energy. However, for capillary 1, the chronological order of the temperatures at which the experiments were performed was: 333K, 323K, 343K and 313K. The experiments at a temperature of 313K were done after those at 343K and the value of $k_{v,ov}$ at a temperature of 313K does not deviate from the trend. It is, therefore, unlikely that catalyst deactivation has significantly influenced these results.

Properties of the catalyst coatings

It is possible that, for whatever reason, the properties of the catalyst coatings in either or both of the capillaries were not as targeted, since no characterization was done after their synthesis. This may explain why $k_{v,ov}$ may be lower for the capillary with the higher targeted Pd content, for otherwise identical conditions. However, it can not explain why there is a difference between the values of $k_{v,ov}$ with varying flow regime for the same capillary and thus for the same catalyst.

Comparison with other studies of the hydrogenation of phenylacetylene on Pd catalysts

Although a number of unexpected results can be explained by one or several of the previously mentioned causes, an explanation for the relatively low values for the apparent activation energy has not yet been found.

Chaudhari et al. [6] performed the hydrogenation of phenylacetylene on a 0.1 $wt\%_{catalyst}$ Pd/C catalyst. They convincingly show that neither internal nor external mass transfer effects were present for the measurements from which they calculated the activation energy. They found a value of 51.5 kJ/mol for the activation energy of the hydrogenation of phenylacetylene to styrene and a value of 53.6 kJ/mol for the hydrogenation of styrene to ethylbenzene. At a temperature of 318 K and a hydrogen pressure of $14.7 \cdot 10^5$ Pa, they found a catalyst activity of $2.5 \cdot 10^{-2}$ $mol \cdot_{H2} \cdot g_{Pd}^{-1} \cdot s^{-1}$. In this work, at a temperature of 313 K and an average hydrogen pressure of $4.2 \cdot 10^5$ Pa, a catalyst activity of $6 \cdot 10^{-3}$ $mol \cdot_{H2} \cdot g_{Pd}^{-1} \cdot s^{-1}$ was found, based on the capillary targeted to contain 1 $wt\%_{coating}$ Pd. The activities are almost equal when taking the difference in hydrogen pressure and temperature into account.

The activation energy found in this work is approximately half the value found by Chaudhari et al. However, Jackson and Shaw [7] report an apparent activation energy of 26

± 2 kJ/mol for the same reaction, also on a Pd/C catalyst, but internal mass transfer limitations can not be ruled out from their data.

The question is then if the lower activation energy found in this work can be explained by differences in properties of the catalyst. First of all, the support material used in the literature studies differs from that used in this work. Furthermore, the activity of a Pd/TiO_2 catalyst, which is used in this work, was shown to be dependent on both the temperature at which the catalyst was reduced, as well as on the size of the palladium particles [18,19]. It is also commonly reported that the activity of Pd catalysts in hydrogenation of alkynes depends on the size of the Pd particles [18,20], although there is still discussion on the exact mechanism. However, no literature was found describing the activation energy as a function of the conditions at which the Pd/TiO_2 catalyst has been reduced, or of the particle size of Pd. Although there are a number of reasons for the catalyst activity to vary between the work of Chaudhari et al. and this work, whether they also explain a difference in temperature dependency of this activity, and thus in the apparent activation energy, is unclear.

6.2.7 Conclusions experimental results and recommendations for future work

The hydrogenation of phenylacetylene in isopropanol was performed over Pd supported on mesoporous titania films coated on the walls of a glass capillary with an inner diameter of $2.5 \cdot 10^{-4}$ m_c. Two such capillaries were constructed by Berenguer-Murcia targeted to have a coating thickness of $120 \cdot 10^{-9}$ $m_{coating}$. The palladium loading, consisting of Pd particles with a diameter of 2 nm, was intended to vary between the two capillaries and targeted to be, respectively, 1 $wt\%_{coating}$ and 2 $wt\%_{coating}$. The reaction was performed in the Taylor flow regime as well as in the Taylor-ring-annular regime at temperatures varying from 313 to 343 K and phenylacetylene conversions smaller than 0.2. The selectivity towards styrene was above 0.92 for all experiments. The pressure in the reactive capillaries was estimated from model calculations. The catalyst has an activity $1.3 \cdot 10^{-2}$ $mol \cdot_{H2} \cdot g_{Pd}^{-1} \cdot s^{-1}$ at a temperature of 343 K and at an average hydrogen pressure of $4.2 \cdot 10^{5}$ Pa. Its activity at lower temperatures was comparable to literature data [6].

Analysis of the reaction data shows some unexpected results, which can not be attributed to internal and/or external mass transfer effects, as these were shown not to be limiting for these experiments. Other possible sources for these results were evaluated and

although they may explain some results; others remain unresolved at this point. The unexpected results were:

- The value of the overall reaction rate coefficient does not increase with increasing catalyst loading at a given temperature, similar pressure, and similar hydrodynamics.

- The value of the overall reaction rate coefficient varied with the applied flow regime at equal catalyst loading and temperature.

- The apparent activation energy is approximately half the value reported in literature for the same reaction, although the catalyst support was different.

It has been argued that inaccuracy of the calculated pressure profiles, which is more likely for the Taylor-ring-annular regime, can only explain the offset between the overall volumetric mass transfer coefficient versus temperature for the Taylor flow and the Taylor-ring-annular regime. However, it can not explain the fact that approximately the same values of overall volumetric reaction rate were found for different catalyst loadings and otherwise nearly identical conditions. The latter could be explained if the properties of the catalyst coatings were not as targeted for during their synthesis. However, it is not known if the properties of the catalyst were as intended, since the catalysts have not been characterized after construction or after experiments. Finding a different value of the activation energy compared to literature may be due to a possible difference of size of the Pd particles and/or due to a difference in support material. Furthermore, the activation energy may vary with conditions at which the catalyst has been reduced. It is, therefore, recommended to:

- repeat these experiments with pressure measurements before and after the reactive capillaries,

- gather more data in order to better quantify the activation energy, and

- characterize the reactive capillaries before and after performing a series of experiments.

6.3 Dimensioning of the capillary diameter and catalyst layer thickness

The overall volumetric reaction rate coefficient in the current capillaries is low, due to the low amount of catalyst per unit volume of capillary, which is 3 $kg_{coating}/m_c^3$. The catalyst loading can be increased by reducing the channel diameter, increasing the catalyst layer thickness, or both. Reducing the channel diameter will also increase mass transfer rates and increasing the catalyst layer thickness may result in significant diffusion limitations within the catalyst layer. For research on catalyst systems and reaction kinetics, it is usually preferred to avoid diffusion within the catalyst, affecting the reaction rates. The goal for this purpose is then twofold; 1) to determine the maximum catalyst layer thickness for which internal diffusion is not significant 2) to determine, based on this thickness, the maximum channel diameter for which external mass transfer is not significant. It is also interesting to study a broader range of catalyst layer thicknesses and channel diameters, accepting external and/or internal mass transfer to affect the volumetric reaction rate coefficient, in order to study the limit of $k_{v,ov}$ as a function of channel diameter.

Table 6.9: values used for the calculations of $k_{v,catalyst}$ and $k_{v,mass\ transfer}$ based on the data of the gas-liquid Taylor flow experiments performed in capillary 1 at a temperature of 343K.

T	343	**[K]**
$k_{v,coating}$	10	**[$m_l^3 m_{coating}^{-3} s^{-1}$]**
D_c	0.1 - 2.5	**[10^{-3} m]**
$\mathcal{D}$	$4.4 \cdot 10^{-9}$	**[$m_l^2\ s^{-1}$]**
$\mathcal{D}_{eff}$	$1.0 \cdot 10^{-9}$	**[$m_l^3\ m_{coating}^{-1}\ s^{-1}$]**
μ_l	0.64	**[10^{-3} Pa s]**
σ_l	$1.9 \cdot 10^{-2}$	**[N m^{-1}]**
u_b	0.035	**[m s^{-1}]**

The calculations will be based on the data obtained for Taylor flow in the capillary 1 at a temperature of 343 K, since this was the highest value observed for $k_{v,ov}$ (Table 6.8). The catalyst coating in the capillary was targeted to have thickness $d_{coating}$ of $120 \cdot 10^{-9}$ m and a loading of 1 $wt\%_{coating}$ Pd. Although there are still some unresolved issues regarding the data, for these calculations it is assumed that the value of $k_{v,ov}$ is based on intrinsic kinetics. Furthermore, the catalyst activity per gram Pd per unit time was very close to data reported in literature for the same reaction on a Pd on carbon catalyst [6]. Further assuming the catalyst properties to be as targeted, the reaction rate coefficient per unit volume of catalyst coating $k_{v,coating}$ is then equal to 10 $m_l^3 m_{coating}^{-3} s^{-1}$. The data used for these calculations are given in Table 6.9.

Volumetric reaction rate of the catalyst $k_{v,\,catalyst}$

For a given channel diameter D_c and a thickness of the catalyst coating $d_{coating}$, the volumetric fraction of catalyst in the channel $f_{v,coating}$ is given by:

$$f_{v,coating} = \frac{\left(0.5D_c\right)^2 - \left(0.5D_c - d_{coating}\right)^2}{\left(0.5D_c\right)^2} = 4\left(\frac{d_{coating}}{D_c} - \left(\frac{d_{coating}}{D_c}\right)^2\right) \tag{6.14}$$

The volumetric reaction rate coefficient based on a unit of capillary volume $k_{v,catalyst}$ is then:

$$k_{v,catalyst} = \eta f_{v,coating} k_{v,coating} \tag{6.15}$$

where η is the effectiveness factor as calculated from equations (6.10), (6.12) and (6.13).

Volumetric mass transfer coefficient $k_{v,\,mass\ transfer}$

The calculations will be based on the maximum mass transfer coefficient per unit of capillary volume $k_{v,mass\ transfer}$ as given by equation (6.9). As discussed earlier in this chapter, this implies the liquid slugs being saturated with hydrogen, which imposes a maximum on the liquid slug length that can be used in practice. Furthermore, the thickness of the liquid film surrounding the liquid slug must be equal to that of the film surrounding the gas bubble, which is obtained if the capillary number Ca_b is kept below 0.01 [1]. When these conditions are met, there is no difference with respect to mass transfer through the liquid film when it is in contact with a gas bubble, or with a liquid slug. This also means that, apart from start-up, the concentration profile in the liquid film will not change in time, which is not necessarily the case for long, unsaturated liquid slugs.

Overall volumetric reaction rate coefficient $k_{v,\,ov}$

Following the theory of resistances in series, the overall reaction rate coefficient per unit of capillary volume is given by:

$$\frac{1}{k_{v,ov}} = \frac{1}{k_{v,mass\ transfer}} + \frac{1}{k_{v,catalyst}} \tag{6.16}$$

The following criteria are used to determine whether or not the overall volumetric reaction rate coefficient is fully determined by external mass transfer and whether or not internal diffusion significantly affects the rate coefficient:

- internal mass transfer is not significant when: $\varphi \leq 0.4$ [21]
- external mass transfer is not significant when: $k_{v,catalyst} \leq 0.1\ k_{v,mass\ transfer}$
- externally mass transfer limited when: $k_{v,catalyst} \geq 10\ k_{v,mass\ transfer}$

6.3.2 Calculation results and discussion

Case I: no significant internal diffusion

The maximum effective thickness of the catalyst coating $d_{coating,eff}$ was calculated to be $4.1 \cdot 10^{-6}$ $m_{coating}$, using equation (6.10), the data in Figure 6.8 and the maximum allowed Thiele modulus at which internal mass transfer does not affect the reaction rate, $\varphi = 0.4$. Using equation (6.11) the coating thickness can be calculated as a function of channel diameter and varied between $3.91 \cdot 10^{-6}$ m_c for $D_c = 1 \cdot 10^{-4}$ m_c and $4.07 \cdot 10^{-6}$ $m_{coating}$ for $D_c = 2.5 \cdot 10^{-3}$ m_c. As this value hardly varies with channel diameter for the range covered in these calculations, for further analysis, a value of $4 \cdot 10^{-6}$ $m_{coating}$ is taken to be the maximum thickness of the catalyst layer at which internal mass transfer is not a factor. Equations (6.13), (6.14) and (6.15) are then used to calculate $k_{v,catalyst}$.

The liquid film thickness is calculated according to the equation of Aussillous and Quéré [8], as given in equation (6.5), but replacing D_c by $D_c - 2d_{coating}$, in order to correct for a fraction of the channel diameter occupied by the coating not being available for gas-liquid flow, giving equation (6.17). Equation (6.9) is then used to calculate $k_{v,mass\ transfer}$.

$$\frac{d_f}{D_c - 2d_{coating}} = \frac{0.67 Ca_b^{\frac{2}{3}}}{1 + 3.34 Ca_b^{\frac{2}{3}}} \tag{6.17}$$

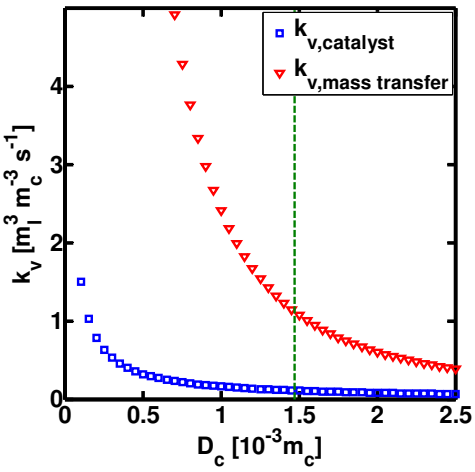

Figure 6.8: $k_{v,catalyst}$ and $k_{v,mass\ transfer}$ as a function of channel diameter D_c for φ= 0.4. The dashed line indicates the maximum channel diameter for which external mass transfer does not affect the overall volumetric reaction rate coefficient: $k_{v,catalyst} \leq 0.1\ k_{v,mass\ transfer}$

The results are given in Figure 6.8. The reaction rate is not significantly influenced by mass transfer for channel diameters smaller than $1.47 \cdot 10^{-3}$ m. At this diameter, the values of $k_{v,mass\ transfer}$ and $k_{v,catalyst}$ are 1.11 $m_l^3 m_c^{-3} s^{-1}$ and 0.11 $m_l^3 m_c^{-3} s^{-1}$, respectively, leading to $k_{v,ov}$ = 0.10 $m_l^3 m_c^{-3} s^{-1}$.

The amount of catalyst per volume unit of capillary is then 16.9 $kg_{coating}/m_c^3$. For channels with a diameter smaller than this value, decreasing the channel diameter results in an approximately linear increase of the volumetric reaction rate coefficient $k_{v,ov}$ solely due to increasing the amount of catalyst per unit volume of channel diameter. However, for equal bubble frequency and velocity, this will cause an approximately quadratic increase of the pressure drop.

Case II: $k_{v,ov}$ as a function of D_c and $d_{coating}$, allowing for internal and external mass transfer effects

For the calculations, the channel diameter D_c is varied between $1 \cdot 10^{-4}$ m_c and $2.5 \cdot 10^{-3}$ m_c and for each diameter, the thickness of the catalyst layer is varied between $1 \cdot 10^{-6}$ m_c and $1 \cdot 10^{-4}$ m_c. The results for $k_{v,catalyst}$ are given in Figure 6.9 and the dashed line indicates the

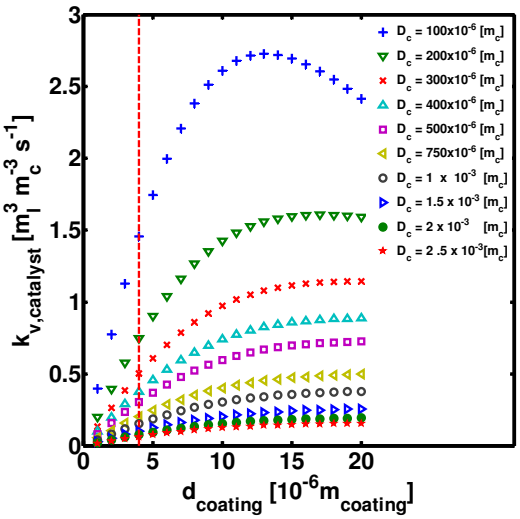

Figure 6.9: $k_{v,catalyst}$ as a function of channel diameter D_c and thickness of the catalyst coating $d_{coating}$. The dashed line indicates the maximum thickness of the catalyst coating for which internal mass transfer does not affect the volumetric reaction rate coefficient of the catalyst ($d_{coating}$ for which φ=0.4).

maximum thickness of the catalyst layer for which internal mass transfer does not significantly affect the overall reaction rate, as calculated in the previous section.

Furthermore, the figure shows that increasing the catalyst layer thickness beyond approximately $10 \cdot 10^{-6}$ $m_{coating}$ hardly causes an increase of $k_{v,catalyst}$ for all channel diameters. For these coating thicknesses, the increase of $k_{v,catalyst}$ by increasing the amount of catalyst per unit volume of capillary is counteracted by a decrease of the effectiveness factor η. For a channel diameter $1 \cdot 10^{-4}$ m_c this results in a decrease of $k_{v,catalyst}$ upon increasing $d_{coating}$ to values above approximately $13 \cdot 10^{-6}$ $m_{coating}$. This is the result of $d_{eff,coating}$ not being a linear function of $d_{coating}$ when the coating occupies a significant part of the capillary volume.

Rather than comparing the values of $k_{v,catalyst}$ directly to those of $k_{v,mass\ transfer}$, it is more insightful to plot the ratio of the two as a function of channel diameter and thickness of the catalyst coating, as is done in Figure 6.10. The vertical dashed line indicates the maximum thickness of the catalyst coating for which internal mass transfer does not affect the volumetric reaction rate coefficient of the catalyst ($d_{coating}$ for which φ=0.4). The horizontal dashed line indicates the criterion $k_{v,catalyst} \cdot k_{v,coating}^{-1}$ = 0.1. At ratios lower than this criterion, external mass transfer does not significantly affect the volumetric reaction rate coefficient $k_{v,ov}$.

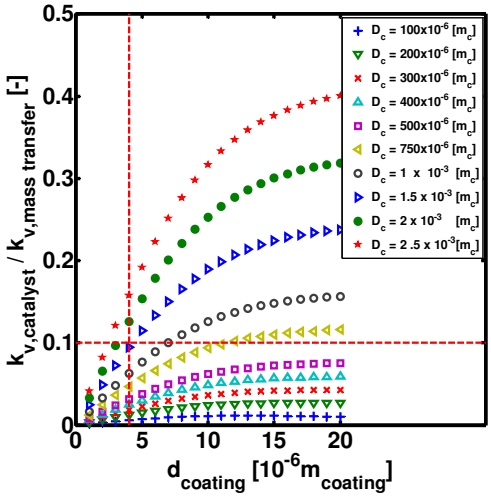

Figure 6.10: The ratio of $k_{v,catalyst}$ and $k_{v,mass\ transfer}$ as a function of channel diameter D_c and thickness of the catalyst coating $d_{coating}$. The vertical dashed line indicates the maximum thickness of the catalyst coating for which internal mass transfer does not affect the volumetric reaction rate coefficient of the catalyst ($d_{coating}$ for which φ=0.4). The horizontal dashed line indicates the criterion $k_{v,catalyst}$ /$k_{v,coating}$ =0.1. At ratios lower than this criterion, external mass transfer does not significantly affect the reaction rate volumetric reaction rate coefficient $k_{v,ov}$.

The figure shows that, for the conditions studied here, for capillaries with a diameter of approximately $6.5 \cdot 10^{-4}$ m_c or less, external mass transfer will not affect $k_{v,ov}$ significantly, regardless of the amount of catalyst deposited on the capillary wall. Furthermore, for capillaries with a diameter of $1.47 \cdot 10^{-3}$ m_c or less, increasing the thickness of the catalyst coating will result in internal mass transfer affecting the reaction rate before external mass transfer becomes significant. This limiting value was already determined as it is the result from the calculations in *Case I*. For capillaries with a larger diameter, the reverse is true and upon increasing the thickness of the catalyst coating, external mass transfer will affect the reaction rate before internal mass transfer.

Figure 6.11 contains the same data as Figure 6.10, but the ratio of $k_{v,catalyst}$ and $k_{v,mass\ transfer}$ is now plotted against the channel diameter and every line represents one value of the thickness of the catalyst layer, varying from $1 \cdot 10^{-6}$ $m_{coating}$ to $20 \cdot 10^{-6}$ $m_{coating}$. When plotted this way, the data show that the dependency of the ratio $k_{v,catalyst}$ and $k_{v,mass\ transfer}$ is almost perfectly linear.

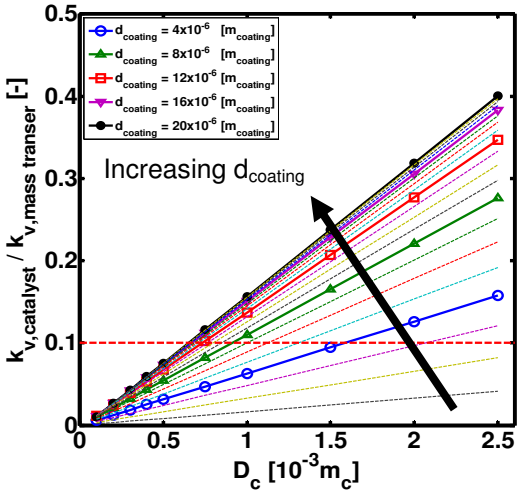

Figure 6.11: The ratio of $k_{v,catalyst}$ and $k_{v,coating}$ as a function of channel diameter D_c and thickness of the catalyst coating $d_{coating}$. Internal mass transfer effects were absent for a coating thickness smaller than $4 \cdot 10^{-6}$ $m_{coating}$ ($d_{coating}$ for which φ=0.4). The horizontal dashed line indicates the criterion $k_{v,catalyst}$ /$k_{v,coating}$ =0.1. At ratios lower than this criterion, external mass transfer does not significantly affect the reaction rate volumetric reaction rate coefficient $k_{v,ov}$. The thickness of the catalyst coating was varied from $1 \cdot 10^{-6}$ to $2 \cdot 10^{-6}$ $m_{coating}$ with increments of $1 \cdot 10^{-6}$ $m_{coating}$.

This can be understood from a simple scaling analysis. The volumetric mass transfer rate constant depends on the gas-liquid interfacial area and the thickness of the liquid film as shown in equation (6.9). When the bubble velocity is not varied with varying channel diameter, the liquid film thickness is a fixed fraction of the open channel volume, as can be seen in equation (6.17). Thus, if the thickness of the catalyst layer is thin compared to the channel diameter, the liquid film thickness scales linearly with the channel diameter. From equation (6.9), it is then clear that $k_{v,mass\ transfer}$ scales with D_c^{-2}, for relatively thin catalyst coatings and liquid film thickness. Equations (6.14) and (6.15) show that, for a given relatively thin catalyst coating, $k_{v,catalyst}$ depends only on the amount of catalyst per unit volume of capillary, which scales with D_c^{-1}. The ratio of $k_{v,catalyst}$ and $k_{v,mass\ transfer}$ thus scales inearly with D_c.

The values of $k_{v,ov}$ obtained for the various values of coating thickness and channel diameter are given in Figure 6.12. The largest value for $k_{v,ov}$ obtained for the conditions and channel diameters studied in this work, is 2.7 $m_l^3 m_c^{-3} s^{-1}$ at a capillary diameter of $1 \cdot 10^{-4}$ m_c and a coating thickness of $1.3 \cdot 10^{-5}$ m_c. At these conditions, internal mass transfer is

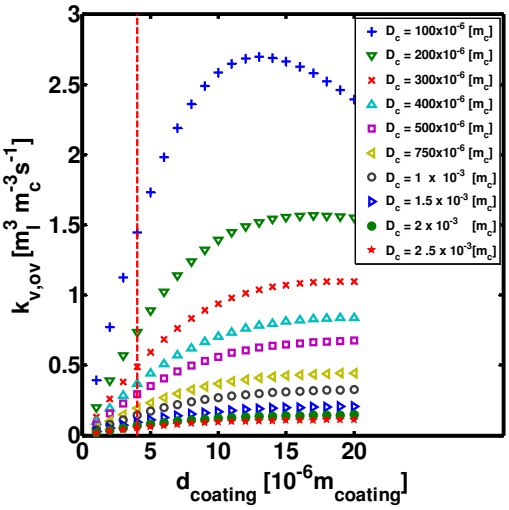

Figure 6.12: $k_{v,ov}$ as a function of channel diameter D_c and thickness of the catalyst coating $d_{coating}$. The dashed line indicates the maximum thickness of the catalyst coating for which internal mass transfer does not affect the volumetric reaction rate coefficient of the catalyst ($d_{coating\varphi}$ for which φ=0.4).

significant while external mass transfer is not. When avoiding both internal and external mass transfer effects, the largest value for $k_{v,ov}$ is 1.45 $m_l^3 m_c^{-3} s^{-1}$ at a capillary diameter of $1 \cdot 10^{-4}$ m_c and a coating thickness of $3.9 \cdot 10^{-6}$ $m_{coating}$, as can also be seen in Figure 6.8, although it will be higher for channels with an even smaller diameter.

6.3.3 Conclusions optimizing the channel diameter and catalyst layer thickness

An optimization study was done in order to determine the maximum catalyst layer thickness for which internal diffusion is not significant and, when applying a catalyst layer of this thickness, at which channel diameter external mass transfer is no longer significant. It was also evaluated what values for the volumetric reaction rate coefficient can be achieved, while accepting internal and external mass transfer limitations. The calculations of the volumetric rate constant of the catalyst are based on data obtained from the hydrogenation of phenylacetylene to styrene at a temperature of 343 K using a 1wt%$_{coating}$ Pd on titania catalyst. At these conditions, the catalyst activity was 10 $m_l^3 m_{coating}^{-3} s^{-1}$. The calculations of the volumetric mass transfer coefficient are based on a Taylor flow with saturated liquid slugs.

The following conclusions are drawn with respect to optimizing the thickness of the catalyst layer and the channel diameter for avoiding internal and external mass transfer limitations.

- External mass transfer limitations are avoided for channel diameters less than approximately $6.5 \cdot 10^{-4}$ m_c, regardless of the thickness of the catalyst layer.

- Internal mass transfer limitations are avoided, if the thickness of the catalyst layer is less than $4 \cdot 10^{-6}$ $m_{coating}$.

- Both internal and external mass transfer limitations are avoided, if the thickness of the catalyst layer is less than $4 \cdot 10^{-6}$ $m_{coating}$ and the channel diameter is smaller than $1.47 \cdot 10^{-3}$ m_c. At these limiting values the overall reaction rate coefficient has a value of 0.10 $m_l^3 m_c^{-3} s^{-1}$.

- The ratio of the volumetric reaction rate coefficient of the catalyst with the volumetric mass transfer coefficient scales linearly with the channel diameter, for a fixed bubble velocity, fixed catalyst coating thickness and a relatively thin liquid film and catalyst coating.

The following results and observations were obtained when allowing for internal and external mass transfer limitations. The maximum volumetric reaction rate coefficients are found for the smallest channel diameters under internal mass transfer limiting conditions, at which external mass transfer limitations no longer occur. For a given diameter in this range, increasing the thickness of the catalyst layer will result in an almost linear increase of the amount of catalyst per unit volume of capillary, but the effect is counteracted by the increase of diffusion limitations. It was found that increasing the thickness of the catalyst layer beyond $1.3 \cdot 10^{-5}$ $m_{coating}$ hardly results in an increase of the volumetric rate constant of the catalyst.

For both cases, with channel diameters small enough to avoid external mass transfer limitations, reducing the channel diameter at a constant catalyst layer thickness, results in an approximately linear increase of the overall volumetric reaction rate, solely due to increasing the amount of catalyst per unit reactor volume. However, for equal bubble frequency and velocity, this will cause an approximately quadratic increase of the pressure drop and it depends on the application whether the increase of the overall reaction rate coefficient is worth the increase in pressure drop.

Nomenclature

A	area of the capillary cross-section [m_c^2]
A_b	area of the bubble cross-section [m_b^2]
a_{bf}	interfactial area of the gas bubble and the liquid film per unit of capillary volume [$m_l^2\ m_c^{-3}$]
a_{sf}	specific interfactial area of the liquid slug and the liquid film per unit of capillary volume [$m_l^2\ m_c^{-3}$]
c	fit parameter [-]
Ca_b	capillary number based on the properties of the liquid and the gas bubble velocity [-]
$\mathcal{D}$	diffusion coefficient of hydrogen in ispropanol [$m_l^2\ s^{-1}$]
D_c	channel diameter [m_c]
$\mathcal{D}_{eff}$	effective diffusion coefficient of hydrogen in ispropanol in the catalyst coating [$m_l^3\ m_{coating}^{-1}\ s^{-1}$]
$d_{coating}$	catalyst coating thickness [$m_{coating}$]
$d_{coating,eff}$	area of the catalyst coating in contact with liquid per unit volume of catalyst coating [$m_{coating}$]
d_f	liquid film thickness [m_l]
E_{app}	Apparent activation energy [kJ mol^{-1}]
F_b	frequency of bubbles [s^{-1}]
F_{H2}	molar flow rate of hydrogen [$mol_{H2}\ s^{-1}$]
Fo	Fourier time [-]
H	Henry coefficient of hydrogen in isopropanol [Pa $m_l^3\ mol_{H2}^{-1}$]

$k_{l,bf}$	liquid side mass transfer coefficient at the interface of the gas bubble and the liquid film [$m_l\ s^{-1}$]
$k_{v,catalyst}$	volumetric reaction rate constant of the catalyst coating [$m_l^3\ m_c^{-3}\ s^{-1}$]
$k_{v,ov}$	overall volumetric reaction rate constant [$m_l^3\ m_c^{-3}\ s^{-1}$]
$k_{v,mass\ transfer}$	overall volumetric mass transfer coefficient [$m_l^3\ m_c^{-3}\ s^{-1}$]
L_b	length of a bubble [m]
L_s	length of a liquid slug [m]
P	pressure [Pa]
$P_{entrance}$	pressure at the entrance of the reactive capillary [Pa]
P_{exit}	pressure at the exit of the reactive capillary [Pa]
Re_b	Reynolds number based on the properties of the liquid and the gas bubble velocity [-]
Re_{gl}	Reynolds number based on the properties of the liquid and the sum of the superficial gas and liquid velocites [-]
u_b	velocity of a gas bubble [m/s]
R	universal gas constant, 8.314 [$m^3\ Pa\ K^{-1}\ mol^{-1}$]
$Sel._{styrene}$	selectivity towards styrene as mol fraction of styrene in the reaction products [-]
T	temperature [K]
U_g	superficial gas velocity [$m_g^3\ m_c^{-2}\ s^{-1}$]
U_l	superficial liquid velocity [$m_l^3\ m_c^{-2}\ s^{-1}$]
We_b	Weber number based on the properties of the liquid phase and the gas bubble velocity [-]

We_{gl}	Weber number based on the liquid properties and the the sum of the superficial gas and liquid velocites [-]
X_{PA}	conversion of phenylacetylene [-]
z	axial position in the capillary [m_c]

Greek symbols

ε	porosity of the coating [$m_l^3\ m_{coating}^{-3}$]
η	effectiveness factor of the catalyst coating [-]
μ_g	viscosity of the gas [Pa·s]
μ_l	viscosity of the liquid [Pa·s]
σ	surface tension [N/m]
τ	tortuosity factor of the catalyst coating [-]
φ	Thiele modulus [-]

Subscripts

b	gas bubble
c	capillary
f	liquid film
s	liquid slug
uc	unit cell
coating	catalyst coating

References

[1] Kreutzer, M. T., Kapteijn, F., Moulijn, J. A., Heiszwolf, J. J., Multiphase monolith reactors: Chemical reaction engineering of segmented flow in microchannels. *Chem. Eng. Sci.*, 60(22), 5895-5916, 2005

[2] Vergunst, T., Kapteijn, F., Moulijn, J. A., Optimization of Geometric Properties of a Monolithic Catalyst for the Selective Hydrogenation of Phenylacetylene. *Industrial & Engineering Chemistry Research*, 40(13), 2801-2809, 2001

[3] Irandoust, S., Andersson, B., Mass transfer and liquid-phase reactions in a segmented two-phase flow monolithic catalyst reactor. *Chem. Eng. Sci.*, 43(8), 1983-1988, 1988

[4] Nijhuis, T. A., Kreutzer, M. T., Romijn, A. C. J., Kapteijn, F., Moulijn, J. A., Monolithic catalysts as more efficient three-phase reactors. *Catal Today*, 66(2-4), 157-165, 2001

[5] Rebrov, E. V., Berenguer-Murcia, A., Skelton, H. E., Johnson, B. F. G., Wheatley, A. E. H., Schouten, J. C., Capillary microreactors wall-coated with mesoporous titania thin film catalyst supports. *Lab Chip Miniaturisation Chem. Biol.*, 9(4), 503-506, 2009

[6] Chaudhari, R. V., Jaganathan, R., Kolhe, D. S., Emig, G., Hofmann, H., Kinetic modelling of a complex consecutive reaction in a slurry reactor: Hydrogenation of phenyl acetylene. *Chem. Eng. Sci.*, 41(12), 3073-3081, 1986

[7] Jackson, S. D., Shaw, L. A., The liquid-phase hydrogenation of phenyl acetylene and styrene on a palladium/carbon catalyst. *Applied Catalysis A: General*, 134(1), 91-99, 1996

[8] Aussillous, P., Quéré, D., Quick deposition of a fluid on the wall of a tube. *Phys. Fluids*, 12(10), 2367-2371, 2000

[9] Lockhart, R. W., Martinelli, R. C., Proposed correlation of data for isothermal two-phase, two-component flow in pipes. *Chem. Eng. Prog.*, 45(1), 39-48, 1949

[10] Chisholm, D., A theoretical basis for the Lockhart-Martinelli correlation for two-phase flow. *Int. J. Heat Mass Transf.*, 10(12), 1767-1778, 1967

[11] Lide, D. R., *Handbook of Chemistry and Physics,* CRC Press, Inc., Boca Raton, 85th ed., 2004

[12] Young, C. L., Battino, R., Clever, L. H., Cargill, R. W., *Hydrogen and Deuterium,* Pergamon Press, New York, Vol. 5/6, 1981

[13] Aspen Plus 2006, Aspen Technology, Inc., Burlington, 2006

[14] Froment, G. F., Bischoff, K. B., *Chemical Reactor Analysis and Design,* John Wiley & Sons, New York, 2nd, 1990

[15] Kreutzer, M. T., Du, P., Heiszwolf, J. J., Kapteijn, F., Moulijn, J. A., Mass transfer characteristics of three-phase monolith reactors. *Chem. Eng. Sci.*, 56(21-22), 6015-6023, 2001

[16] Thulasidas, T. C., Abraham, M. A., Cerro, R. L., Flow patterns in liquid slugs during bubble-train flow inside capillaries. *Chem. Eng. Sci.*, 52(17), 2947-2962, 1997

[17] Chen, I. Y., Yang, K. S., Wang, C. C., An empirical correlation for two-phase frictional performance in small diameter tubes. *Int. J. Heat Mass Transf.*, 45(17), 3667-3671, 2002

[18] Weerachawanasak, P., Praserthdam, P., Arai, M., Panpranot, J., A comparative study of strong metal-support interaction and catalytic behavior of Pd catalysts supported on micron- and nano-sized TiO2 in liquid-phase selective hydrogenation of phenylacetylene. *Journal of Molecular Catalysis A: Chemical*, 279(1), 133-139, 2008

[19] Weerachawanasak, P., Mekasuwandumrong, O., Arai, M., Fujita, S. I., Praserthdam, P., Panpranot, J., Effect of strong metal-support interaction on the catalytic performance of Pd/TiO2 in the liquid-phase semihydrogenation of phenylacetylene. *Journal of Catalysis*, 262(2), 199-205, 2009

[20] Molnár, A., Sárkány, A., Varga, M., Hydrogenation of carbon-carbon multiple bonds: Chemo-, regio- and stereo-selectivity. *Journal of Molecular Catalysis A: Chemical*, 173(1-2), 185-221, 2001

[21] Levenspiel, O., *Chemical Reactor Engineering,* John Wiley & Sons, New York, 3rd ed., 1999

Chapter 7

Conclusions, suggestions for further research and some remarks on gas-liquid-solid reactions in small channels

7.1 Conclusions

The work presented in this thesis was done within the framework of a larger project with the goal of developing a "lab-on-a-chip"-like microreactor system for the selective solid catalyzed hydrogenation of α,β-unsaturated aldehydes to their corresponding alcohols. The goal of this work was to obtain more insight in the hydrodynamics of gas-liquid flows in small channels and their relation to pressure drop and mass transfer to, ultimately, be able to design the microreactor.

This study focuses on gas-liquid Taylor flow, since it is the main flow regime of interest for performing gas-liquid-solid reactions in micro-structured reactors and monoliths. It consists of an alternating sequence of gas bubbles and liquid slugs moving through a small channel (diameter typically < 1 mm). The length of the gas bubbles is larger than the channel diameter and a thin liquid film separates the gas bubbles from the channel walls. This thin liquid film ensures a short diffusion length for the gas component to the channel walls, where the catalyst is often located. The large concentration gradient in this film, in combination with the large surface to volume ratio of small channels, results in enhanced mass transfer rates compared to conventional gas-liquid-solid reactors, such as bubble columns or stirred slurry reactors.

The behaviour of the liquid film thickness as a function of the properties of the liquid phase and the gas bubble velocity is well understood for channels with a circular cross-

sectional area and for negligible inertial and gravitational forces. However, in practice, inertial forces are not always negligible and, in monolithic reactors and microfluidic devices, the cross-sectional area of the channels is often rectangular or square. In this work, the fraction of channel cross-sectional area occupied by the liquid film and the gas-hold up were determined from combining data from image analysis and a mass balance based Taylor flow model. Experimental data were obtained for a nitrogen-water Taylor flow in channels with a cross-sectional area of 100x50 μm^2 and for bubble velocities ranging from 0.24 to 7.12 m/s. The gas hold-up as a function of the ratio of the superficial gas velocity and the sum of the superficial gas and liquid velocities was shown to follow the Armand correlation. The model shows that the validity of the Armand correlation implies that the fraction of cross-sectional channel area occupied by the liquid film does not depend on the gas bubble velocity. In literature, the Armand correlation is also obtained for nitrogen-water and air-water Taylor flows for a wide range of bubble velocities and channel diameters. This indicates that, when inertial effects are significant, the liquid film thickness is independent of the bubble velocity, and occupies a fixed fraction of the channel cross-section independent of the channel diameter.

A new pressure drop model was developed for gas-liquid Taylor flow with a non-negligible film thickness in small channels with a circular cross-section. The model takes two sources of pressure drop into account: (i) frictional pressure drop caused by laminar flow in the liquid slugs, and (ii) an additional pressure drop over a single gas bubble due to the bubble disturbing the otherwise parabolic velocity profile in the liquid slugs. The model shows that (i) the additional pressure drop caused by the presence of the gas bubbles depends on the bubble frequency and the bubble velocity, and (ii) its contribution to the overall pressure drop relative to that of the frictional pressure drop in the liquid phase decreases with increasing gas bubble velocity and decreasing bubble frequency. Experimental data were obtained for nitrogen-water Taylor flow in a round glass channel with an inner diameter of 250 µm. The capillary number Ca_{gl} varied between $2.3 \cdot 10^{-3}$ and $8.8 \cdot 10^{-3}$ and the Reynolds number Re_{gl} varied between 41 and 159. The presented model describes the experimental results with an accuracy of ± 4% of the measured values.

A method was developed for determining the pressure drop of gas-liquid Taylor flow in microchannels by combining data obtained from analysis of images of the Taylor flow with a mass balance based Taylor flow model. The method was applied to water/nitrogen Taylor flow in channels with square and rectangular cross-sectional areas of 50x50 μm^2 and

100x50 μm^2, respectively, and to isopropanol/nitrogen Taylor flow in a channel with a cross-sectional area of 100x50 μm^2. The observed pressure profile for each combination of gas and liquid velocities, liquid phase, and cross-sectional area of the channel, was linear over a distance of 1.8 mm. Since pressure drop models for channels with a non-circular cross-sectional area are lacking, the data were compared to predictions from models developed for channels with a circular cross-sectional area. The models described the data obtained in the channels with a rectangular cross-sectional area within ± 50% of the measured values. The model predictions were less accurate for the channel with a square cross-sectional area, for which an explanation still has to be found. However, it was concluded that the method yields realistic values for the pressure drop of gas-liquid Taylor flows. This method can be used for determining the pressure drop in micro-fluidic chips with channels of an arbitrary cross-section, where directly measuring the pressure or pressure drop is not always feasible, while imaging facilities often are available.

The influence of mixer design, liquid phase and channel dimensions on flow regime transitions in microchannels was studied. The results show that the design of the mixer geometry is mainly of influence for high superficial gas and/or liquid velocities, where inertial forces are significant. Whether water or isopropanol was used, affected most regime transitions, except when both the superficial liquid and gas velocities were high and inertial forces were large compared to surface tension forces. When decreasing the dimensions of the cross-sectional area of the cross-mixer and the downstream channel from 100x50 μm^2 to 50x50 μm^2, annular flow was no longer observed and, at equal liquid velocities, Taylor flow was observed at higher gas velocities.

The length of a Taylor gas bubble as a function of the width of the channels in a cross-mixer was studied experimentally. The results showed that the ratio of the gas bubble length and the width of the channel depends linearly on the ratio of the gas and liquid flow rates in the mixer. This result implies that, for a given mixer, the gas bubble and liquid slug lengths can not be varied independently from each other. However, if the geometry of the mixer can be varied separately from the dimensions of the downstream channel, then the gas bubble length, liquid slug length and total flow rate, can each be controlled.

The hydrogenation of phenylacetylene in isopropanol was performed over Pd supported on mesoporous titania films with a thickness of $120 \cdot 10^{-9}$ $m_{coating}$ coated on the walls of a glass capillary with an inner diameter of 250 μm_c. Two such capillaries were used,

containing 1 $wt\%_{coating}$ and 2 $wt\%_{coating}$, respectively. The reaction was performed in the Taylor flow and Taylor-ring-annular regimes at temperatures varying from 313 to 343 K. The phenylacetylene conversions were smaller than 0.2 and styrene selectivities were higher than 0.92. Based on these data, an optimization study was done where the thickness of the catalyst layer and the diameter of the channel were varied. The following conclusions were drawn with respect to optimizing the thickness of the catalyst layer and the channel diameter in order to avoid internal and external mass transfer limitations.

- External mass transfer limitations can be avoided for channel diameters less than approximately 650 μm_c, regardless of the thickness of the catalyst layer.

- Internal mass transfer limitations can be avoided, if the thickness of the catalyst layer is less than 4 $\mu m_{coating}$.

- Both internal and external mass transfer limitations are avoided, if the thickness of the catalyst layer is less than 4 $\mu m_{coating}$ and the channel diameter is smaller than $1.47 \cdot 10^{-3}$ m_c. At these limiting values, the overal volumetricl reaction rate coefficient has a value of 0.10 $m_l^3 m_c^{-3} s^{-1}$. The amount of catalyst per unit of capillary volume is then 16.9 $kg_{coating}/m_c^3$.

- For a fixed bubble velocity, fixed catalyst coating thickness and a relatively thin liquid film and catalyst coating, the ratio of the volumetric reaction rate coefficient of the catalyst and the volumetric mass transfer coefficient scales linearly with the channel diameter.

Furthermore, for channel diameters small enough to avoid external mass transfer limitations, reducing the channel diameter at a constant catalyst layer thickness results in a nearly linear increase of the overall volumetric reaction rate, solely due to increasing the amount of catalyst per unit reactor volume. For the conditions and channel diameters studied in this work, the largest value for the overall volumetric reaction rate coefficient was 2.7 $m_l^3 m_c^{-3} s^{-1}$. This value was obtained for a channel diameter of 100 μm_c and a coating thickness of 13 μm_c. At these conditions, external mass transfer limitations are not present and internal mass transfer limits the overall reaction rate. When avoiding both internal and external mass transfer effects, the largest value for the overall volumetric reaction rate coefficient is 1.45 $m_l^3 m_c^{-3} s^{-1}$, at a capillary diameter of 100 μm_c and at a coating thickness of 3.9 $\mu m_{coating}$.

7.2 Suggestions for further research

The understanding of gas-liquid Taylor flow hydrodynamics and its relation to mass transfer and pressure drop is growing, particularly for channels with a circular cross-sectional area and negligible inertial and gravitational forces. For these conditions, the behaviour of the liquid film thickness has been well described.

Numerical studies have been performed, which include the effect of inertial forces on the thickness of the liquid film, but no correlation or model is available. The influence of inertial forces on pressure drop is also not yet completely understood. Since in practical situations, such as in monolith reactors, inertial forces can be significant, results from further study would surely be relevant.

Furthermore, channels with a non-circular cross-sectional area are encountered in monolith reactors and almost all microfluidic devices. The behaviour of the liquid film is far less understood, as its thickness is no longer constant along the perimeter of the channel. This non-uniformity of the liquid film complicates experiments and numerical calculations. Some studies have been performed with respect to the liquid film thickness in the corners of a square channel, but hardly any data are available for the liquid film thickness along the remaining sections of the channel walls. Lack of knowledge concerning the behaviour of the liquid film in non-circular channels implies that mass transfer and pressure drop are less well understood for these channel geometries. In fact, mass transfer and pressure drop models, specifically developed for non-circular channels, are not available. Considering the practical relevance of Taylor flow in non-circular channels, it is a field worthy of further study.

Heat transfer in gas-liquid Taylor flow was beyond the scope of this thesis, but a general remark can be made. Considering the fact that heat transfer can be of crucial importance in the design of reactors, it is somewhat strange that it has hardly been studied for gas-liquid Taylor flow. An increased knowledge of heat transfer in gas-liquid Taylor flows would surely be of use for designing reactors operating in this regime.

7.3 Some remarks on gas-liquid-solid reactions in small channels

Performing gas-liquid-solid reactions in reactors with small characteristic length scales, such as a monoliths and microreactors, results in increased volumetric mass transfer rates. This is of particular interest with respect to gas component mass transfer, since it often limits the reaction rate in conventional reactors.

If the channels are small enough, external mass transfer limitations can be avoided and the catalyst is used most efficiently. The reaction rate per unit of reactor volume then depends on how much catalyst can be applied per unit of reactor volume. For monoliths and microreactors, the catalyst is applied as a washcoat on the channel walls. For a monolith reactor, the amount of catalyst per unit of reactor volume is generally lower than in a packed bed reactor. Thus, even though the catalyst is used more efficiently, the lower amount of catalyst per unit of reactor volume results in a less spectacular increase of the volumetric reaction rate, than the increase in mass transfer rates would suggest.

The reaction rate per unit of reactor volume can be increased by increasing the amount of catalyst per unit of reactor volume. This can be achieved by increasing the thickness of the catalyst layer, by decreasing the size of the channels, or by doing both. However, there are limits with respect to the effectiveness of increasing the thickness of the catalyst layer, since internal mass transfer limitation will become significant. It depends on the type of reaction whether this can be allowed or not. The remaining question is then whether it is worthwhile to perform these types of reactions in microreactors, where the channels can be an order of magnitude smaller than those typically used in monolith reactors.

At channel diameters small enough to overcome external mass transfer limitations, reducing the diameter of the channel, at constant thickness of the catalyst layer, results in a nearly linear increase of the reaction rate per unit of reactor volume. However, the pressure drop, and thus the energy dissipation per unit of reactor volume, increases quadratically. The net result is that the amount of energy dissipated by friction increases per unit mass of product. It depends on the application whether this reduction of the efficiency of the reactor is worth the increase of the reaction rate per unit of reactor volume.

The main advantage of performing gas-liquid-solid reactions in small channels is the ability to overcome heat and external mass transfer limitations, while maintaining a low pressure drop. Monolith reactors applied for gas-liquid-solid reactions have channel dimensions in the order of a few hundred micrometers to a millimeter. Several studies, including this thesis, show that external mass transfer limitations are already significantly reduced, or even completely avoided, at these channel dimensions. Unless heat transfer limitations are present at this length scale, a further reduction of the channel diameter results in a less efficient reactor. However, if the intrinsic reaction rate can be increased, heat and external mass transfer limitations may become relevant at dimensions currently applied in monoliths and a further reduction of the channel diameter will then be benificial. These increased intrinsic reaction rates may result from developments in catalysis or from the ability to perform these reactions in a different process window, which may be enabled by using microchannels. Thus, the potential of using smaller channels can be found in the combination with advances in other fields.

List of publications

Journal publications

M.J.F. Warnier, M.H.J.M. de Croon, E.V. Rebrov, J.C. Schouten, Pressure drop of gas-liquid Taylor flow in micro capillaries, *Microfluidics Nanofluidics*, in press, (2009), DOI: 10.1007/s10404-009-0448-z

M.J.F. Warnier, E.V. Rebrov, M.H.J.M. de Croon, V. Hessel, J.C. Schouten, Gas hold-up and liquid film thickness in Taylor flow in rectangular micro channels, *Chem. Eng. J.*, 135(1), S153-S158, (2008)

V. Haverkamp, V. Hessel, H. Löwe, G. Menges, M.J.F. Warnier, E.V. Rebrov, M.H.J.M. de Croon, J.C. Schouten, M. Liauw, Hydrodynamics and mixer-induced bubble formation in microbubble columns with single and multiple channels, *Chem. Eng. Technol.*, 29(9), 1015-1026, (2006)

V.P. Chilekar, M.J.F. Warnier, J. van der Schaaf, J.R. van Ommen, B.F.M. Kuster, J.C. Schouten, Bubble size estimation in slurry bubble columns from pressure fluctuations, *AIChE J.*, 51(7), 1924-1937, (2005)

K.C. Ruthiya, V.P. Chilekar, M.J.F. Warnier, J. van der Schaaf, J.R. van Ommen, B.F.M. Kuster, J.C. Schouten, Detecting regime transitions in slurry bubble columns using pressure time series, *AIChE J.,* 51(7), 1951-1965, (2005)

Refereed conference proceedings

M.J.F. Warnier, E.V. Rebrov, M.H.J.M. de Croon, V. Hessel, J.C. Schouten, Horizontal Taylor flow hydrodynamics, pressure drop and overall mass transfer in a capillary reactor, in *Proc. 10th Int. Conf. on Microreaction Technology (IMRET-10)*; Editors: -, New Orleans, LA, United States, CD-ROM 235a, (2008)

M.J.F. Warnier, M.H.J.M. de Croon, E.V. Rebrov, V. Hessel, J.C. Schouten, Pressure drop by high speed imaging techniques in water/nitrogen and isopropanol/nitrogen Taylor flows in

rectangular micro channels, in *7th Netherlands Process Technology Symposium (NPS7)*; Editors: -, Veldhoven, Netherlands, pp. 1, (2007)

C. Dezelah, L. Niinistö, E.V. Rebrov, M.J.F. Warnier, M.H.J.M. de Croon, J.C. Schouten, Synthesis and characterization of ALD-Pd catalyst for application in multiphase microstructured reactors, in *Proc. EuropaCat VIII*; Editors: -, Turku, Finland, p2-81, (2007)

E.V. Rebrov, M.J.F. Warnier, O. Muraza, M.H.J.M. de Croon, V. Hessel, J.C. Schouten, Advanced catalytic microstructured reactor for continuous chemical synthesis integrated with a separation step, in *AIChE Spring Meeting*; Editors: -, Houston, TX, United States, CD-ROM nr. 95b, (2007)

V. Hessel, H. Löwe, P. Löb, G. Menges, M.J.F. Warnier, E.V. Rebrov, M.H.J.M. de Croon, J.C. Schouten, G-L and G-L-S micro process engineering: Transfer of laboratory development to production-oriented scaling-out, in *Proc. 6th Int. Symp. on Catalysis in Multiphase Reactors (CAMURE-6)*; Editors: -, Pune, India, 1 p, (2007)

M.J.F. Warnier, E.V. Rebrov, M.H.J.M. de Croon, V. Hessel, J.C. Schouten, The influence of mixer geometry on the hydrodynamics of gas/liquid flows in rectangular micro channels, in *Book of Abstracts 9th Int. Conf. on Microreaction Technology (IMRET-9);* Editors: -, Potsdam, Germany, pp. 108-109, (2006)

V. Hessel, G. Menges, V. Haverkamp, M. Liauw, J.C. Schouten, M.J.F. Warnier, Micro bubble column - fluid dynamics, modelling, and applications, in *Proc. 7th German/Japanese Symposium on Bubble Columns (Bubble Columns 2006), May 20-23*; Editors: -, Goslar, Germany, (2006)

J. van der Schaaf, V.P. Chilekar, M.J.F. Warnier, B.F.M. Kuster, J.C. Schouten, Determination of gas bubble size from spectral analysis of pressure time series, in *Proc. 6th Int. Conference on Gas-Liquid and Gas-Liquid-Solid Reactor Engineering*, Summaries of yet unpublished papers/posters; Editors: -, Vancouver, BC, Canada, paper 73a, (2003)

Dankwoord

Zo, eindelijk is mijn proefschrift zo goed als af. Nog “even” het dankwoord schrijven en dan kan het naar de drukker. Ik mag dan de enige auteur zijn die op de omslag van dit proefschrift staat vermeld, maar dit boekje was er nooit gekomen zonder de betrokkenheid van een groot aantal mensen. Het zou te ver gaan om iedereen hier persoonlijk te bedanken, maar een paar mensen hebben een dusdanig grote bijdrage geleverd, dat ik hen er toch uit wil lichten.

Allereerst wil ik Jaap Schouten bedanken voor de mogelijkheid mijn promotieonderzoek te doen binnen de capaciteitsgroep Chemical Reactor Engineering. Jaap, jouw hulp en tips zijn zeer waardevol geweest bij het schrijven van abstracts, het voorbereiden van lezingen, en het schrijven van publicaties. Ook wat betreft het maken van keuzes binnen een promotieonderzoek heb ik in de afgelopen jaren veel van je mogen leren. Maar ik ben je ongetwijfeld het meeste dank verschuldigd voor de manier waarop je me geholpen hebt het werk af te ronden.

Vervolgens is het de beurt aan mijn dagelijkse begeleiders: Mart de Croon en Evgeny Rebrov. Mart, het is al door de nodige ex-promovendi opgemerkt, maar jij bent een wandelende encyclopedie van vakkennis, waar ik dankbaar gebruik van heb mogen maken. We hebben de nodige uren al kriebelend op een whiteboard doorgebracht en daarbij heb ik veel van je mogen opsteken over, bij gebrek aan een betere omschrijving, de kunst van het afschatten. Verder zal ik mij altijd de vrolijk gebrachte, al dan niet cynische, analyses van een ontelbaar aantal onderwerpen met veel plezier blijven herinneren. Dat gaf een, door mij zeer gewaardeerde, extra dimensie aan onze samenwerking.

Evgeny, zoals het een echte onderzoeker betaamt, is jouw immer scherpe blik van grote waarde geweest voor mijn promotieonderzoek en, in het bijzonder, tijdens het schrijven van de verschillende abstracts en publicaties.

Behalve mijn begeleiders en stafleden heb ik natuurlijk ook een groot aantal promovendi als collega’s gehad. Zij hebben allen bijgedragen aan de ervaringen die ik heb opgedaan tijdens mijn promotieonderzoek in Eindhoven, maar ik zou, zonder iemand te kort te willen doen,

toch graag een aantal van mijn (ex-)collega promovendi expliciet willen noemen. Niek, Stijn en Patrick, ik zou alinea's kunnen volschrijven met anekdotes over onze zinnige en onzinnige discussies, congresbezoeken en "avondvullende programma's", maar ik ga het kort houden. Jullie zijn de "vaste kern" geweest waardoor ik nooit met tegenzin vanuit Valkenburg richting Eindhoven ben vertrokken, zelfs wanneer het werk even helemaal tegen zat en mijn motivatie een dip had. En dat was, en is nog steeds, heel wat waard.

Iedere promovendus, die tijdens zijn promotieonderzoek experimenteel werk heeft verricht, weet dat adequate technische ondersteuning onmisbaar is. Ik ben dan ook dank verschuldigd aan de hele technische staf, maar met name aan Anton, Madan en Frank voor het meedenken en operationeel maken van mijn eerste opstelling.

En als die opstelling dan eenmaal ter wereld is gekomen, dan moet er ook mee gewerkt worden! Een groot deel van het experimentele werk is door een illuster viertal afstudeerders gedaan: Pascal, Petra, Joyce en Dennis. Jullie inzet waardeer ik nog steeds en ik heb onze samenwerking altijd plezierig gevonden.

Denise, zoals Jaap, samen met de stafleden, de promovendi inhoudelijk op de rails probeert te houden, zo zorg jij er o.a. voor dat wij op de nodige andere vlakken niet ontsporen. En dat is een taak die niet onderschat mag worden…. Naast alle hulp die jij me gedurende de afgelopen jaren bij allerlei zaken hebt gegeven, wil ik je in het bijzonder bedanken voor je hulp bij het doorlopen van de hele procedure rondom de promotie.

Verder wil ik de leden van de gebruikerscommissie van het MiRAACS project bedanken voor de levendige en positieve discussies die wij hebben gehad. Jullie feedback over zowel de voortgang van het project als over de inhoud heb ik zeer gewaardeerd.

Ondanks de inspanningen van alle personen die direct bij mijn promotieonderzoek betrokken waren, had dit proefschrift nooit tot stand kunnen komen als ik niet de onvoorwaardelijke steun van een aantal mensen in mijn privé omgeving had gehad. Het schrijven van dit proefschrift, naast een fulltime baan, was geen gemakkelijke opgave. Mijn dankbaarheid voor het begrip en de bemoedigende woorden van mijn ouders, oma, "schoonouders", familie, vrienden en Petra, aan wie ik in deze periode allen minder aandacht heb kunnen geven dan ik had gewild, is groter dan ik hier kan omschrijven.

Pa en ma, jullie hebben me altijd de mogelijkheid gegeven om te doen wat ik wilde en me mijn eigen pad laten kiezen, met dit als uiteindelijke resultaat. Ik kan jullie hiervoor, en voor de gezellige avonden, tenniswedstrijden, etentjes en concertbezoeken, niet genoeg bedanken.

Pé, laat ik beginnen met je te bedanken voor het volledig doorlezen van dit proefschrift en het van commentaar te voorzien. Degene die ons een beetje kent, weet dat wij een eindige interesse hebben in de inhoud van elkaars werk, dus alle lof voor de vele uren leeswerk. Wat de meeste mensen niet zullen weten, is dat de omslag van dit proefschrift door jou is ontworpen. En dat is het vermelden meer dan waard, want ik ben er trots op. Maar de meeste dank ben ik je voor een andere reden verschuldigd. Ik ben het laatste jaar vooral met dit proefschrift en mijn nieuwe baan bezig geweest en dat was niet altijd even gemakkelijk voor ons. Je begrip hiervoor en de steun die je me, op vele manieren, hebt gegeven, hebben ervoor gezorgd dat ik dit werk heb kunnen afmaken. Naast het ontwerpen van de cover en je “leescommissie-achtige” activiteiten, is dit je grootste bijdrage aan dit proefschrift en daar zal ik je altijd dankbaar voor zijn.

Maurice Warnier

18 oktober 2009

About the author

Maurice Warnier was born on April 22nd 1979 in Maastricht. He graduated from the Trichter College in Maastricht in 1997. In the same year, he started his study in chemical engineering at the Eindhoven University of Technology, from which he obtained his M.Sc. degree in 2003 on the topic of "Determination of the average bubble size in slurry bubble columns by spectral analysis of pressure fluctuations". In March 2004, he started his Ph.D. research at the Laboratory of Chemical Reactor Engineering at the Eindhoven University of Technology under supervision of dr. M.H.J.M. de Croon, dr. E.V. Rebrov, and prof.dr.ir. J.C. Schouten. Since September 1st 2008, he has been working as a process development engineer in the group Performance Materials, Chemistry and Technology at DSM Research, Geleen.